

The Pennsylvania State University
The Graduate School
College of Engineering

**A PRELIMINARY ACOUSTIC INVESTIGATION OF A COAXIAL
HELICOPTER IN HIGH-SPEED FLIGHT**

A Thesis in
Aerospace Engineering
by
Gregory Walsh

© 2016 Gregory Walsh

Submitted in Partial Fulfillment
of the Requirements
for the Degree of

Master of Science

August 2016

The thesis of Gregory Walsh was reviewed and approved* by the following:

Kenneth S. Brentner
Professor of Aerospace Engineering
Thesis Advisor

Jacob W. Langelaan
Associate Professor of Aerospace Engineering

George A. Lesientre
Professor of Aerospace Engineering
Head of the Department of Aerospace Engineering

*Signatures are on file in the Graduate School.

Abstract

The desire for a vertical takeoff and landing (VTOL) aircraft capable of high forward flight speeds is very strong. Compound lift-offset coaxial helicopter designs have been proposed and have demonstrated the ability to fulfill this desire. However, with high forward speeds, noise is an important concern that has yet to be thoroughly addressed with this rotorcraft configuration. This work utilizes a coupling between the Rotorcraft Comprehensive Analysis System (RCAS) and PSU-WOPWOP, to computationally explore the acoustics of a lift-offset coaxial rotor system. Specifically, unique characteristics of lift-offset coaxial rotor system noise are identified, and design features and trim settings specific to a compound lift-offset coaxial helicopter are considered for noise reduction. At some observer locations, there is constructive interference of the coaxial acoustic pressure pulses, such that the two signals add completely. The locations of these constructive interferences can be altered by modifying the upper-lower rotor blade phasing, providing an overall acoustic benefit. Significant noise reduction (and power reduction) is possible by reducing rotor tip speeds – an option available because the coaxial rotor in a compound configuration does not need to provide all the propulsive force. Alternative blade designs and blade configurations also enable noise reduction at an in-plane, forward, target observer. This research is a preliminary investigation into compound lift-offset coaxial helicopter noise with the intention of future research spawning from it.

Table of Contents

List of Figures	vi
List of Symbols	ix
Acknowledgments	xi
Chapter 1	
Introduction	1
1.1 Alternative Rotorcraft Configurations	2
1.1.1 Compound Helicopter	2
1.1.2 Tiltrotor	3
1.1.3 Lift-offset Coaxial Helicopter	4
1.2 Future of Vertical Lift (FVL)	6
1.3 Research Motivation	6
1.3.1 Previous and Ongoing Work	7
1.4 Scope and Organization of Thesis	8
Chapter 2	
Rotorcraft Acoustics Background	10
2.1 Discrete Frequency Noise	10
2.2 Review of Acoustics Theory	12
2.3 Coaxial Acoustic Consideration	13
Chapter 3	
Noise Prediction Methodology	15
3.1 Rotorcraft Comprehensive Analysis System (RCAS)	15
3.1.1 Generalized Dynamic Inflow	16
3.1.2 Prescribed Wake	16
3.2 PSU-WOPWOP	17
3.3 Discussion of Noise Prediction Approach	18
3.3.1 Approach Weaknesses	18
3.3.2 Approach Strengths	19

Chapter 4	
Coaxial Helicopter Acoustic Predictions	20
4.1 Explanation of Figures	20
4.2 XH-59 Helicopter	21
4.3 Coaxial Noise Characteristics	21
4.3.1 Symmetry and Constructive/Destructive Interference	22
4.3.2 Loading Noise: Blade Crossovers & BVI	26
4.3.3 Thickness Noise: Coaxial vs. Conventional	30
4.4 Blade Crossover Comparison	32
4.4.1 Total Noise	33
4.4.2 Thickness Noise	36
4.4.3 Loading Noise	40
4.5 RPM Reduction Study	46
4.5.1 Total Noise	46
4.5.2 Thickness Noise	50
4.5.3 Loading Noise	55
4.5.4 Peak OASPL vs. RPM & M_{AT}	60
4.6 Alternative Blade Design	61
4.6.1 Precursor Exploration	61
4.6.2 Configurations	62
4.6.2.1 Dual-Swept Tip Blades	62
4.6.2.2 Curved-Swept Blades	63
4.6.3 Thickness Noise	65
Chapter 5	
Conclusion and Future Work	68
5.1 Conclusions	68
5.2 Future Work	69
References	70
Appendix A	
BladeMaker: PSU-WOPWOP Geometry	73
A.1 Blade Generation Procedure	73
Appendix B	
Integration of RCAS and PSU-WOPWOP	76
B.1 RCAS Output to ‘.txt’ files via MATLAB	76
B.2 Output ‘.txt’ files to Binary files	78
Appendix C	
PSU-WOPWOP Changes of Base and Namelist	83
C.1 Example Namelist	83

List of Figures

1.1	Bell 533 HPH, Bell Helicopter [3].	3
1.2	Bell XV-3, Bell XV-15, Bell-Boeing V-22 (from left to right) [4].	4
1.3	Sikorsky XH-59, Sikorsky X-2 (from left to right) [8].	6
1.4	Bell Helicopter V-280 Valor and Boeing/Sikorsky SB>1 Defiant.	7
2.1	Typical directivity of various rotorcraft noise sources [22].	11
4.1	XH-59 Helicopter Schematic and Specifications [26].	21
4.2	Coaxial thickness acoustic pressure at in-plane observer locations [30]	22
4.3	Coaxial thickness acoustic spectra at in-plane observer locations [30]	23
4.4	Coaxial thickness acoustic pressure at out-of-plane $\psi=0$ and 180 deg. observer locations	24
4.5	Coaxial thickness acoustic spectra at out-of-plane $\psi=0$ and 180 deg. observer locations	24
4.6	Coaxial thickness acoustic pressure at out-of-plane $\psi=90$ and 270 deg. observer locations	25
4.7	Coaxial thickness acoustic spectra at out-of-plane $\psi=90$ and 270 deg. observer locations	25
4.8	Upper, CCW (left) and lower, CW (right) rotor lift distributions for 160 kts. forward flight speed at 335 RPM [30].	26
4.9	Coaxial loading acoustic pressure at in-plane observer locations.	27
4.10	Coaxial loading acoustic spectra at in-plane observer locations.	27
4.11	Coaxial loading acoustic pressure at out-of-plane $\psi=0$ and 180 deg. observer locations [30]	28
4.12	Coaxial loading acoustic spectra at out-of-plane $\psi=0$ and 180 deg. observer locations [30]	28
4.13	Coaxial loading acoustic pressure at out-of-plane $\psi=90$ and 270 deg. observer locations	29
4.14	Coaxial loading acoustic spectra at out-of-plane $\psi=90$ and 270 deg. observer locations	29
4.15	Coaxial vs. single rotor thickness acoustic pressure at in-plane observer locations [30]	31
4.16	Coaxial vs. single rotor thickness acoustic spectra at in-plane observer locations [30]	31
4.17	Schematic of blade crossover configurations.	32
4.18	Blade crossover comparison of total acoustic pressure at in-plane observer locations [30].	33

4.19	Blade crossover comparison of total acoustic spectra at in-plane observer locations [30].	34
4.20	Blade crossover comparison of total acoustic pressure at out-of-plane $\psi=0$ and 180 deg. observer locations [30]	34
4.21	Blade crossover comparison of total acoustic spectra at out-of-plane $\psi=0$ and 180 deg. observer locations [30]	35
4.22	Blade crossover comparison of total acoustic pressure at out-of-plane $\psi=90$ and 270 deg. observer locations [30]	35
4.23	Blade crossover comparison of total acoustic spectra at out-of-plane $\psi=90$ and 270 deg. observer locations [30]	36
4.24	Blade crossover comparison of thickness acoustic pressure at in-plane observer locations [30].	37
4.25	Blade crossover comparison of thickness acoustic spectra at in-plane observer locations [30].	38
4.26	Blade crossover comparison of thickness acoustic pressure at out-of-plane $\psi=0$ and 180 deg. observer locations [30]	38
4.27	Blade crossover comparison of thickness acoustic spectra at out-of-plane $\psi=0$ and 180 deg. observer locations [30]	39
4.28	Blade crossover comparison of thickness acoustic pressure at out-of-plane $\psi=90$ and 270 deg. observer locations [30]	39
4.29	Blade crossover comparison of thickness acoustic spectra at out-of-plane $\psi=90$ and 270 deg. observer locations [30]	40
4.30	Blade crossover comparison of loading acoustic pressure at in-plane observer locations [30].	41
4.31	Blade crossover comparison of loading acoustic spectra at in-plane observer locations [30].	41
4.32	Blade crossover comparison of loading acoustic pressure at out-of-plane $\psi=0$ and 180 deg. observer locations [30]	42
4.33	Blade crossover comparison of loading acoustic spectra at out-of-plane $\psi=0$ and 180 deg. observer locations [30]	42
4.34	Blade crossover comparison of loading acoustic pressure at out-of-plane $\psi=90$ and 270 deg. observer locations [30]	43
4.35	Blade crossover comparison of loading acoustic spectra at out-of-plane $\psi=90$ and 270 deg. observer locations [30]	43
4.36	Blade crossover comparison of the upper, CCW rotor lift distributions [30]. . . .	45
4.37	Blade crossover comparison of the lower, CW rotor lift distributions [30]. . . .	45
4.38	RPM comparison of total acoustic pressure at in-plane observer locations [30]. . .	47
4.39	RPM comparison of total acoustic spectra at in-plane observer locations [30]. . .	47
4.40	RPM comparison of total acoustic pressure at out-of-plane $\psi=0$ and 180 deg. observer locations [30].	48
4.41	RPM comparison of total acoustic spectra at out-of-plane $\psi=0$ and 180 deg. observer locations [30].	48
4.42	RPM comparison of total acoustic pressure at out-of-plane $\psi=90$ and 270 deg. observer locations [30].	49
4.43	RPM comparison of total acoustic spectra at out-of-plane $\psi=90$ and 270 deg. observer locations [30].	49
4.44	RPM comparison of thickness acoustic pressure at in-plane observer locations [30].	51
4.45	RPM comparison of thickness acoustic spectra at in-plane observer locations [30].	51

4.46	RPM comparison of thickness acoustic pressure at out-of-plane $\psi=0$ and 180 deg. observer locations.	52
4.47	RPM comparison of thickness acoustic spectra at out-of-plane $\psi=0$ and 180 deg. observer locations.	52
4.48	RPM comparison of thickness acoustic pressure at out-of-plane $\psi=90$ and 270 deg. observer locations.	53
4.49	RPM comparison of thickness acoustic spectra at out-of-plane $\psi=90$ and 270 deg. observer locations.	53
4.50	RPM comparison of thickness acoustic pressure at in-plane observer locations [30].	54
4.51	RPM comparison of thickness acoustic spectra at in-plane observer locations [30].	54
4.52	RPM comparison of loading acoustic pressure at in-plane observer locations [30].	55
4.53	RPM comparison of loading acoustic spectra at in-plane observer locations [30]. .	56
4.54	RPM comparison of loading acoustic pressure at out-of-plane $\psi=0$ and 180 deg. observer locations [30].	56
4.55	RPM comparison of loading acoustic spectra at out-of-plane $\psi=0$ and 180 deg. observer locations [30].	57
4.56	RPM comparison of loading acoustic pressure at out-of-plane $\psi=90$ and 270 deg. observer locations [30].	57
4.57	RPM comparison of loading acoustic spectra at out-of-plane $\psi=90$ and 270 deg. observer locations [30].	58
4.58	276 RPM rotor lift distribution for both the CCW, upper (left), and the CW, lower (right), rotors [30].	59
4.59	207 RPM rotor lift distribution for both the CCW, upper (left), and the CW, lower (right), rotors [30].	59
4.60	179 RPM rotor lift distribution for both the CCW, upper (left), and the CW, lower (right), rotors [30].	59
4.61	Peak OASPL vs. rotor RPM/ M_{AT} for a full sphere of observer locations 10 rotor radii from the coaxial rotor hub, halfway between the two rotors [30].	60
4.62	Blade section comparison of thickness acoustic pressure at the forward $\psi=180$ deg. observer location	62
4.63	Dual-swept tip blade configuration [30].	63
4.64	“Anti-Symmetric” dual-swept tip blade configuration [30].	63
4.65	Curved-swept tip blade configuration.	64
4.66	“Anti-Symmetric” curved-swept tip blade configuration.	64
4.67	Blade design comparison of thickness acoustic pressure at in-plane observer locations.	65
4.68	Blade design comparison of thickness acoustic spectra at in-plane observer locations.	66
4.69	Blade design comparison of thickness acoustic pressure at in-plane observer locations.	66
A.1	‘GEOMETRY_INPUT’ Example.	75

List of Symbols

c	speed of sound
p	pressure
p'	acoustic pressure, $p - p_0$
ρ	density
\hat{n}	unit normal vector of surface
dS	differential element of surface, S
v	local source surface velocity
u	local fluid velocity
ψ	azimuth angle
$\delta(f)$	Diract Delta
T_{ij}	Lighthill stress tensor
$H(f)$	Heaviside step function
t	observer time
τ	source time
r	distance from source to observer
M	local Mach number
M_{AT}	advancing tip Mach number
f	implicit function defining source surface
L	force per unit area on surface
L_M	force per unit area within a moving frame
P_{ij}	compressive stress tensor

\vec{x} observer position vector

θ elevation angle

Subscript

0 value in the undisturbed medium

r value in the observer direction

n value in the direction normal to surface

T thickness noise component

L loading noise component

ret evaluated at retarded time, $\tau = t - r/c$

Acknowledgments

First and foremost, I must thank my thesis advisor, Dr. Kenneth Brentner, for all he has taught me and helped me with throughout my graduate studies. I have learned far too much to be specific but I can say that a large part of the knowledge I have gained and the good work habits I have acquired are because of him. I also must thank both George Jacobellis and Professor Farhan Gandhi at RPI for providing me with the data necessary to conduct this research.

Secondly, I would like to thank Dr. William Warmbrodt and the entire NASA Ames Aeromechanics Branch for an unforgettable and invaluable internship experience in the Spring of 2016.

Next, I would like to acknowledge and thank both my parents for their unending support and curiosity in what I do, which always makes me want to learn more so I can share more with them.

Finally, I know I would not be the man I am today without my soon-to-be wife, Lily. Her love and belief in me has driven me to achieve things unimaginable by my younger self and I cannot wait to see where our lives take us from here.

This research is partially funded by the Government under Agreement No. W911W6-11-2-0011. The U.S. Government is authorized to reproduce and distribute reprints notwithstanding any copyright notation thereon. The views and conclusions contained in this document are those of the authors and should not be interpreted as representing the official policies, either expressed or implied, of the U.S. Government.

Introduction

Ever since the unveiling of the first turboshaft engine-powered single main rotor helicopter in the early 1950's, helicopters have been widely used in military, commercial and industrial applications. Today, the helicopter's prominent role in modern aviation cannot be questioned. The ability to takeoff and land vertically, maintain steady hover, and fly forward, backward and laterally, puts the helicopter in an aircraft class of its own. As the helicopter has matured through the mid-twentieth century, mass production and utilization of these machines also occurred and the single main rotor, tail rotor aircraft, now known as the conventional helicopter, has been the standard helicopter design. This conventional helicopter uses one centrally-located large main rotor mounted on the aircraft that provides lift, thrust and directional control, and a rear, smaller, lateral-thrusting tail rotor that balances the torque of the main rotor and provides additional directional control.

Prior to the expansion of helicopter use in the 1950's, however, many of the experimental vertical takeoff and landing (VTOL) aircraft did not look like this. Designs with two equally sized main lifting rotors, such as coaxial (one rotor on top of another), side-by-side (one rotor on either side of the aircraft) or tandem (one rotor forward and one rotor aft) rotor configurations, were actually more popular in the initial development of helicopters [1]. The helicopter pioneers of the early twentieth century understood the need to balance the torque reaction from the lifting rotor(s) on the airframe (hence the common use of two counter-rotating rotors) but lacked key knowledge of rotorcraft aeromechanics to build efficient rotor systems and engines of that time did not have sufficient power to sustain vertical flight. Eventually, the conventional helicopter prevailed due to the relative simplicity of design, implementation, and control through the use of a single main-lifting rotor.

From the time that safe and sustained vertical flight was realized through this configuration, users have continually sought higher speeds. Consequently, many enhancements and modifications have been made throughout the second half of the twentieth century but physical limitations of the single main rotor in high-speed flight exist.

To understand these limitations, consider that as the helicopter rotor is spinning with a fixed rotation speed in forward flight, the velocity over the advancing blade is the sum of the rotational velocity and the aircraft velocity, and the velocity over the retreating blade is the difference between these velocities. Thus, as aircraft velocity increases, airflow over the advancing blade increases but airflow over the retreating blade decreases; both of which are problematic.

For conventional helicopter equilibrium, the advancing and retreating sides of the rotor must produce equal lift. Thus, as velocities on the advancing blade increase (increasing lift) but decrease on the retreating blade (decreasing lift), the retreating blade angle of attack must be increased to compensate for a loss of lift. At a certain point however, increasing the angle of attack results in a decrease in lift and retreating blade stall eventually occurs. Hence, in a high-speed flight condition, the majority of the lift is generated by the forward and aft regions of the rotor instead of the sides. On the advancing side, increasing aircraft velocity causes the advancing blade to approach the speed of sound and experience transonic flow, much before the aircraft itself does. This transonic flow results in compressibility effects: airfoil drag divergence, shock waves on the blades, and large increases in drag on the rotor.

Both of these physical phenomena, retreating blade stall and compressibility effects on the advancing blade, cause high vehicle vibrations and restrict the forward speed of the conventional helicopter. Even though there has been a strong desire for higher speeds on a conventional helicopter, Westland's (now Leonardo – Finmeccanica) G-Lynx still holds the conventional helicopter's maximum forward flight speed record of 216 kts. set 30 years ago in 1986 [2]. Therefore, to achieve faster flight speeds, alternative VTOL aircraft need to be considered.

1.1 Alternative Rotorcraft Configurations

Concurrent to the modifications made to the conventional helicopter design during the latter years of the twentieth century, alternative rotorcraft configurations were also being developed, with various degrees of success. In the following sections, three notable high-speed configurations are described: the compound helicopter, the tiltrotor and the lift-offset coaxial helicopter.

1.1.1 Compound Helicopter

The first of these VTOL aircraft attempting to achieve high speeds and the easiest to visualize, is the compound helicopter. For a helicopter, compounding indicates that, beyond the main rotor providing propulsive thrust and vertical lift, an auxiliary propulsion system (thrust compounding), lifting body (lift compounding) or both (full compounding) have been attached to the aircraft. Typically, this refers to adding one or more propellers or jet engines to the aircraft body for thrust compounding and adding one or more wings or an additional, counter-rotating rotor for lift compounding.

With thrust compounding, the main rotor is no longer required to produce all of the thrust for the helicopter. In effect, auxiliary thrust enables an offloading and a reduction in the forward tilt

of the main rotor at higher speeds. The main rotor can then optimally operate for lift production, delaying retreating blade stall, so faster forward flight speeds than before can be achieved.

By lift compounding, in the same manner as thrust compounding, the main rotor of the helicopter is offloaded by the auxiliary lifting surface, such that the main rotor is no longer required to produce all of the lift for the aircraft. As forward flight speeds increase, lift produced by this added surface also increases, such that the rotor lift limit is bypassed and the helicopter's flight envelope is expanded.

In a configuration with full compounding (both lift and thrust), portions of both the lift and the thrust are offloaded from the main rotor and the effects of both lift and thrust compounding are combined. Therefore, the threat of retreating blade stall is greatly relieved and the fully compounded helicopter can achieve even higher speeds than with only lift or thrust compounding, making it an ideal modification of the conventional helicopter.

Early in the 1960's, the U.S. Army funded Bell Helicopter to develop a high performance helicopter (HPH) in an effort to explore the current limits of the conventional helicopter, which became the Bell 533 HPH, pictured in Fig. 1.1 below. Throughout this study, auxiliary thrust (jet engines) and auxiliary lifting surfaces (wings) were added to the original Bell 533 conventional helicopter design to see the effects each had on the overall helicopter performance, specifically focused on maximum forward flight speed. The results were favorable; the Bell 533 reached an overall maximum top speed of 275 kts. and was the first rotorcraft to ever exceed 200 kts. [3]. More recently, companies like Piasecki Aircraft Corporation, with their X-49 SpeedHawk, and Eurocopter, with their X³, are implementing compound helicopters in an effort to achieve high speeds.



Figure 1.1. Bell 533 HPH, Bell Helicopter [3].

1.1.2 Tiltrotor

Another rotorcraft concept aimed at achieving higher speeds is the tiltrotor. This configuration generates required lift and thrust through the use of two rotors, typically mounted at the tips of fixed wings on either side of the aircraft. The rotors on a tiltrotor can operate in both a “helicopter” and an “airplane” mode. For vertical takeoff and landing, the rotors are aligned

vertically such that the rotors produce lift like helicopter rotors. As forward speed is gained, the rotors can progressively be tilted forward until aligned horizontally, allowing the rotors to generate propulsive thrust like airplane propellers, while the wings carry the required lift. Tilting the rotors like this in high speeds removes the threat of retreating blade stall from traditional vertical lifting rotors and high forward flight speeds can be achieved. However, the rotor diameter on a tiltrotor is generally smaller than desired for a helicopter, which causes the tiltrotor to have a higher disk loading (ratio of rotor thrust to rotor area) and a lower hover efficiency.

Bell Helicopter demonstrated the tiltrotor concept with the experimental tiltrotor, the XV-3, in the 1950's and 60's. Through the course of the XV-3's extensive flight and wind tunnel testing, it successfully transitioned from helicopter to airplane mode multiple times but significant design weaknesses were exposed, namely: recurring rotor/wing/pylon instabilities and the far distance between the engines and the rotors (fuselage to wingtips). These experiments with the XV-3 yielded invaluable knowledge that was later used to develop the XV-15, another research tiltrotor and the successor of the XV-3. The XV-15 solved the engine-rotor distance problem by moving the engines out to rotating pods at the wing tips and eliminated the rotor/wing/pylon issues by incorporating very stiff wings and pod-wing attachments into the design. Flight and wind tunnel tests confirmed these improvements and the XV-15 achieved superior forward flight speeds to the conventional helicopter, up to 301 kts. [4].

From the successful demonstration of the tiltrotor technology with the XV-15 program, Bell Helicopter and The Boeing Company together were granted funding to develop the V-22 Osprey, a military tiltrotor aircraft. The V-22, larger in size than the XV-15, is currently in service, primarily in the U.S. military, and has been for almost a decade. Pictures of each of these three tiltrotor aircraft can be seen in Fig. 1.2 below.



Figure 1.2. Bell XV-3, Bell XV-15, Bell-Boeing V-22 (from left to right) [4].

1.1.3 Lift-offset Coaxial Helicopter

Preceding both the compound helicopter and the tiltrotor, the coaxial helicopter has origins dating back to the 18th century. However, this rotorcraft configuration did not fly until the early twentieth century because coaxial helicopters are complex in design. With two rotors positioned on top of one another, contra-rotating, the coaxial rotor system is inherently more mechanically complex than a single main rotor and has unique design challenges to overcome such as avoiding

blade-to-blade strikes. In contrast, benefits of a coaxial rotor system include: built-in torque balance of the two rotors spinning in opposite directions, full aircraft directional control without a tail rotor through differential torque between the two rotors, and compactness compared to a conventional helicopter. A beneficial variation of a coaxial rotor system is a lift-offset coaxial rotor.

The term lift-offset refers to a specific form of lift compounding. By adding either a wing opposite the advancing blade of the main rotor disk or an additional counter-rotating rotor to the main rotor system, the regions of high lift from large dynamic pressures on the rotor's advancing side are offset by equally high lift regions on the opposite side of the aircraft and a lift-offset helicopter configuration is realized. In a conventional helicopter configuration, the lift from the advancing blades has to be balanced by the lift from the retreating blades, limiting the maximum lift that can be produced on the advancing side. A lift-offset rotor removes this limitation. Specifically, a coaxial rotor system utilizing lift-offset, first developed by the Sikorsky Aircraft Corporation and named the Advancing Blade Concept (ABC), is a notable lift compounding technique to overcome the issue of retreating blade stall and the dissymmetry of lift of a conventional rotor system [5].

An ABC rotor system capitalizes on the availability of large dynamic pressures and substantial rotor lift on the advancing side of a rotor disk by using coaxial, contra-rotating rotors. In this rotor configuration, simultaneous advancing blades on both sides of the aircraft generate lift, which results in a roll moment balance of the rotor system. Additionally, the lift distribution of an ABC rotor system is different from that of a conventional rotor system because the majority of the aircraft's lift is generated by the two advancing blades (even in high-speed conditions) and the retreating blades are offloaded. This offloading eliminates the threat of retreating blade stall and therefore enables high forward flight speeds to be achieved. Moreover, additional speed can be gained with thrust compounding. Side mounted jet engines or aft-mounted propellers (since tail rotor can be removed) are examples of thrust compounding on a coaxial system enabling higher flight speeds.

However, these advantages of a lift-offset coaxial rotor system do not come without design challenges. In order to withstand the significant hub moment generated by the large lift forces on each advancing blade, a rigid hub with closely spaced rotors needs to be used. Consequently, the rotor blades must also be substantially stiffened as compared to conventional rotor blades to avoid having the blades hit one another. Earlier coaxial rotor models, like those employed by the Russian rotorcraft manufacturing company, Kamov, did not allow large moments to be carried in the rotor hub, thus a lift-offset rotor was not possible and forward flight speed capability of their coaxial models has been limited to 170 kts. [6].

Sikorsky Aircraft Corporation first demonstrated the advancing blade concept on their compound lift-offset coaxial helicopter, the XH-59. With two, closely spaced, contra-rotating rotors and side-mounted jet engines for auxiliary propulsion, the XH-59 achieved a forward flight speed of 238 kts. but experienced significant vibrations at high speeds [7]. Learning from the XH-59 experience, Sikorsky more recently developed another ABC demonstrator called the X2, which

improved on the XH-59 by adding a vibration reduction system, fly-by-wire (electronic), rather than mechanical, controls and a pusher propeller instead of side jet engines. With these design changes, high-speed vehicle vibrations were reduced and an even higher forward flight speed (higher than the XH-59), of 250 kts. was reached [8]. Both the XH-59 and the X-2 can be seen in Fig. 1.3.



Figure 1.3. Sikorsky XH-59, Sikorsky X-2 (from left to right) [8].

1.2 Future of Vertical Lift (FVL)

Armed with knowledge of advanced capabilities from alternative rotorcraft configurations, such as the tiltrotor and the compound lift-offset coaxial helicopter, the U.S. Army has taken a keen interest in replacing their current rotorcraft fleet. These new innovations have led them to establish the Future of Vertical Lift (FVL) program, which looks to capitalize on the most advanced technologies for VTOL aircraft. The Army’s requirements for FVL aircraft include: a forward flight speed of 230 kts., the ability to transport at least 12 troops, operate in 95 degrees Fahrenheit temperatures and altitudes of 6,000 ft (known as “high-hot” conditions), and have a minimum combat radius of 424 km (263 mi) [9]. By the end of the FVL program, it is presently anticipated that one, scalable design will make up a family of rotorcraft, with Joint Multi-Role (JMR) capability, to fulfill most of the Army’s rotorcraft needs. To date, two competing teams have received contracts to build a JMR Technology Demonstrator (JMR-TD): Bell Helicopter with their V-280 Valor tiltrotor and a joint effort between Boeing and Sikorsky for their SB>1 Defiant compound lift-offset coaxial helicopter design, both pictured in Fig. 1.4. The V-280 Valor and the SB>1 Defiant are based on previous technologies from the V-22 and the X-2, respectively, and are set to fly in 2017 to compete for the Army’s contract [10].

1.3 Research Motivation

As the first flight for these JMR-TD aircraft quickly approaches, there is a desire for detailed analysis and understanding of each rotorcraft concept. For the V-280 Valor, the tiltrotor has been studied for a long time and much more operational experience is available from the V-22 program, so, it should be understood in greater depth. The SB>1 Defiant, however, is based



(a)



(b)

Figure 1.4. (a). Bell Helicopter V-280 Valor (b). Boeing/Sikorsky SB>1 Defiant [9].

on two technology demonstrator aircraft, where much of the design's capability and scalability remain unknown. Even more so, the aeromechanical environment of a lift-offset coaxial rotor system is sure to be complex, especially in high-speed flight. The intra-rotor interactions of each rotor in isolation, along with the additional complexity of rotor-rotor interference, from one rotor to another, sets up a multifaceted problem. Acoustically, these phenomena will strongly influence noise and will generate unique noise signals unlike previous rotorcraft designs, particularly at high speeds. These expected acoustic characteristics are yet to be studied in the open literature. Therefore, this research work focuses on the acoustics of a compound lift-offset coaxial rotor system in high-speed flight.

1.3.1 Previous and Ongoing Work

Coaxial rotor configurations like the SB>1 Defiant have been and currently are being researched; however, the acoustics of this rotorcraft configuration in high-speed flight have not. Relevant studies involving coaxial rotors are highlighted below.

In 1983, Mosher and Peterson conducted a full-scale acoustic test of Sikorsky's XH-59 in the NASA Ames 40- by 80-Foot Wind Tunnel [11]. In this test, relatively low tunnel wind speeds

between 89 and 142 kts. were considered and unfortunately, the microphone array was determined to be too spread out to identify any specific acoustic characteristics. More recently in 2005, Boyd, et al. studied the acoustics of a notional coaxial rotor system consisting of two BO-105 model rotors [12]. This coaxial rotor system was not a lift-offset coaxial rotor, since the hub moments were trimmed to zero, and the maximum forward flight speed tested was 120 kts. In a series of studies, Kim, Duraisamy, and Brown have researched the acoustics of a generic compound lift-offset coaxial helicopter but flight speeds have been limited to 70 kts. and below [13, 14]. Currently, Barbely is simulating and validating the flow field and aerodynamic characteristics of a coaxial rotor system as a precursor to acoustic studies, with the end goal of eventually understanding the aeroacoustics and mitigating the noise signal of a coaxial configuration [15].

Addressing high-speed coaxial rotors, Jacobellis, et al. developed a model of Sikorsky's XH-59 in the Rotorcraft Comprehensive Analysis System (RCAS) to examine how control redundancies could be exploited to minimize the power requirements and hub vibrations [16]. One of the computational results from this study indicated that optimized trim settings, for a flight speed of 250 kts., reduced total power requirements by approximately 17% by reducing the main rotor RPM by 27% and decreasing the differential lateral pitch by 5 deg. Aerodynamically, Passe, et al. created a notional X2 model for use in coupled CFD/CSD (Computational Fluid Dynamics/Computational Structural Dynamics) framework to explore the interactional effects of compound coaxial rotorcraft, focusing on rotor-rotor and rotor-fuselage aerodynamic interference, in forward flight for speeds up to 150kts. [17]. Walsh and the Sikorsky flight test team evaluated the X2 technology demonstrator at high airspeeds, up to 250 kts., but the publically available acoustics data did not fully characterize the unique rotor configuration [18]. Likewise, Schmaus and Chopra performed comprehensive analysis of a high advance ratio coaxial helicopter but did not specifically address noise [19].

1.4 Scope and Organization of Thesis

Though a number of researchers have studied this complex coaxial rotor problem, few have focused on high-speed flight conditions (at least publicly) and even fewer on the acoustics. Therefore, the scope of this master's thesis is to produce a low-fidelity computational investigation of the noise characteristics of a $SB > 1$ Defiant-like coaxial helicopter in high-speed forward flight, as well as identify and explain a few concerns and/or benefits of a coaxial configuration as they apply to noise. Additionally, this analysis explores the use of design variables inherent to a coaxial helicopter configuration of this kind to reduce and/or control the directivity of the noise.

In the process of this research, a few original contributions were generated. Namely, a series of blade planform changes for improved acoustic performance of a coaxial rotor system were introduced. These new coaxial rotor blade configurations reduced the strength of the original acoustic signal during this low-fidelity study but a more comprehensive study needs to be conducted to substantiate the magnitude of their acoustic benefit.

With the overarching goal of identification and characterization of the noise unique to a

compound lift-offset coaxial helicopter in high-speed flight and exploring potential options to alter the noise signal, this thesis is organized as follows:

- The second chapter provides a background in rotorcraft acoustics, the acoustic theory used in this study and how this theory applies specifically to a compound lift-offset coaxial rotor system.
- The third chapter describes the simulation framework and acoustic methodology used to achieve the desired goals.
- The fourth chapter is a comprehensive account with presentation and in-depth analysis of all results gathered during this work.
- The fifth chapter summarizes all of the research completed in this effort and proposes potential future research.

Rotorcraft Acoustics Background

Before examining the unique acoustic characteristics of a compound lift-offset coaxial rotor configuration, it is helpful to review rotorcraft acoustics and the various noise sources involved in helicopter rotor noise, and then identify the specific noise sources likely to be important for coaxial rotor noise.

Rotorcraft of all types are inherently complicated vehicles with rotors that operate in an extremely complex aeromechanical environment. As such, the many moving rotor surfaces within this environment contribute to aerodynamic noise generation in the form of both discrete frequency and broadband noise. Rotational noise, blade-vortex interaction (BVI) noise and high-speed impulsive (HSI) noise are the typical deterministic components of discrete frequency noise. Broadband noise, on the other hand, includes the non-deterministic loading sources like: turbulence ingestion noise, blade-wake interaction noise and blade self-noise. Other noise sources not included in these two categories, such as engine noise and drivetrain and gear noise, can also be significant rotorcraft noise sources. In this initial investigation of compound lift-offset coaxial helicopter noise, only the rotational noise contribution (thickness and loading noise) to discrete frequency noise will be considered. The next section will review the theory for discrete frequency noise sources. For more information on the other types of rotorcraft noise, please refer to [20, 21, 22].

2.1 Discrete Frequency Noise

Rotorcraft discrete frequency noise consists of rotational noise, BVI noise and HSI noise. The rotational noise is split up into two categories known as thickness noise and loading noise, which are both related to linear aerodynamic theory. The displacement of fluid in the flow field by the rotor blade generates thickness noise, while the accelerating force on the fluid created by the blade motion causes loading noise. Loading noise in this context refers to the lower frequency harmonic portion of the overall loading noise; the impulsive loading noise caused by BVI and the

non-deterministic loading noise of broadband noise are studied as separate noise components.

Both BVI noise and HSI noise are severe rotorcraft noise sources that are highly impulsive and occur at the blade passage frequency. BVI noise is caused by a rotor blade interacting with a shed tip vortex from a blade that preceded it in rotation. This interaction, especially when the orientation of the tip vortex and the blade is parallel or nearly parallel, causes rapid pressure fluctuations on the blade, which results in this impulsive loading noise. BVI noise can occur on both the advancing and the retreating side of a rotor and, in certain flight regimes, such as descending flight, can continually occur. When it does occur, BVI noise is highly directional and this directivity depends on the orientation of the interaction. In particular, BVI noise that radiates from the advancing blade is directed down and forward of the rotorcraft, while BVI noise that radiates from the retreating blade is directed down and aft of the rotorcraft. In a coaxial configuration, BVI noise could be very important; the two rotors are capable of self-generated BVI noise and it is possible that tip vortices from one rotor interact with a blade from the other rotor.

HSI noise could also be important for a compound lift-offset coaxial helicopter. As high advancing-tip Mach numbers (M_{AT}) are achieved, near sonic speeds, shocks form in the volume surrounding the blade and this high-intensity noise, known as HSI noise, radiates within the rotor plane. HSI noise is sensitive to changes in M_{AT} ; the noise dramatically increases with small changes in M_{AT} . The signal from this noise is characteristically saw-tooth in shape; hence, very impulsive, and shocks can extend into the far-field (far away observers). For a compound lift-offset coaxial helicopter, HSI noise may be significant because the M_{AT} could be high at high forward flight speeds. However, in order to predict HSI noise, detailed flow field information is needed, thus this noise source is not included in this initial investigation.

Each of these discrete frequency noise sources has a general directivity of sound propagation when they occur. Displayed in Fig. 2.1 is the typical radiation direction of various types of rotor noise.

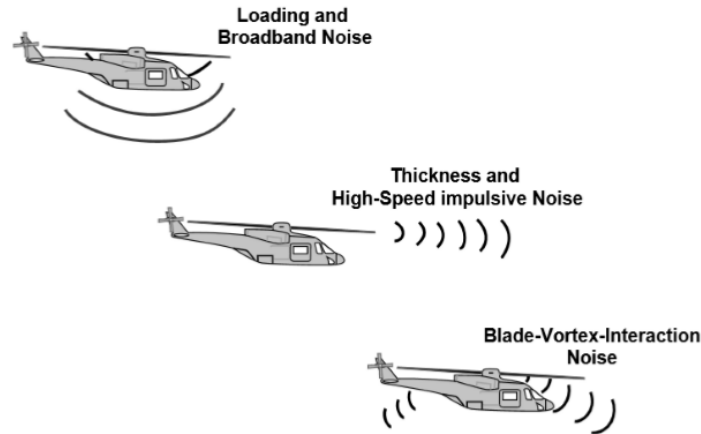


Figure 2.1. Typical directivity of various rotorcraft noise sources [22].

2.2 Review of Acoustics Theory

The various types of rotor noise discussed in the previous section can be understood in a more precise way by considering the acoustic source terms in the context of the governing equation. In 1969, Ffowcs Williams and Hawkings (FW-H) derived the governing equation for noise predictions involving surfaces in arbitrary motion by rearranging the Navier-Stokes equations to create an inhomogeneous wave equation [23]. The resulting formulation can be written as:

$$\begin{aligned} \left(\frac{1}{c_0^2} \frac{\partial^2}{\partial t^2} - \frac{\partial^2}{\partial x_i \partial x_i} \right) p'(\vec{x}, t) = & \frac{\partial}{\partial t} \{ [\rho_0 v_n + \rho(u_n - v_n)] \delta(f) \} \\ & - \frac{\partial}{\partial x_i} \{ [\Delta P_{ij} \hat{n}_j + \rho u_i(u_n - v_n)] \delta(f) \} + \frac{\partial^2}{\partial x_i \partial x_j} [T_{ij} H(f)] \end{aligned} \quad (2.1)$$

where c_0 , ρ_0 , and p_0 are the speed of sound, density and pressure of the undisturbed medium, respectively; p' is the acoustic pressure ($p - p_0$), and ρ is the fluid density. Also, v_n and u_n are the normal components of the local source surface velocity and the fluid velocity, respectively, P_{ij} is the compressive stress tensor, T_{ij} is the Lighthill stress tensor, $\delta(f)$ is the Dirac delta function and $H(f)$ is the Heaviside function. Both $\delta(f)$ and $H(f)$ use the implicit function, f , which is defined as:

$$f = \begin{cases} < 0 & \text{Within the data surface} \\ 0 & \text{On the data surface} \\ > 0 & \text{Outside the data surface} \end{cases} \quad (2.2)$$

The three terms on the right hand side of the FW-H equation, Eq. (2.1), have mathematical characteristics of monopole (thickness noise source), dipole (loading noise source) and quadrupole source terms, respectively.

Farassat later established an integral representation of the solution to the FW-H equation, known as Formulation 1A, which neglects the quadrupole source terms, as follows:

$$p'(\vec{x}, t) = p'_T(\vec{x}, t) + p'_L(\vec{x}, t) \quad (2.3)$$

with p'_T , the thickness contribution, written as:

$$4\pi p'_T(\vec{x}, t) = \int_{f=0} \left[\frac{\rho_0(\dot{v}_n + v_n)}{r(1 - M_r)^2} \right]_{ret} dS + \int_{f=0} \left[\frac{\rho_0 v_n (r \dot{M}_r + c_0 M_r - c_0 M^2)}{r^2 (1 - M_r)^3} \right]_{ret} dS \quad (2.4)$$

and p'_L , the loading contribution, written as:

$$4\pi p'_L(\vec{x}, t) = \frac{1}{c_0} \int_{f=0} \left[\frac{\dot{L}_r}{r(1 - M_r)^2} \right]_{ret} dS + \int_{f=0} \left[\frac{L_r - L_M}{r^2(1 - M_r)^2} \right]_{ret} dS \\ + \frac{1}{c_0} \int_{f=0} \left[\frac{L_r(r\dot{M}_r + c_0 M_r - c_0 M^2)}{r^2(1 - M_r)^3} \right]_{ret} dS \quad (2.5)$$

where r is the distance between the source and the observer, M_r is the Mach number in the radiation direction (from the source point to the observer), M is the Mach number of the surface $f = 0$, and a dot above a variable represents the source time derivative of that variable. For Eq. (2.5) specifically, the new variable to note, L , is the local force per unit area, with two subscripts: r , to denote the radiation direction, and M , to indicate the forces are in a moving frame [22]. The $[\]_{ret}$ denotes that each integrand is evaluated at the retarded/source time, the time the sound is emitted. However, the discrete integral summations occur at a constant observer time, the time that the emitted signals all reach the observer. This is a subtle, yet important, concept to understand in acoustic studies. As a result of the difference distances to the observer from each source point on the blade (or other surface) and a constant speed of sound, signals emitted simultaneously from a surface do not simultaneously reach a fixed observer. Instead, since these signals travel different distances at the same speed, emitted sound from closer source points arrive at the observer first, while those from farther source points arrive later. Therefore, the noise that reaches the observer at a particular observer time, t , is from all the source points on the rotor blade, emitted at different source times.

2.3 Coaxial Acoustic Consideration

A review of Farassat's Formulation 1A, Eqs. (2.3)-(2.5), is useful because the computational acoustics software used in this study, PSU-WOPWOP, numerically solves Eqs. (2.3)-(2.5). By examining these equation, potential issues specific to compound lift-offset coaxial helicopter noise can be identified.

First, consider the terms on the right hand side of the thickness equation, p'_T , Eq. (2.4). For a coaxial helicopter, higher forward flight speeds than a conventional helicopter are possible, resulting in potentially larger Mach numbers for a given RPM. These high Mach numbers would cause a large increase in the thickness acoustic pressure due to the Doppler amplification (a result of the $1/(1 - M_r)$ terms as M_r approaches 1) in Formulation 1A. However, the rotor rotation speed of a compound lift-offset coaxial helicopter is often variable and can be decreased, potentially alleviating this initial high-speed concern.

Likewise, the presence of a second rotor introduces additional acoustic considerations. For example, on a conventional helicopter in forward flight, with an observer directly ahead of the

helicopter in the rotor plane, the largest source of noise is the advancing blade because of the high Mach number and thus, a high Doppler amplification. When considering a lift-offset coaxial helicopter in the same scenario, there are often two blades advancing simultaneously and these large acoustic signals will add, resulting in constructive interference. For other observer locations and situations, similar constructive or destructive interferences between the acoustic signals from both rotors are likely to occur (to a varying degree depending upon observer location).

For the terms on the right hand side of the loading equation, p'_L Eq. (2.5), the effect of the Mach number and Doppler amplification are still relevant as in the case of thickness noise, but, there are additional terms in the numerator to consider. Namely, the loading variables, \mathbf{L} and $\dot{\mathbf{L}}$, will have a very different radial and azimuthal distribution as compared to a conventional helicopter and are likely to be impulsive in certain areas on the rotor disks due to expected interactions such as: BVI within each rotor, rotor-wake interactions and the unsteady aerodynamics caused by the close interaction when the blade of the upper and lower rotors pass (or cross) each other at various locations around the azimuth. Any impulsive loading is of particular concern in acoustics because the numerator term $\dot{\mathbf{L}}$, is the time derivative of the loading, which would magnify any impulsive signals and result in a spike in loading acoustic pressure.

Noise Prediction Methodology

In order to compute the noise of a compound lift-offset coaxial helicopter in high-speed flight, two analysis tools are coupled: PSU-WOPWOP and the Rotorcraft Comprehensive Analysis System (RCAS). The rotor noise prediction program, PSU-WOPWOP, numerically solves Farassat's Formulation 1A of the Ffowcs Williams-Hawkings equation, Eqs. (2.3)-(2.5), and requires the rotor blade motion, the rotor blade surface geometry and the rotor blade loading as input. The rotor blade surface geometry is generated by a code known as BladeMaker, while the rotor blade loading is generated by RCAS. Together, the blade surface geometry from BladeMaker and the blade loading data from RCAS are input to PSU-WOPWOP, along with an input file defining the blade motion, for acoustic prediction. A brief description of RCAS and PSU-WOPWOP are provided in this chapter and a description of BladeMaker is included in Appendix A. A detailed explanation of the integration process of RCAS and PSU-WOPWOP is included in Appendix B.

3.1 Rotorcraft Comprehensive Analysis System (RCAS)

The Rotorcraft Comprehensive Analysis System (RCAS) was used to simulate the rotor blade loading in this research. RCAS is a tool developed by Advanced Rotorcraft Technology Inc. for the U.S. Army, to enable research, design and engineering of arbitrary rotorcraft configurations [24]. Within RCAS, users are able to define a variety of rotor configurations for modeling in hover, forward-flight and maneuvering flight conditions.

Aerodynamically, RCAS enables the modeling of each component of a rotorcraft system: rotor blades, fuselage, empennage, etc. For this thesis and for the loading noise calculations, only the loading on the rotor blades was of interest. In order to solve for the rotor blade loading, RCAS divides the rotor blades into separate segments and computes the forces at discrete points on those segments through the use of basic lifting line theory, where each segment is treated as a two-dimensional airfoil. The calculation of these forces require that the local flow velocity at each point be determined. From the local velocity components, the angle of attack and Mach number

at each point can be determined, which then enable the lift, drag and pitching moment to be generated from the specified airfoil characteristics. Establishing the local flow velocity for these calculations depends on the motion of the blades and the inflow velocity components, which are provided by a rotor inflow model. Rotor inflow models estimate or predict the inflow velocity into the rotor.

Acoustically, the inflow model is important because the inflow velocities influence the local velocities, which affect the loading on the blades. Those forces on the blades are then directly used in the loading noise calculations and the blade loading details affect the loading acoustic pressure. Thus, the accuracy of the inflow model plays a role in the accuracy of the loading noise predictions.

Within RCAS, there are four types of aerodynamic inflow models: momentum theory, generalized dynamic inflow theory, prescribed wake, and free wake. However, the RCAS simulations for this research work were completed by research partners at Rensselaer Polytechnic Institute (RPI) and the output from RCAS was provided to the author. The two inflow models used by RPI were the generalized dynamic inflow model and the prescribed wake model. Therefore, only the generalized dynamic inflow model and the prescribed wake model were used in this research work and are discussed in the following sections.

3.1.1 Generalized Dynamic Inflow

The dynamic inflow model in RCAS is based on the unsteady theory of Peters and He and assumes an inviscid, incompressible, and irrotational flow. The form of the inflow into the rotor disk is also assumed by this model and is governed by a set of differential equations. The dynamic inflow model has been widely used and can be computationally efficient [25]. However, with the assumptions of the dynamic inflow model, only the flow moving perpendicular to the rotor disk can be accounted for, such that the chordwise and spanwise flow characteristics are missed. Moreover, the vorticity of the rotor wake is also not included in this model, which would affect the inflow velocities and thus, the calculated blade loading.

3.1.2 Prescribed Wake

The prescribed wake model, unlike the dynamic inflow model, does not assume the form of the inflow, but instead, models the geometry of the tip vortices, the wake sheet and the strength of the inflow based on the operating condition of the helicopter. The geometry and strength are taken from a database of measurements or computations of a single rotor helicopter and are used to compute the influence on the inflow into the rotor. Moreover, the irrotational assumption is also removed in the prescribed wake model and vorticity of the wake is included. In effect, the Biot-Savart law is applied to obtain the rotor inflow velocities and thus, vorticity effects in the rotor wake are accounted for in the calculation of the blade loads. Inclusion of vorticity is important for blade load computations because vorticity can greatly affect the rotor inflow and consequently, the blade loads. Spanwise and chordwise flow is also included in the prescribed

wake model, which, when present, will influence the blade loads as well. Overall, the prescribed wake model should generate more representative blade loading than the dynamic inflow model by capturing the additional flow phenomena described in this section. Therefore, prescribed wake modeling was used in this research to simulate the rotor blade loading.

3.2 PSU-WOPWOP

PSU-WOPWOP, Refs. [26, 27, 28], is a rotor noise prediction software that numerically solves Farassat's Formulation 1A, Eqs. (2.3)-(2.5). As input, PSU-WOPWOP requires a time history of the rotor blade motion, the rotor blade geometry and the rotor blade loading. In this thesis, the rotor blade motion for PSU-WOPWOP is specified by an input file, while the rotor blade geometry and the rotor blade loading are generated by external tools: BladeMaker and RCAS, respectively. Additionally, noise predictions require specified locations at which the noise predictions occur, known as observer locations. Observer locations for PSU-WOPWOP can be defined within the same input file as the blade motion or in an external file defining a grid of observer locations. For noise prediction, the observer location determines the distance and the direction that sound radiates from the source to the observer and is, therefore, a necessary parameter for evaluating Formulation 1A.

From the input of blade motion, blade geometry and blade loading, as well as specified observer locations, PSU-WOPWOP can numerically solve Formulation 1A, Eqs. (2.3)-(2.5), presented here again for reference:

$$p'(\vec{x}, t) = p'_T(\vec{x}, t) + p'_L(\vec{x}, t) \quad (2.3)$$

with p'_T , the thickness contribution, written as:

$$4\pi p'_T(\vec{x}, t) = \int_{f=0} \left[\frac{\rho_0(\dot{v}_n + v_{\dot{n}})}{r(1 - M_r)^2} \right]_{ret} dS + \int_{f=0} \left[\frac{\rho_0 v_n(r\dot{M}_r + c_0 M_r - c_0 M^2)}{r^2(1 - M_r)^3} \right]_{ret} dS \quad (2.4)$$

and p'_L , the loading contribution, written as:

$$\begin{aligned} 4\pi p'_L(\vec{x}, t) = & \frac{1}{c_0} \int_{f=0} \left[\frac{\dot{L}_r}{r(1 - M_r)^2} \right]_{ret} dS + \int_{f=0} \left[\frac{L_r - L_M}{r^2(1 - M_r)^2} \right]_{ret} dS \\ & + \frac{1}{c_0} \int_{f=0} \left[\frac{L_r(r\dot{M}_r + c_0 M_r - c_0 M^2)}{r^2(1 - M_r)^3} \right]_{ret} dS \end{aligned} \quad (2.5)$$

In order to calculate the acoustic pressure, the derivative and rates of change in Eqs. (2.4) and (2.5) are computed first by PSU-WOPWOP using difference equations. Then, each integrand

is evaluated at the retarded time, denoted by *ret*, meaning the time that the sound is emitted from the rotor blades. Next, numerical integration is performed over each discrete point along the blade surface, the arrival time to the observer of each signal from those discrete points is computed and the signal is interpolated such that all the arrival times to the observer are the same for each integral summation. PSU-WOPWOP repeats then this process for each desired observer time and location until complete.

The surface geometry files for integration are recognized by PSU-WOPWOP as external patch files. These patch files contain each of the discrete points that PSU-WOPWOP integrates over during the evaluation of Formulation 1A and they are used to define the rotor blade geometry in this thesis. When complete information for integration (e.g. distributed loading over an entire blade surface) is not known, a compact patch can alternatively be used. Compact patches are one-dimensional (1-D) definitions of a rotor blade (spanwise locations) that have already been integrated in the chordwise direction by assuming the rotor blade is acoustically compact in the chordwise direction. By making this assumption, noise predictions can be made with simplified blade geometry and blade loading because distributed rotor blade information, such as geometry or loading, is no longer needed for a noise computation. In using compact patches, the overall computation time can be greatly decreased. Compact patches are utilized in this thesis to define the rotor blade geometry and loading for loading noise computation since the blade loads are known only as functions of span and azimuth (not chordwise).

Within PSU-WOPWOP, a variable method for defining surface and observer motion, called changes of base (COB), allows any type of source motion to be modeled. Example COB that were used in this work are described in Appendix C.

3.3 Discussion of Noise Prediction Approach

The coupling of RCAS and PSU-WOPWOP was used in this thesis to predict the noise of a compound lift-offset coaxial rotor system. However, that is not the only way this analysis could have been performed. Therefore, a discussion of this method and the rationale for the choice of these tools is presented. This work is intended to be an initial investigation of the noise generated by a compound lift-offset coaxial rotor system during high-speed flight. Thus, conscious consideration of both strengths and weaknesses of the individual tools and how they are used together will be useful for the reader to understand the conclusions of this research and will be helpful to guide future studies in this area.

3.3.1 Approach Weaknesses

The first weakness of this particular analysis (and, in the opinion of the author, the biggest one) is that the RCAS prescribed wake model cannot capture all of the physical phenomena associated with this coaxial rotor system. Specifically, because the geometry and strength of the prescribed wake inflow is based on a single rotor experiment or computation, it is unlikely

that the strength and location of the tip vortices and the wake sheet generated for each rotor in this coaxial rotor system will be correct. There has not been much, if any, data to account for coaxial rotor wake interactions and then develop prescribe wakes. Alternatively, a free-wake model would be an improvement on the prescribed wake model because the position and strength of the wakes are computed as part of the solution. With a free-wake model, a database of single rotor measurements or computations is not used and the influence of each rotor wake on the other can be included. Likewise, a computational fluid dynamics (CFD) solver calculates the strength and location of tip vortices and wake sheets but is much more computationally expensive. By using either a free-wake method or a high-fidelity CFD solver, the blade loading might reflect the missed interactions of the prescribed wake and more accurate blade loading is possible. Consequently, using blade loads or surface pressures from either a free-wake method or a CFD solution, respectively, to compute loading noise could provide more accurate results.

Another drawback of this coupling of RCAS and PSU-WOPWOP is that high-speed impulsive (HSI) noise, if it is significant, is not accounted for in these noise predictions. HSI noise, which occurs from shock-wave formation on the tips of advancing blades, could be highly important because of its impulsiveness, relative loudness and directivity (forward of the rotor plane). However, since a compound lift-offset coaxial helicopter can operate with a reduced rotor RPM and hence, advancing tip Mach number, HSI noise may not be an issue.

One underlying issue with this research is that the noise of a compound lift-offset coaxial rotor system has not been widely considered, particularly in high-speed flight. Thus, validation of these noise predictions against data cannot be done at this time.

3.3.2 Approach Strengths

Despite the weaknesses in this analysis, there are noteworthy strengths. From an RCAS modeling perspective, a prescribed wake model can capture key wake features of a compound lift-offset coaxial rotor system, such as the actual vorticity in the flow field (to some extent) and the vorticity's influence on the rotor inflow.

In execution, both RCAS and PSU-WOPWOP were computationally inexpensive and fast. This allowed extra time to be focused on analyzing results, rather than waiting on their computation, and permitted many different flight cases and coaxial helicopter configurations to be studied. Also, PSU-WOPWOP readily enabled a coaxial rotor to be modeled with no software modification, saving additional time.

Furthermore, although there is not much, if any, data to validate these coaxial rotor system noise predictions against, the tools used in this study have been widely used and validated for single rotors. Thus, there is some confidence in these results since they seem to make sense and change as expected under various flight conditions.

Coaxial Helicopter Acoustic Predictions

4.1 Explanation of Figures

Prior to the acoustic results of this study, a description of helicopter noise predictions and the manner in which these results are presented is helpful. The primary way acoustic results are displayed in this thesis are through acoustic pressure time histories with Acoustic Pressure (Pa) on the y-axis and Observer Time (s) on the x-axis. The Acoustic Pressure range for each plot is case dependent but, although the observer time range may change, each plot shows the signal from one full rotor revolution (unless specified otherwise). These acoustic pressure time histories are presented for both in-plane (within the rotor plane) and out-of-plane (below the rotor plane) observer locations, where the rotor plane is defined as a plane parallel to and halfway between the two rotors. Each in-plane plot contains 8 observer locations, equally spaced around the rotor azimuth, including directly aft, $\psi = 0$ deg. and directly forward, $\psi = 180$ deg., at a distance of 10 rotor radii (180 ft.) from the point on the shaft axis midway between the two rotor hubs. The out-of-plane plots show the results on a vertical plane that cuts through the centerline of the rotorcraft connecting $\psi = 180$ deg. and $\psi = 0$ deg. and on a vertical plane that cuts through a lateral line connecting $\psi = 90$ deg. and $\psi = 270$ deg. Each plot has 6 observer locations at elevation angles: -15, -45 and -75 deg. (negative denotes below the rotor plane) also at a distance of 10 rotor radii from the point on the shaft axis midway between the two rotor hubs. Examples of both the in-plane and out-of-plane plots are shown in Figs. 4.2 - 4.7. For reference, the azimuthal angles in this thesis are defined by the upper, counterclockwise-rotating rotor with $\psi = 90$ deg. corresponding to the side with the upper rotor's advancing blade (starboard side).

In a complimentary way, the acoustic spectra for all acoustic pressure time histories was computed and is displayed with SPL (dB) on the y-axis and Harmonic Number on the x-axis.

4.2 XH-59 Helicopter

For these acoustic predictions, the Sikorsky Aircraft Corporation's XH-59 aircraft was modeled in RCAS and the XH-59 lift-offset coaxial rotor system was the baseline for this research. The XH-59 was designed and built in the 1970's and served as the technology demonstrator for the ABC rotor system [29]. As shown in the schematic in Fig. 4.1, the XH-59 has two rigid rotors, an upper, counterclockwise (CCW) rotating rotor and a lower, clockwise (CW) rotating rotor. Both rotors have three stiff blades, each with a 20% root cut-out, composed of three airfoil sections (from root to tip, respectively): NACA 0026, 63-218, and 23012. The blade chord decreases from 20.7 inches at 20% span to 11.5 inches at the blade tips and the twist decreases from 4.6 deg. at 20% span to -3.8 deg. at the blade tips. During the rotors' rotation, the blade crossover locations (though variable) are originally assumed in this research to occur at $\psi = 0$ deg. and every 60 deg. from that around the azimuth, where ψ denotes the rotor azimuth angle and $\psi = 0$ deg. points directly aft of the helicopter. It should be noted that in the schematic in Fig. 4.1, the XH-59 has a blade crossover configuration of $\psi = 30$ deg. and every 60 deg. from that around the azimuth. For thrust compounding, the XH-59 has two auxiliary turbojets mounted on either side of the aircraft. Moreover this coaxial rotor configuration acts as a type of lift compounding, utilizing an ABC rotor system.

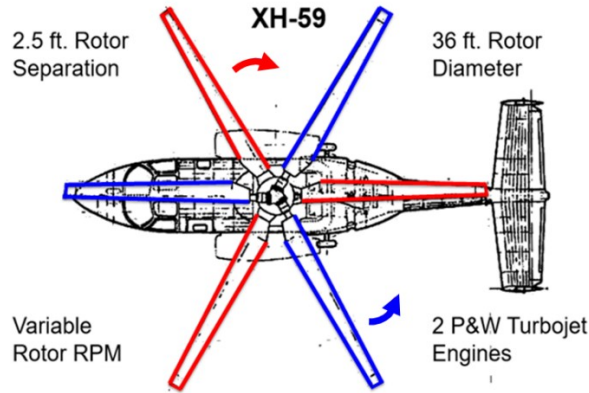


Figure 4.1. XH-59 Helicopter Schematic and Specifications [26].

4.3 Coaxial Noise Characteristics

As a first, exploratory look into compound lift-offset coaxial rotor noise, a representative flight condition for the XH-59 was considered to identify unique characteristics of both the thickness and loading noise. The aerodynamic and acoustic features of this configuration are expected to be more complex than that of a single main rotor aircraft. The intra-rotor interactions of each rotor in isolation, such as BVI events, along with the additional complication of rotor-rotor interference, such as blade crossover events and acoustic interferences, create an interesting aeroacoustic environment. In this section, an investigation into some of these complexities, with

a focus on specific notable characteristics of coaxial rotor noise is presented. In order to achieve this goal, the XH-59 was trimmed in RCAS with a 160 kts. forward flight speed, at 335 RPM, and an aircraft angle of attack of 4 deg., yielding an $M_{AT} = 0.8$.

4.3.1 Symmetry and Constructive/Destructive Interference

In Figs. 4.2 and 4.3, the in-plane thickness acoustic pressure and acoustic spectra are shown. From these figures, it can be seen that the sum of the thickness noise generated by each of the rotors is symmetric with respect to the centerline of the rotorcraft. This characteristic should hold true for all coaxial configurations assuming they have the same blade geometry, mirrored as appropriate for rotation in the opposite direction. The symmetry exists because the thickness noise is only a function of the blade geometry and operating conditions – not the blade loading. The impact of this symmetry is that the thickness noise is doubled on the plane of symmetry (e.g. 4.2 (b)). Generally, this property is applicable to the loading noise as well; however, the loading on the two rotors will not be identical, resulting in loading noise that is not exactly symmetrical.

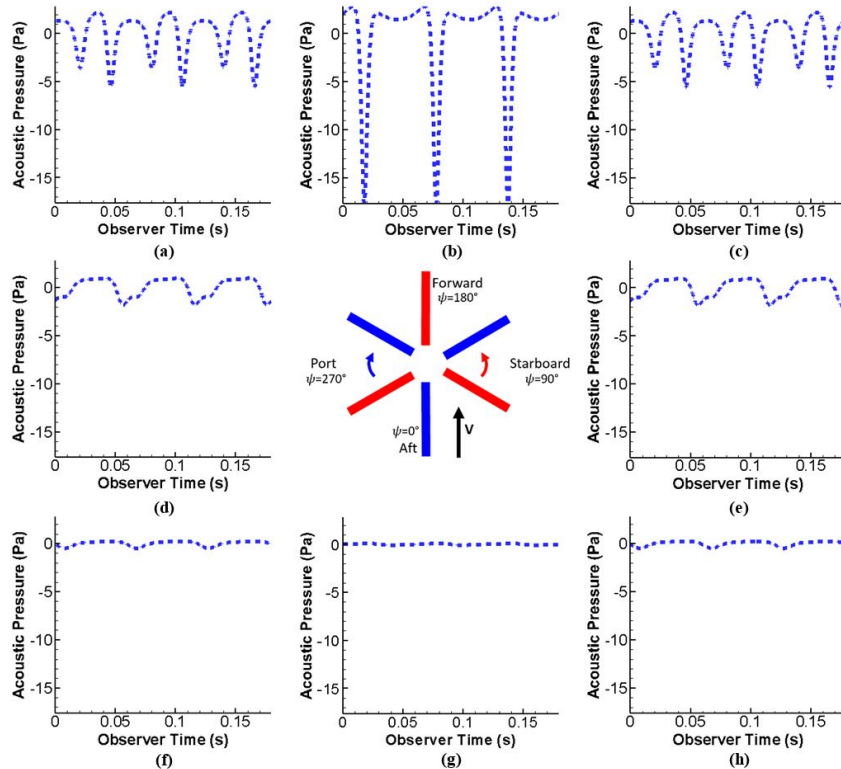


Figure 4.2. Coaxial thickness acoustic pressure at in-plane observer locations $\cdots\cdots\cdots\Diamond$ Coaxial [30].

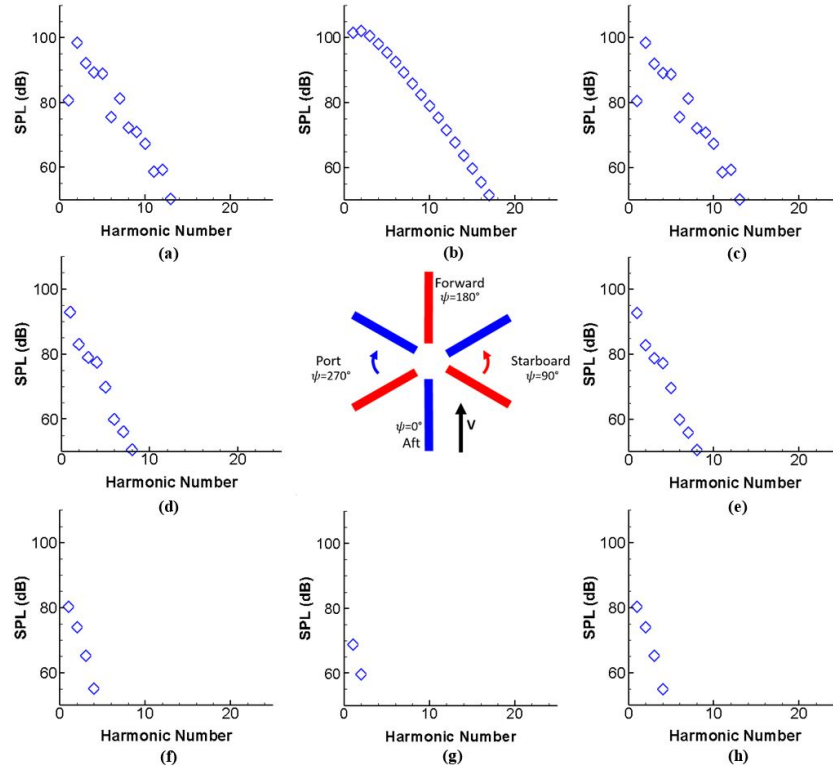


Figure 4.3. Coaxial thickness acoustic spectra at in-plane observer locations $\cdots\diamond$ Coaxial [30].

At locations off the plane of symmetry, the distance from the symmetric sources on each rotor to the observer are different; hence, there is a time delay and a decay for the more distant source (most noise comes from the blade tip region on the advancing sides of the rotors). This results in constructive and destructive interference between signals from each rotor. In Fig. 4.2, for observer locations that are not on the plane of symmetry (i.e., not (b) or (g)), the summation of the two rotor signals is evident. For instance, at observer location (c), there are three thickness noise pulses that are larger than the other three, due to spherical spreading of the signals, and the smaller pulses are not centered in time between the larger pulses because of a time delay of signals from the more distant sources. It is clear in Fig. 4.2 (b) there is constructive interference – the two signals add completely, which result in three large acoustic pulses. At other observer locations, a positive part of the acoustic pressure time history can add with the negative part of the other rotor signal; hence, destructive interference. The same effect is true for all rotor noise sources; however, thickness noise is very symmetric so the results are much more noticeable.

In Figs. 4.4 - 4.7, the out-of-plane thickness acoustic pressure and thickness spectra plots are shown. Although thickness noise amplitudes decrease significantly at out-of-plane observer locations, many of the same characteristics of in-plane thickness noise hold, especially the symmetry, the summation of individual rotor signals and constructive and destructive interference. These cases were computed and are presented mainly for completeness.

Figure 4.4. Coaxial thickness acoustic pressure at out-of-plane $\psi=0$ and 180 deg. observer locations
----- \diamond Coaxial.

Figure 4.5. Coaxial thickness acoustic spectra at out-of-plane $\psi=0$ and 180 deg. observer locations
----- \diamond Coaxial.

Note: Values are lower than 70dB at observer locations (b),(d),(e) and (f).

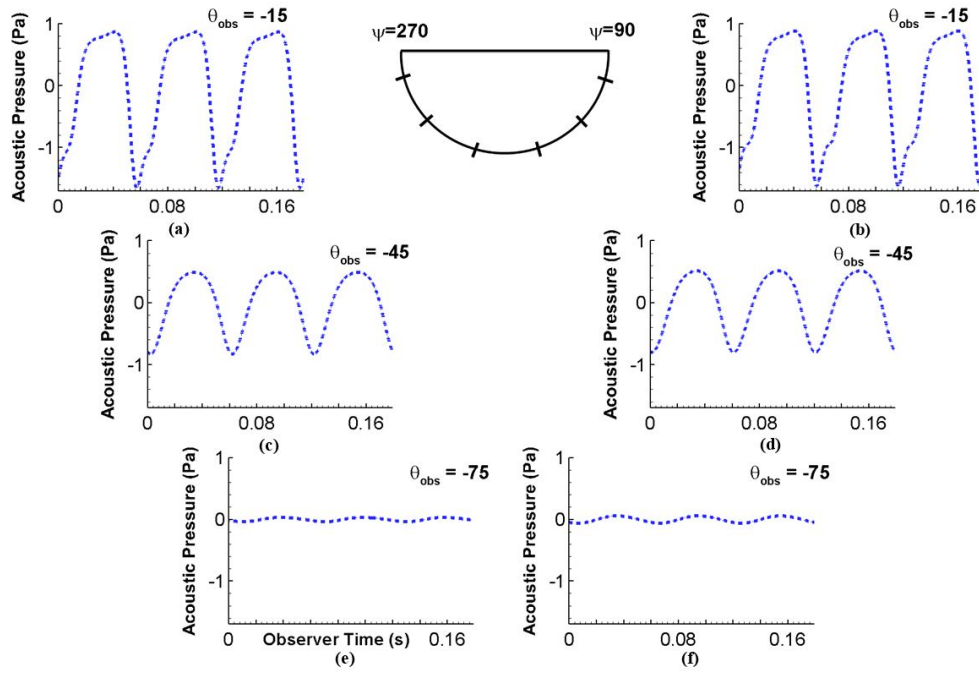


Figure 4.6. Coaxial thickness acoustic pressure at out-of-plane $\psi=90$ and 270 deg. observer locations
----- \diamond Coaxial.

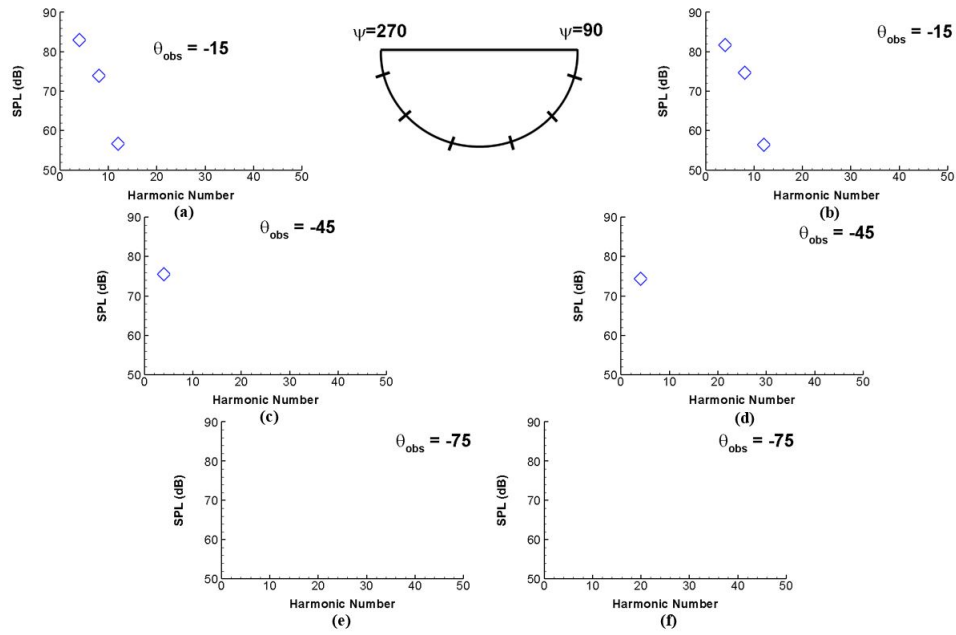


Figure 4.7. Coaxial thickness acoustic spectra at out-of-plane $\psi=90$ and 270 deg. observer locations
----- \diamond Coaxial.

Note: Values are lower than 50dB at observer locations (e) and (f).

4.3.2 Loading Noise: Blade Crossovers & BVI

Though the previous section focused primarily on thickness noise, the loading noise from a compound lift-offset coaxial rotor has unique properties as well. Fig. 4.8 shows the lift distribution (in lb/ft) on both the upper and lower rotors, respectively, as contour plots around the azimuth. On the advancing side of each rotor, above the $\psi = 0$ -180 deg. line for the upper rotor and below the $\psi = 0$ -180 deg. line for the lower rotor in Fig. 4.8, the loading experiences multiple instances of rapid loading change. In explanation, impulsive fluctuations are represented on this plot by quick changes in color level while moving in the direction of a rotor's rotation. A few likely causes of these events are BVI with a rotor's own tip-vortex; rotor-wake interactions between the two rotors; or the aerodynamic interference when the blades of the upper and lower rotors "cross". In addition, Fig. 4.8 highlights a lift-offset rotor feature that the majority of the lift is produced on the advancing side of the rotor disk, and, in this case, by inboard sections of the blades, rather than the blade tips.

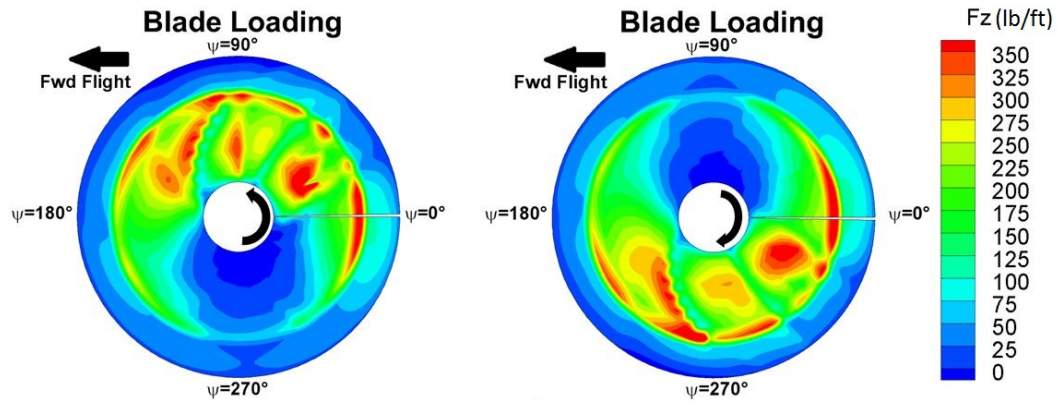


Figure 4.8. Upper, CCW (left) and lower, CW (right) rotor lift distributions for 160 kts. forward flight speed at 335 RPM [30].

From an acoustic perspective, there are at least two interesting characteristics in the blade loading to point out in Fig. 4.8. First, the rapid loading changes are very important and are likely to cause significantly strong and impulsive loading noise signals. Secondly, moving the loading inboard and away from the tip, causes the Doppler amplification to have a less predominant role (although this is generally not as important for loading noise).

In the same manner as the thickness noise plots, the in-plane and out-of-plane loading acoustic pressure and acoustic spectra are shown in Figs. 4.9 - 4.14 respectively. From the in-plane loading noise in Fig. 4.9, it is clear that the impulsive blade loading generated impulsive loading noise signals. Shown by both the sharp peaks of the acoustic pressure time histories and the high levels of high frequency content in the acoustic spectra, these loading noise signals are much more impulsive than the thickness noise signals. However, the relative levels of the in-plane loading noise are low, compared to in-plane thickness noise, so the impulsiveness may not be very significant in-plane.

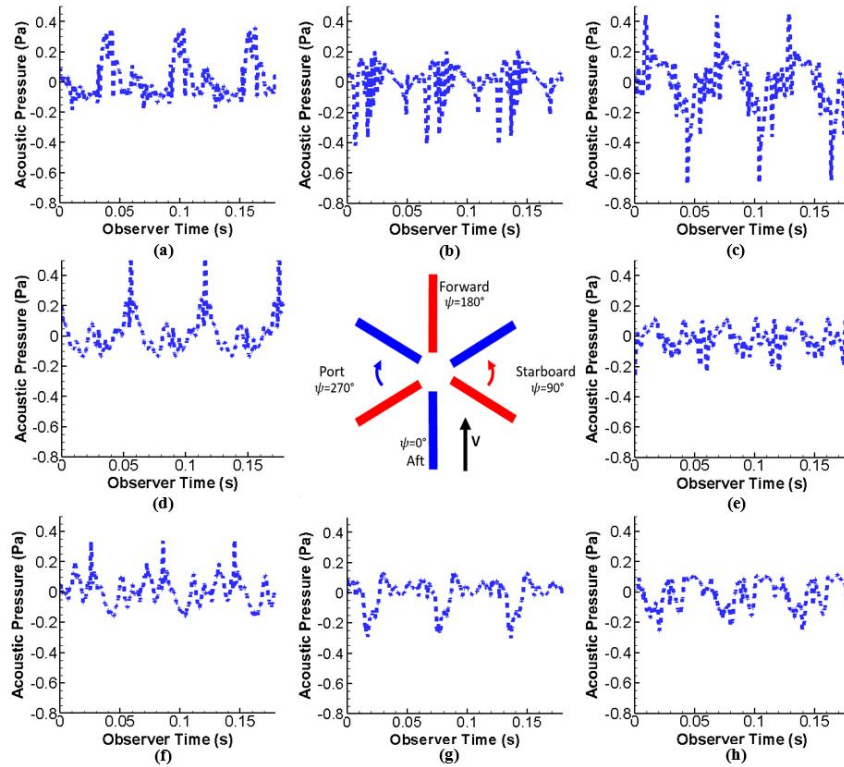


Figure 4.9. Coaxial loading acoustic pressure at in-plane observer locations $\cdots \diamond$ Coaxial.

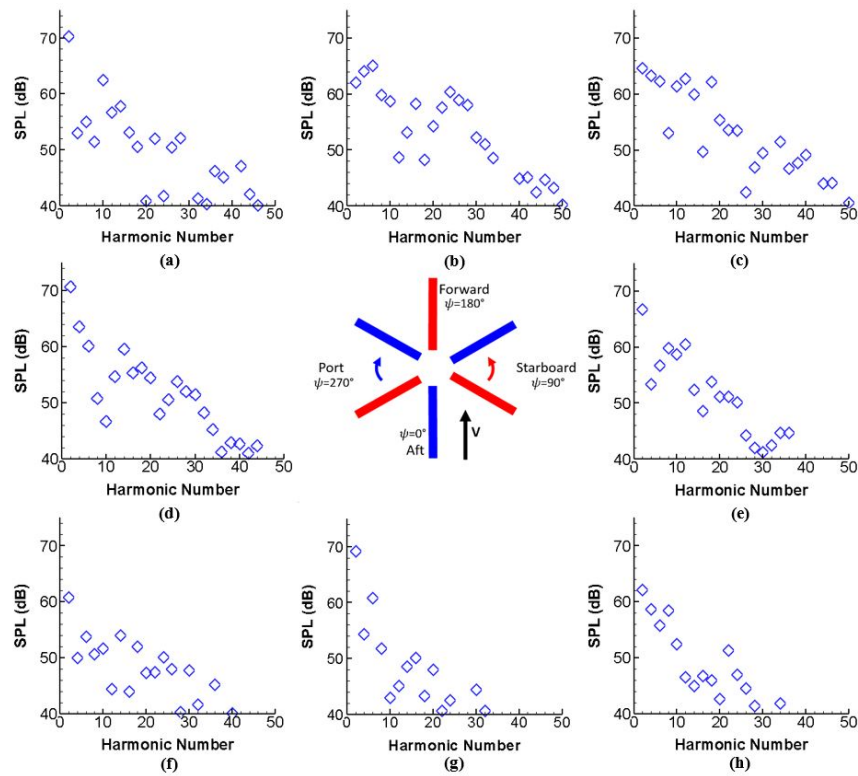


Figure 4.10. Coaxial loading acoustic spectra at in-plane observer locations $\cdots \diamond$ Coaxial.

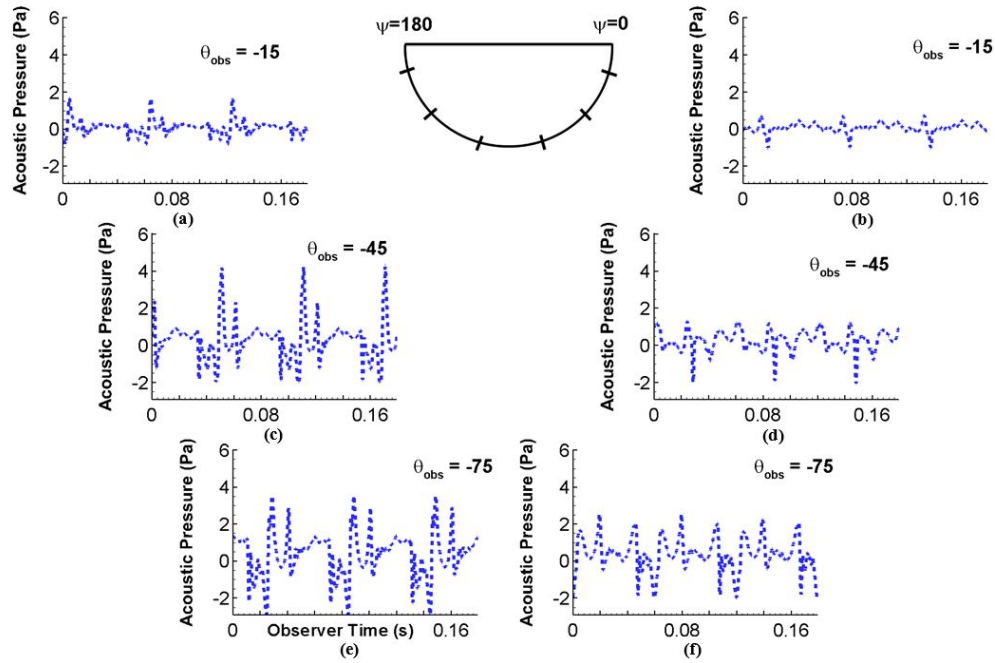


Figure 4.11. Coaxial loading acoustic pressure at out-of-plane $\psi=0$ and 180 deg. observer locations
◇ Coaxial [30].

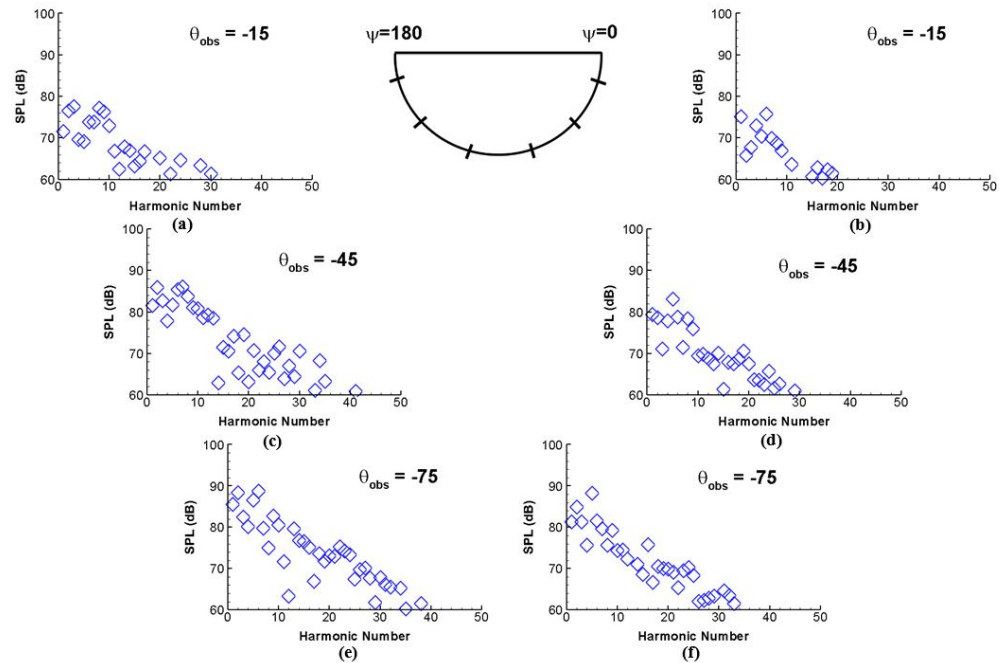


Figure 4.12. Coaxial loading acoustic spectra at out-of-plane $\psi=0$ and 180 deg. observer locations
◇ Coaxial [30].

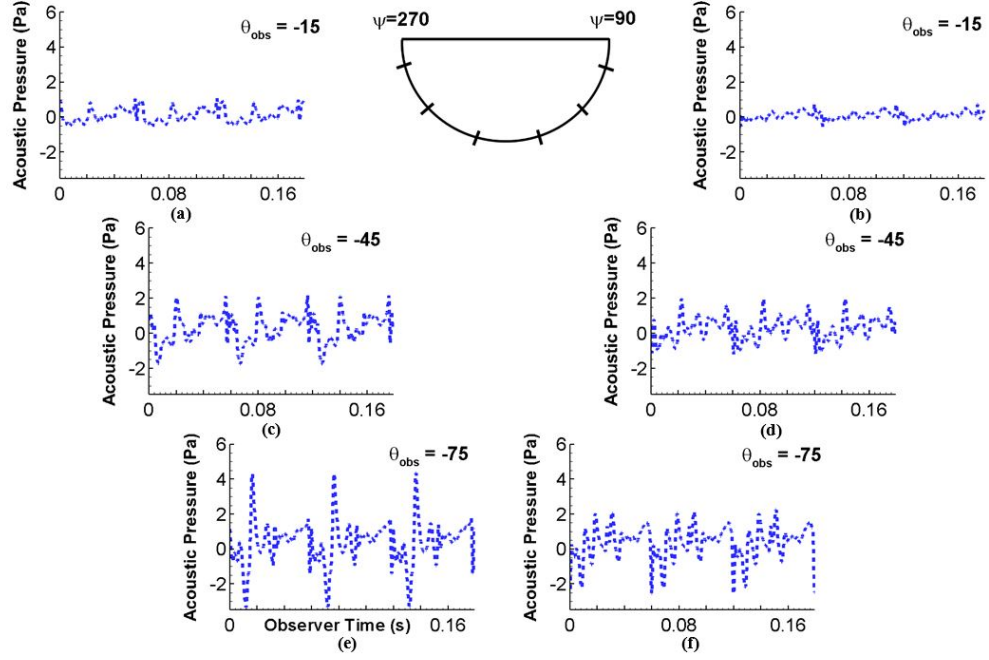


Figure 4.13. Coaxial loading acoustic pressure at out-of-plane $\psi=90$ and 270 deg. observer locations $\cdots \diamond$ Coaxial [30].

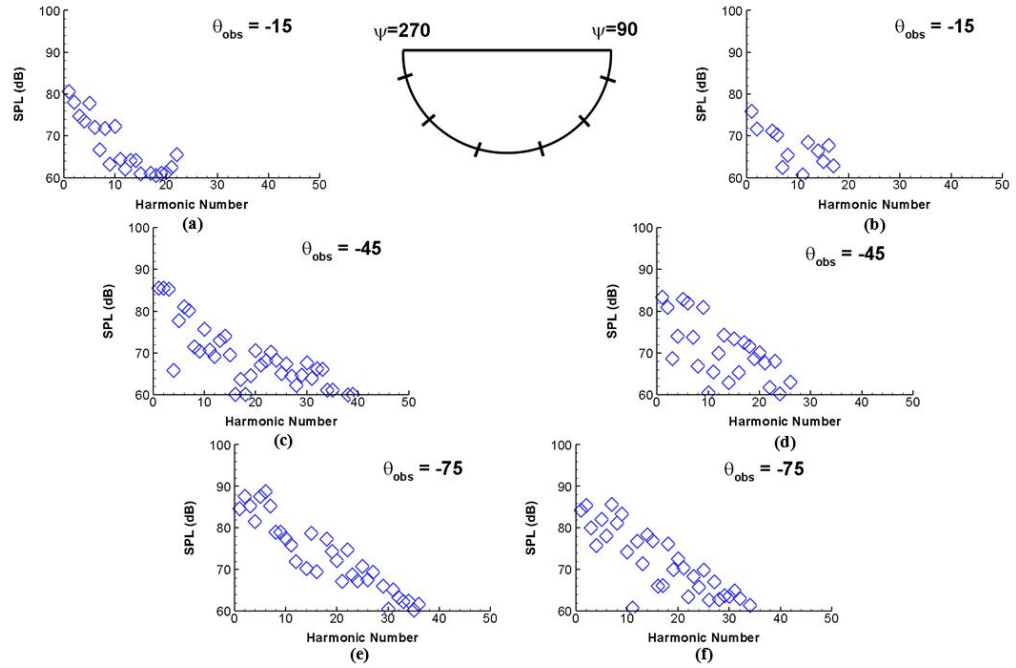


Figure 4.14. Coaxial loading acoustic spectra at out-of-plane $\psi=90$ and 270 deg. observer locations $\cdots \diamond$ Coaxial [30].

At out-of-plane observer locations though, shown in Figs. 4.11 - 4.14, the loading noise and its impulsive nature is important, as the out-of-plane loading noise signals are stronger than the out-of-plane thickness noise signals at most obverse locations. Moreover, impulsive BVI noise-like pulses are evident in Figs. 4.11 and 4.13, especially for observer locations farther from the rotor tip-path plane (i.e., plots (e) and (f)). Excitations such as these are not always present, nor as strong, especially in level, forward flight, with a single main rotor aircraft but the addition of a second rotor appears to cause interactional loading not experienced by a single rotor. At higher forward flight speeds, these loading noise pulses below the rotor plane could become larger and thus, more annoying to observers.

4.3.3 Thickness Noise: Coaxial vs. Conventional

As a further examination of compound lift-offset coaxial helicopter noise characteristics, in-plane thickness noise results for the XH-59 are compared to results of a equivalent solidity, notional, single main rotor in the same flight condition as previously described. This notional single main rotor model was created from the XH-59 coaxial model by taking the three blades on the lower rotor and adding them to the upper rotor, generating a 6-bladed single main rotor, rotating CCW. Although this single main rotor helicopter configuration is not optimally designed, it provides a useful acoustic comparison to reveal important differences between single main rotor and coaxial rotor noise.

Figures 4.15 and 4.16 present the in-plane thickness noise component in the same format as Figs. 4.2 and 4.3 but with the additional single rotor results for comparison. As illustrated in Figs. 4.15 and 4.16, thickness noise for the coaxial configuration is larger, or at least similar to, the conventional single main rotor configuration at all in-plane observers. At observer location (b), the difference in signals and the constructive interference of the coaxial thickness noise is strikingly clear; acoustic pressure pulses are double in strength and half in number of the single rotor configuration. Moreover, additional details can be seen in the acoustic spectra comparison; the coaxial configuration has twice the number of harmonics over the same frequency range as compared to the single rotor configuration in 4.16 (b), because the single rotor's blade passage frequency (BPF) is double that of the coaxial rotor.

These unique characteristics of the coaxial configuration may lead the reader to believe that at an equivalent flight condition, thickness noise of a conventional helicopter configuration may be quieter in the rotor plane than a compound lift-offset coaxial configuration, especially at $\psi = 180$ deg. However, it should be noted that a compound coaxial configuration, like the XH-59, possesses the ability decrease the rotor RPM, while maintaining forward flight speed, by use of auxiliary thrust, potentially decreasing the total noise signal drastically as compared to a single main rotor configuration operating at the same high-speed forward flight condition.

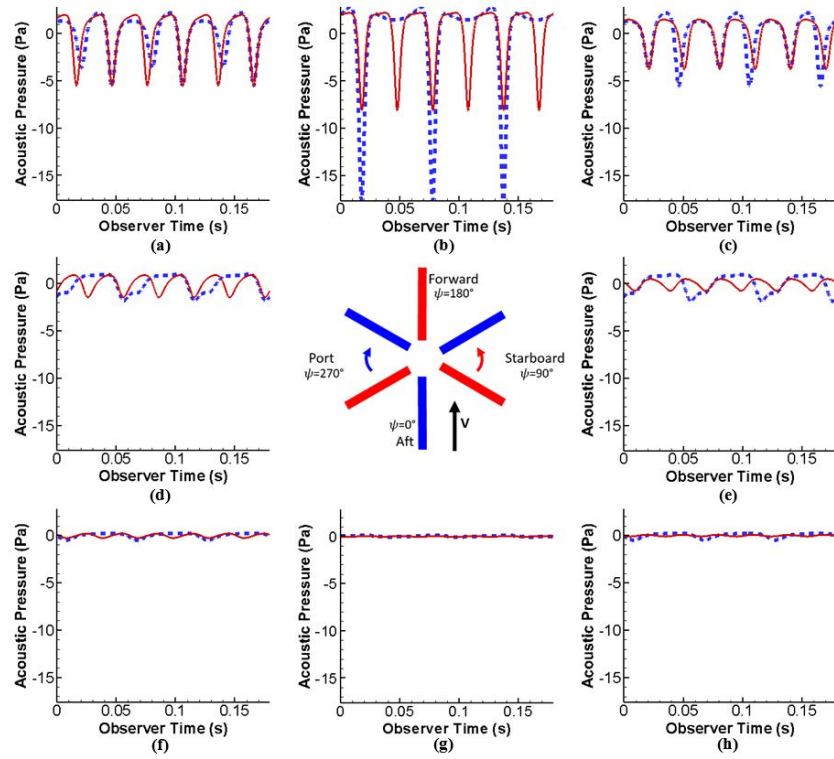


Figure 4.15. Coaxial vs. single rotor thickness acoustic pressure at in-plane observer locations
— \square Single. - - - \diamond Coaxial [30].

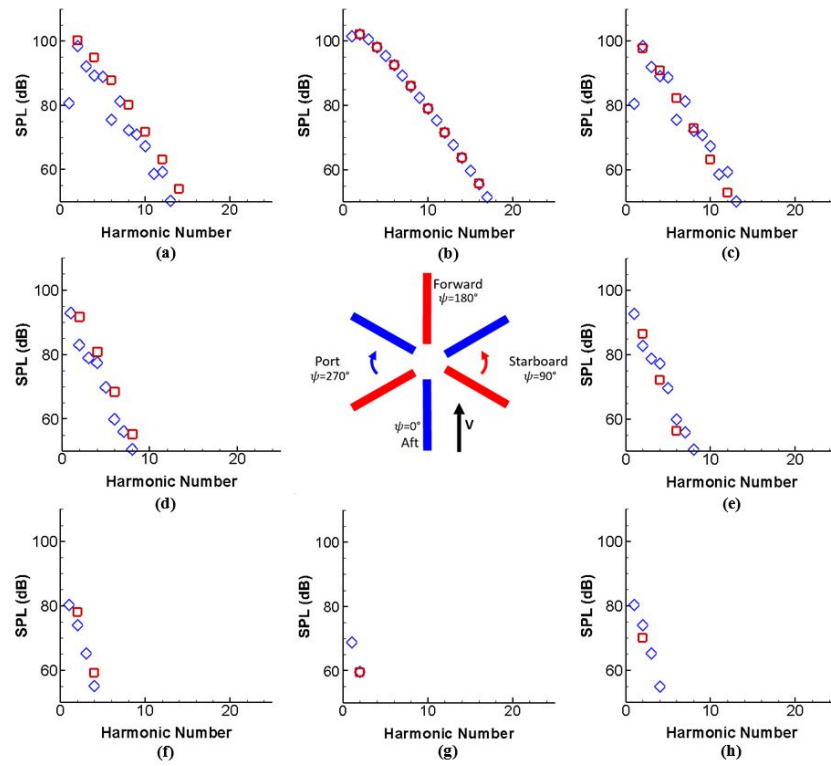


Figure 4.16. Coaxial vs. single rotor thickness acoustic spectra at in-plane observer locations
— \square Single. - - - \diamond Coaxial [30].

4.4 Blade Crossover Comparison

A few unique properties and characteristics of coaxial rotor noise have been presented and pose some concerns of high noise levels for certain observer locations, namely thickness noise in the rotor plane at $\psi = 180$ deg. and loading/BVI noise below the rotor plane. An interesting area to explore next, with this knowledge, is the impact different compound lift-offset coaxial helicopter design variables and/or trim settings (available due to control redundancies) can have on the noise, specifically focused on noise reduction.

The first design parameter considered was the relative blade phasing or blade clocking, effectively altering the azimuth angles at which the upper rotor blades overlap the lower rotor blades. Theoretically, changing this variable will alter the locations of constructive and destructive interferences and shift the impulsive loading locations experienced on the advancing sides of each rotor for potential BVI/loading noise mitigation below the rotor plane.

As a baseline case, the originally assumed blade crossover locations of $\psi = 0$ deg. and every 60 deg. after that around the azimuth (i.e. $\psi = 60, 120, 180, 240, 300$ deg.) was used. Initial crossover locations of $\psi = 0$ deg. through $\psi = 60$ deg. (baseline case again) in increments of 10 deg. were considered. The best and most interesting results occurred when the blades cross at $\psi = 30$ deg. and every 60 deg. after that around the azimuth (i.e. $\psi = 90, 150, 210, 270, 330$ deg.). A comparison of the noise for this phasing configuration to the baseline case are presented and discussed below. In both cases, the XH-59 RCAS model is trimmed with a forward flight speed of 230 kts., at an RPM of 179, resulting in an $M_{AT} = 0.64$, and with a vehicle angle of attack of 3 deg. For reference, Fig. 4.17 below displays both of the compared crossover configurations with the blade crossover locations represented by the blade dotted lines.

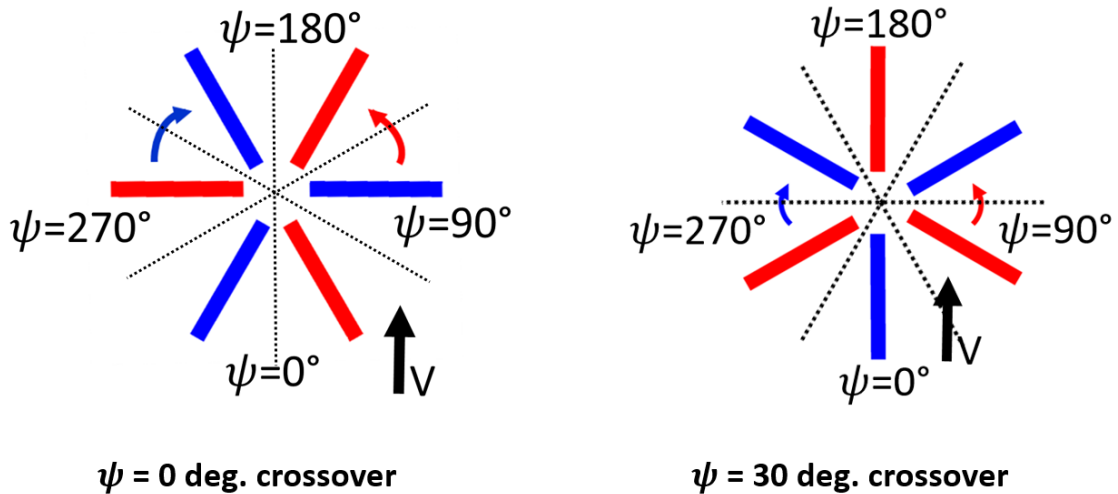


Figure 4.17. Schematic of blade crossover configurations.

4.4.1 Total Noise

As a preliminary result, Figs. 4.18 - 4.23, show the total noise comparison of both blade crossover positions for in-plane and out-of-plane (below plane) observers, respectively. In Figs. 4.18 and 4.19, the total in-plane noise shows no clear indication that either blade crossover configuration provides a substantial acoustic benefit relative to the other, as each signal is stronger at one observer location and then weaker at another; but it is clear that both cases have significant impulsive content.

The total noise at out-of-plane observers, displayed in Figs. 4.20 - 4.23, however, tell a different story. While it is true that both signals continue to be impulsive, changing the initial crossover location to $\psi = 30$ deg., from the original $\psi = 0$ deg. design, is quieter at most observer locations below the rotor plane. Moreover, well below the rotor tip-path plane, in plots (e) and (f) of Figs. 4.21 and 4.23, the sound pressure level (SPL) is higher by 5 to 10 dB at nearly all frequencies with the baseline, $\psi = 0$ deg. crossover case. For a deeper understanding and a better comparison of these acoustic signals, a separate consideration of the thickness and loading components is useful.

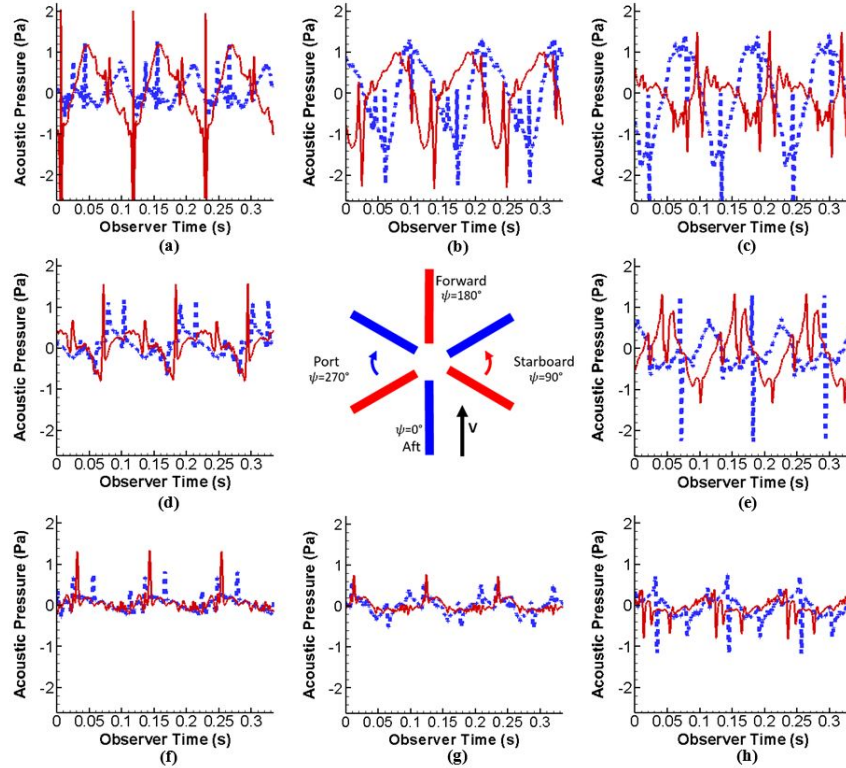


Figure 4.18. Blade crossover comparison of total acoustic pressure at in-plane observer locations
— \square $\psi = 0$ deg. crossover - - - \diamond $\psi = 30$ deg. crossover [30].

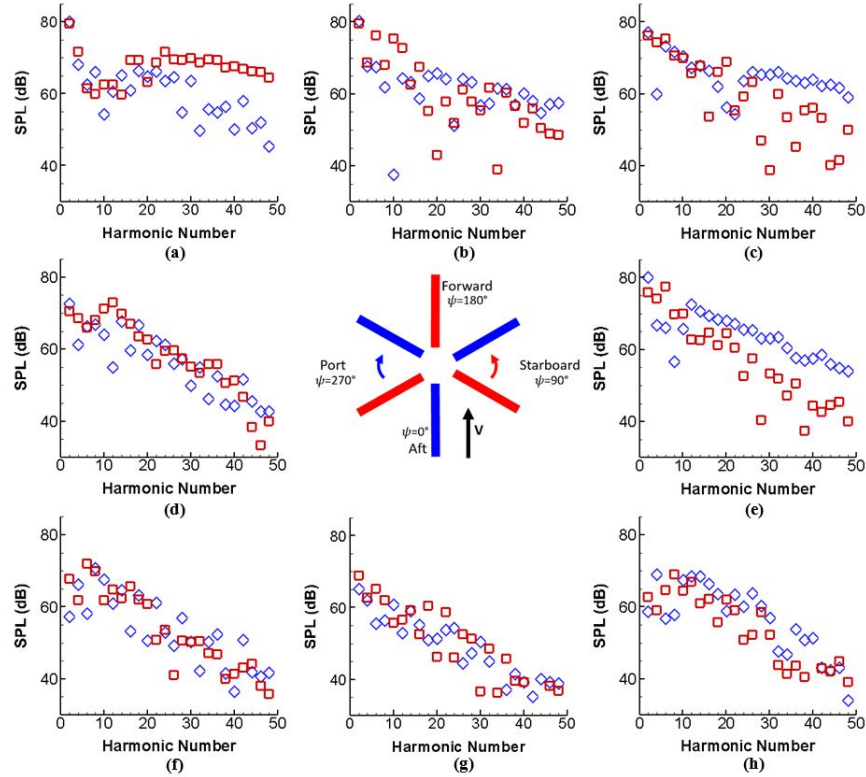


Figure 4.19. Blade crossover comparison of total acoustic spectra at in-plane observer locations — \square $\psi = 0$ deg. crossover — \diamond $\psi = 30$ deg. crossover [30].

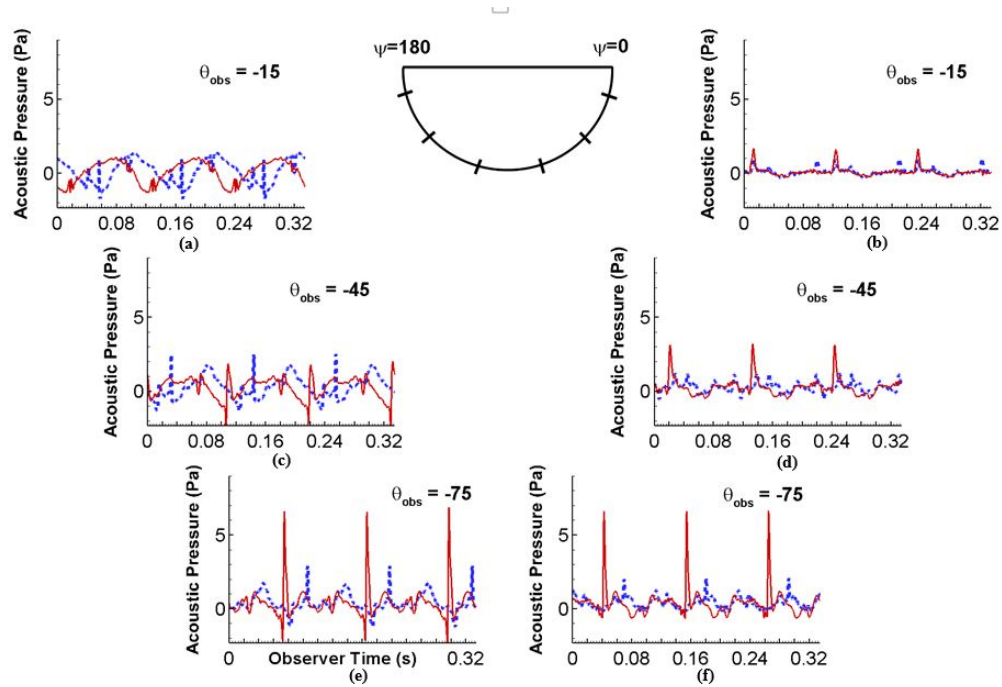


Figure 4.20. Blade crossover comparison of total acoustic pressure at out-of-plane $\psi = 0$ and 180 deg. observer locations — \square $\psi = 0$ deg. crossover — \diamond $\psi = 30$ deg. crossover [30].

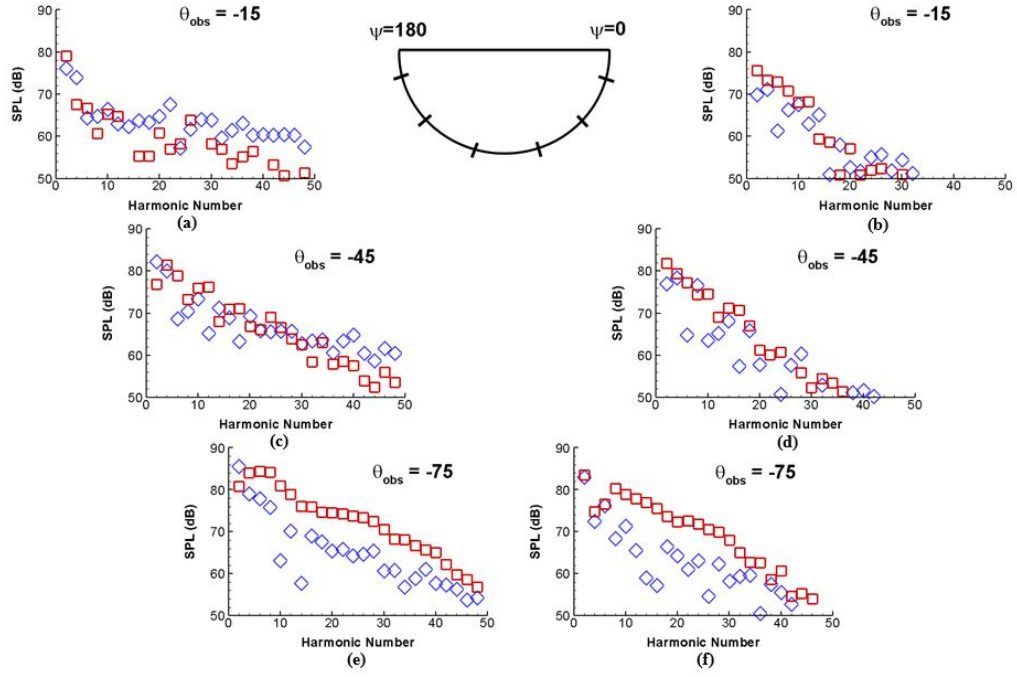


Figure 4.21. Blade crossover comparison of total acoustic spectra at out-of-plane $\psi=0$ and 180 deg. observer locations — \square $\psi = 0$ deg. crossover — \diamond $\psi = 30$ deg. crossover [30].

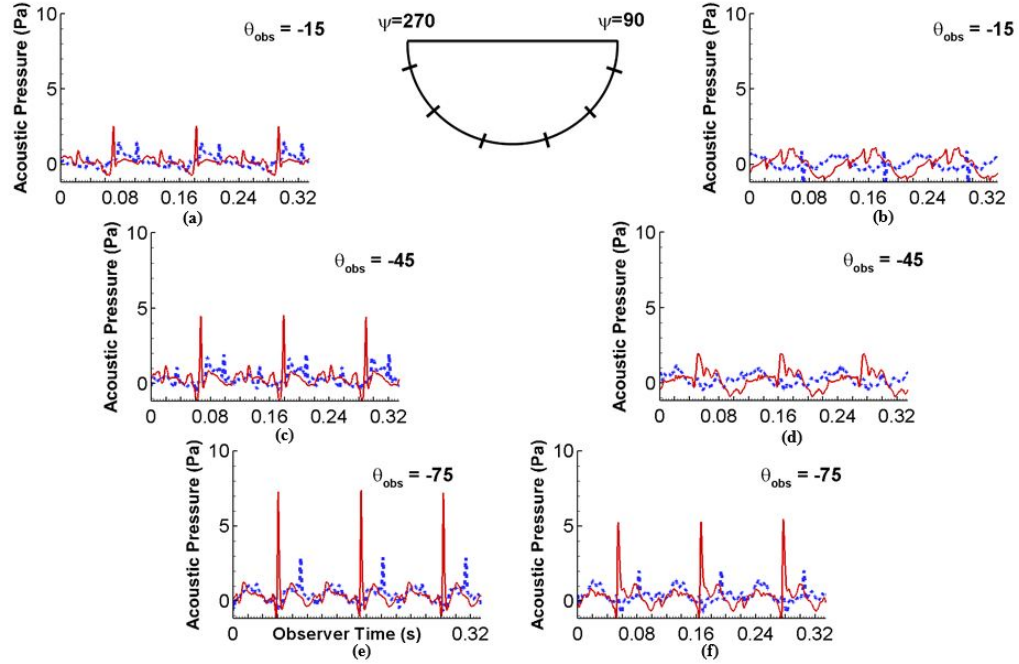


Figure 4.22. Blade crossover comparison of total acoustic pressure at out-of-plane $\psi=90$ and 270 deg. observer locations — \square $\psi = 0$ deg. crossover — \diamond $\psi = 30$ deg. crossover [30].

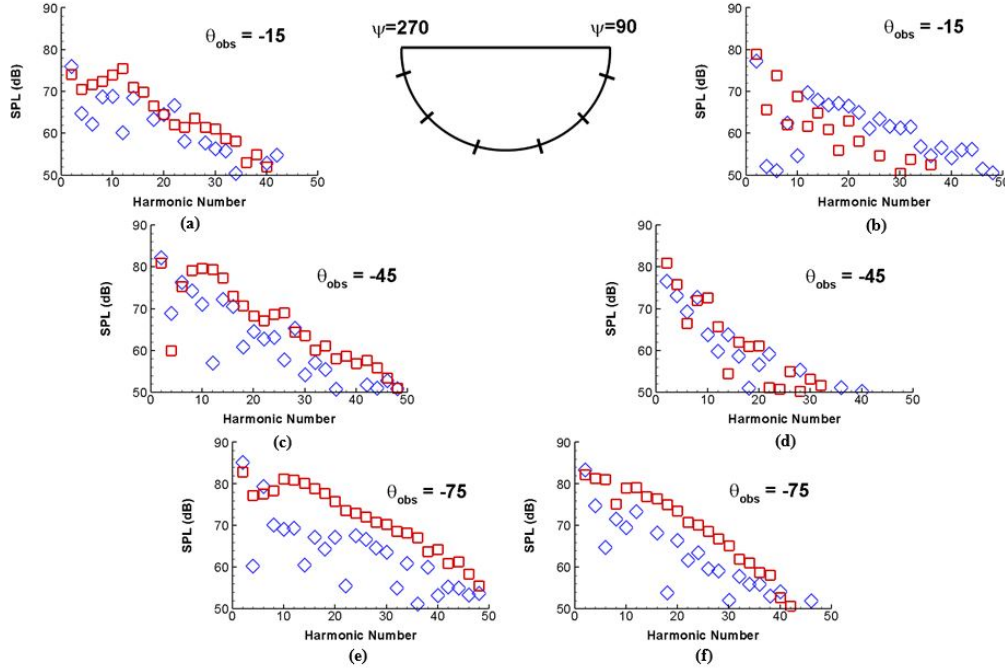


Figure 4.23. Blade crossover comparison of total acoustic spectra at out-of-plane $\psi=90$ and 270 deg. observer locations — \square $\psi = 0$ deg. crossover — \diamond $\psi = 30$ deg. crossover [30].

4.4.2 Thickness Noise

Figures 4.24 - 4.29 display thickness noise only plots for in-plane and out-of-plane observers, respectively. As illustrated by the in-plane plots in Fig. 4.24, there is a clear acoustic benefit at the forward in-plane observer location to changing the blade phasing from the baseline case. These large thickness acoustic signals at $\psi = 180$ deg. no longer have complete constructive interference with one another when the initial blade crossover position is changed to $\psi = 30$ deg. and this observer is no longer the dominant observer location of in-plane noise. Instead, the constructive inference and largest in-plane thickness acoustic pulses are shifted to new observer locations. Although at the $\psi = 135$ and 225 deg. observer locations for the $\psi = 30$ deg. crossover configuration there appears to only be three pulses, they are not equal pulses added together, but rather three sets of two pulses that are very near each other and when combined appear as three pulses. At $\psi = 165$ and 195 deg. the two set of pulses do indeed add to result in a doubling or complete constructive interference.

Moreover, it is important to point out that the in-plane thickness spectra plots, shown in Fig. 4.25 are significantly affected by this blade crossover change. When the signals from the two rotors are essentially identical, such as in Fig. 4.25 (b), with the $\psi = 0$ deg. blade crossover, only half the number of harmonics are observed.

This case is representative of how in-plane thickness noise for a compound lift-offset coaxial rotor can potentially be optimized for desired noise abatement at target observer locations by utilizing the blade phasing variable. Additionally, for a case with a higher RPM and thus, higher

M_{AT} , this blade crossover change will be even more acoustically advantageous as the forward, $\psi = 180$ deg. observer signal strength substantially increases with M_{AT} and becomes even more dominant as compared to other in-plane observer locations.

The out-of-plane comparison of thickness noise for these two blade crossover cases, shown in Figs. 4.26 - 4.29, is less interesting than the in-plane results. Only at the $\psi = 180$ deg. observer location is the change in blade crossover position noticeably beneficial, which was previously established by looking at the in-plane thickness noise. This is not surprising, however, since thickness noise is normally dominant in-plane and loading dominant out-of-plane.

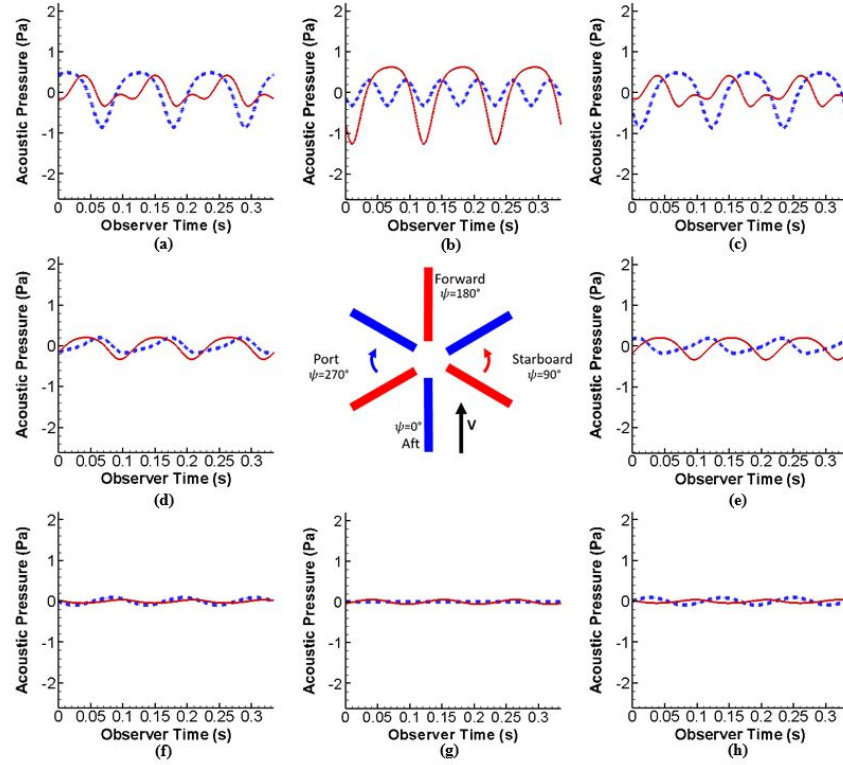


Figure 4.24. Blade crossover comparison of thickness acoustic pressure at in-plane observer locations
— \square $\psi = 0$ deg. crossover - - - \diamond $\psi = 30$ deg. crossover [30].

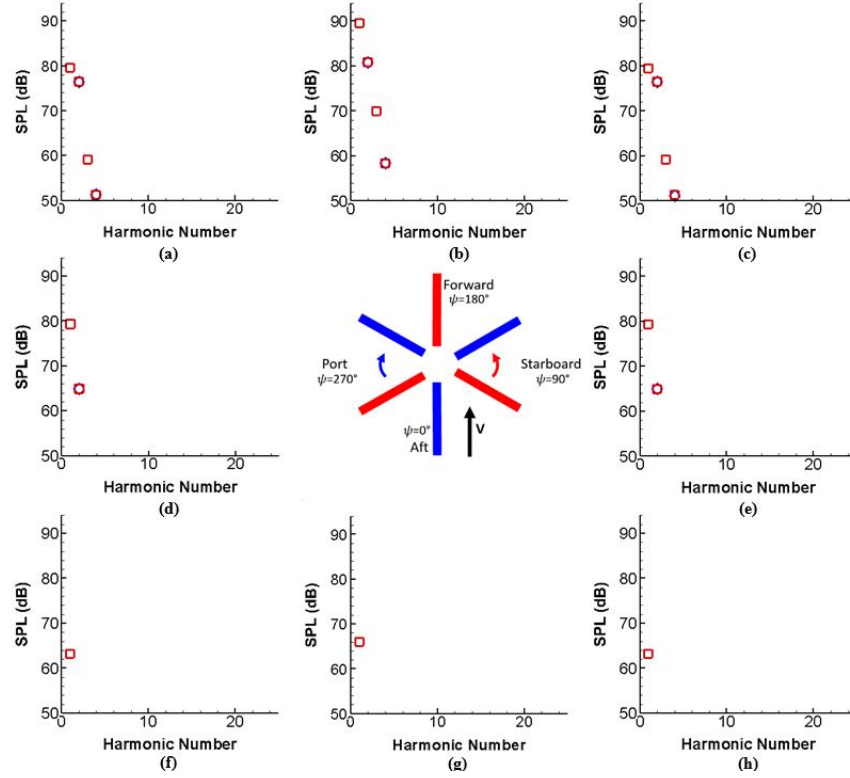


Figure 4.25. Blade crossover comparison of thickness acoustic spectra at in-plane observer locations

—□ $\psi = 0$ deg. crossover —◇ $\psi = 30$ deg. crossover [30].

Note: Values are lower than 50 dB at observer locations (f), (g), and (h) for $\psi = 30$ deg. crossover.

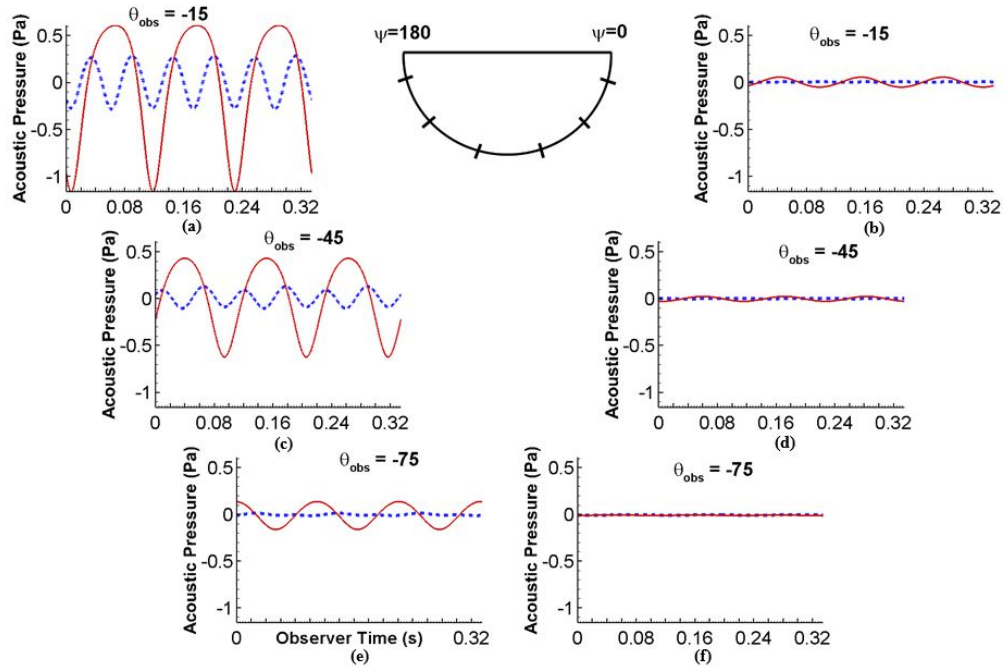


Figure 4.26. Blade crossover comparison of thickness acoustic pressure at out-of-plane $\psi=0$ and 180

deg. observer locations —□ $\psi = 0$ deg. crossover —◇ $\psi = 30$ deg. crossover [30].

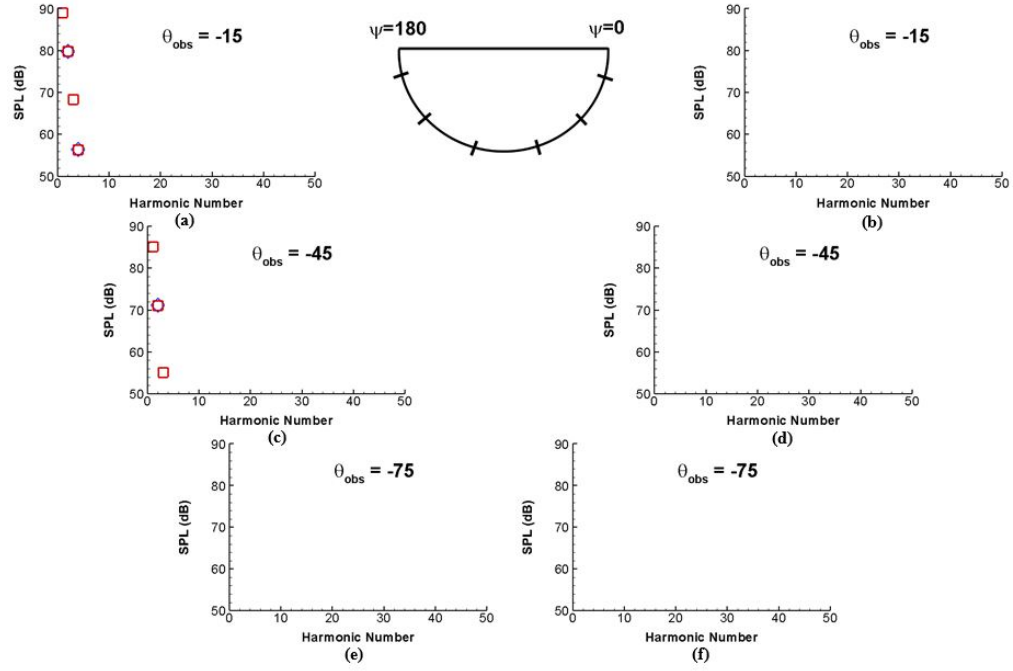


Figure 4.27. Blade crossover comparison of thickness acoustic spectra at out-of-plane $\psi=0$ and 180 deg. observer locations — \square $\psi = 0$ deg. crossover — \diamond $\psi = 30$ deg. crossover [30]. Note: Values are lower than 50 dB at observer locations (b), (d), (f) and (g) for $\psi = 30$ deg. crossover.

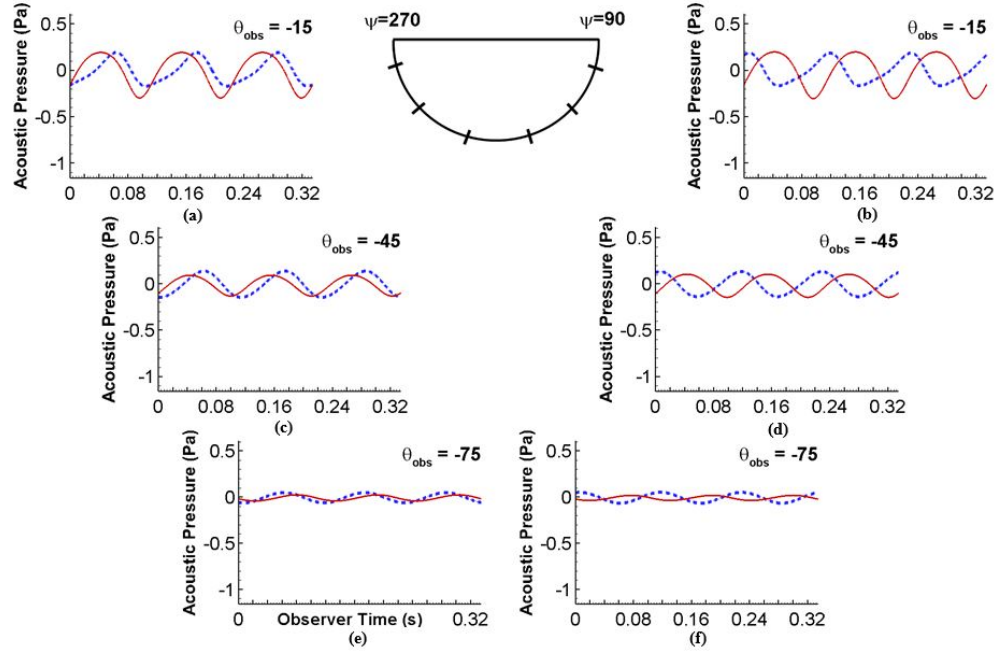


Figure 4.28. Blade crossover comparison of thickness acoustic pressure at out-of-plane $\psi=90$ and 270 deg. observer locations — \square $\psi = 0$ deg. crossover — \diamond $\psi = 30$ deg. crossover [30].

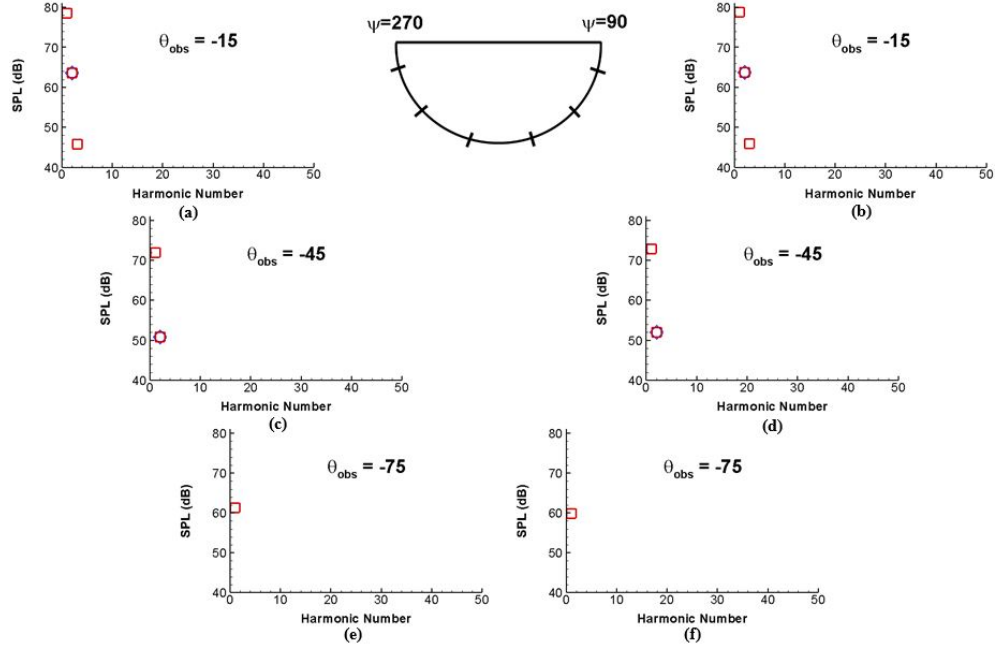


Figure 4.29. Blade crossover comparison of thickness acoustic spectra at out-of-plane $\psi=90$ and 270 deg. observer locations — \square $\psi = 0$ deg. crossover — \diamond $\psi = 30$ deg. crossover [30].

Note: Values are lower than 40 dB at observer locations (e) and (f) for $\psi = 30$ deg. crossover.

4.4.3 Loading Noise

In the same manner as thickness noise, the loading noise was compared for the two different blade crossover cases with in-plane and out-of-plane results shown in Figs. 4.30 - 4.35 respectively. Comparing the in-plane loading noise to the in-plane thickness noise revealed that the loading is the larger noise component in the rotor plane – which is not normally the case. Therefore, the conclusions are the same as for in-plane total noise: the in-plane loading noise shows no uniform acoustic benefit due to altering the blade crossover location but instead, can enable minor noise directivity control.

Contrary to the in-plane results, the out-of-plane loading noise comparison of blade crossover locations provides some very interesting outcomes. In both out-of-plane pressure plots, Figs. 4.32 and 4.34, the overall strength of the loading acoustic pulses is reduced at nearly all observer locations by changing the blade crossover positions from the baseline to the $\psi = 30$ deg. crossover configuration. Most significantly, the strongest loading acoustic pulses in both out-of-plane plots, at observer locations denoted by (e) and (f) in Figs. 4.32 - 4.35, are reduced to a third of the original signal. This is evident in both the time-history and spectral plots.

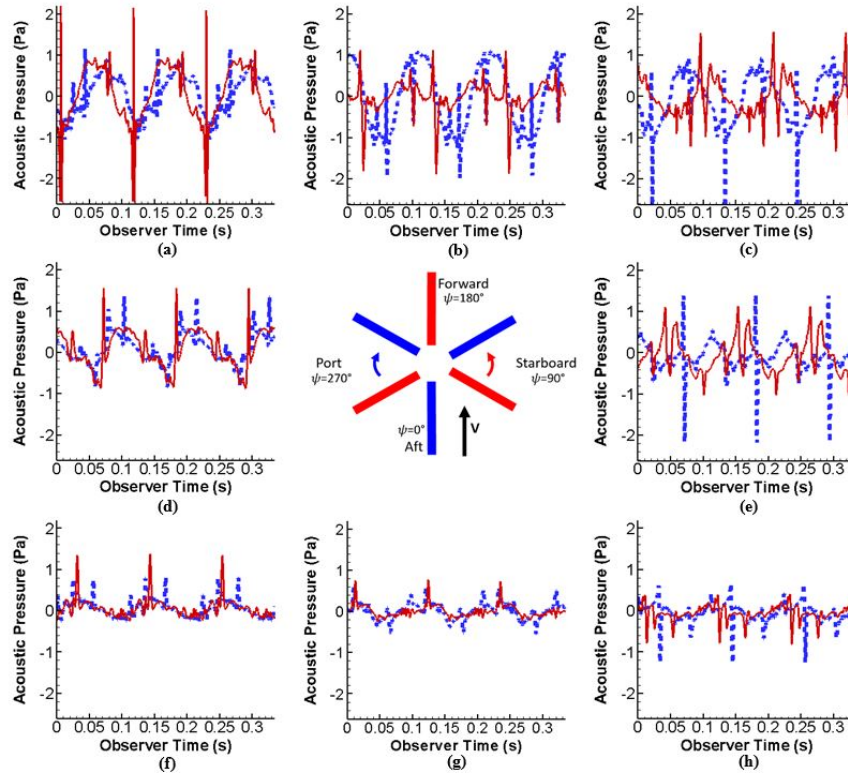


Figure 4.30. Blade crossover comparison of loading acoustic pressure at in-plane observer locations
 — \square $\psi = 0^\circ$ deg. crossover — \diamond $\psi = 30^\circ$ deg. crossover [30].

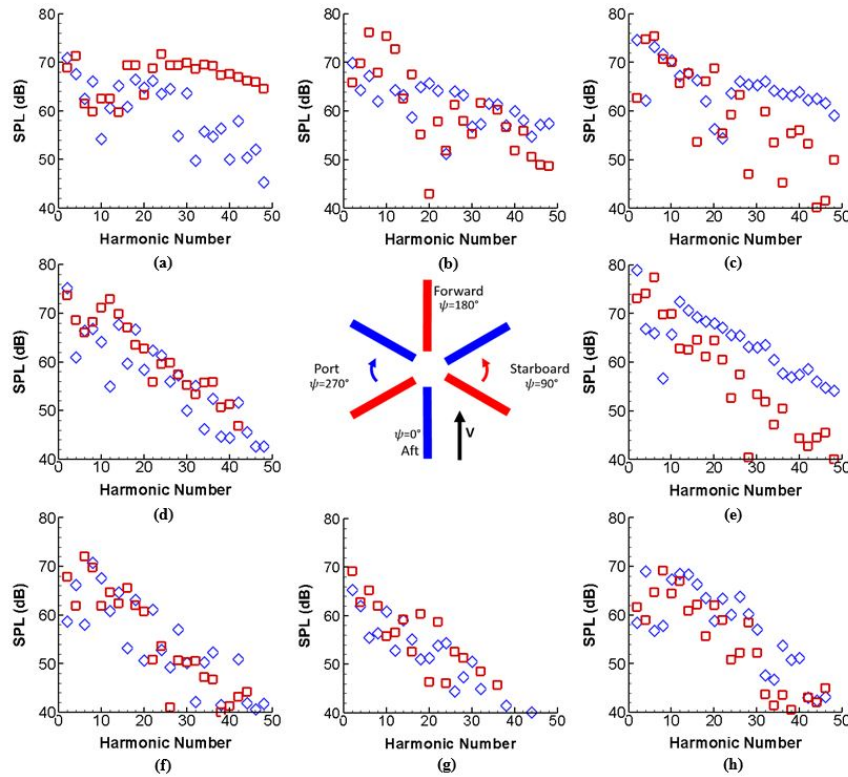


Figure 4.31. Blade crossover comparison of loading acoustic spectra at in-plane observer locations.
 — \square $\psi = 0^\circ$ deg. crossover — \diamond $\psi = 30^\circ$ deg. crossover [30].

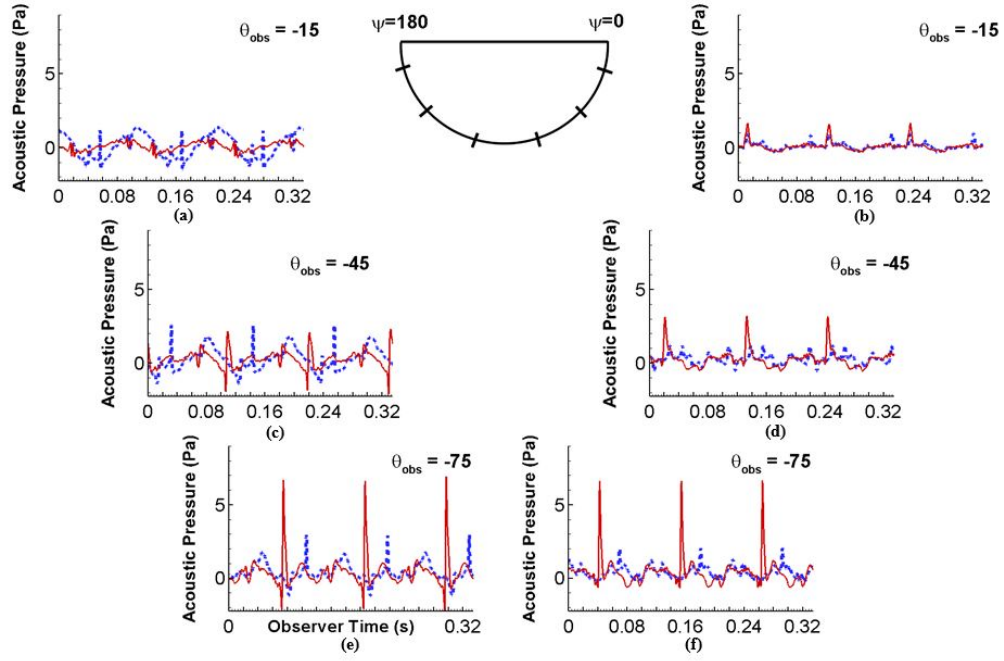


Figure 4.32. Blade crossover comparison of loading acoustic pressure at out-of-plane $\psi=0$ and 180 deg. observer locations — \square $\psi = 0$ deg. crossover — \diamond $\psi = 30$ deg. crossover [30].

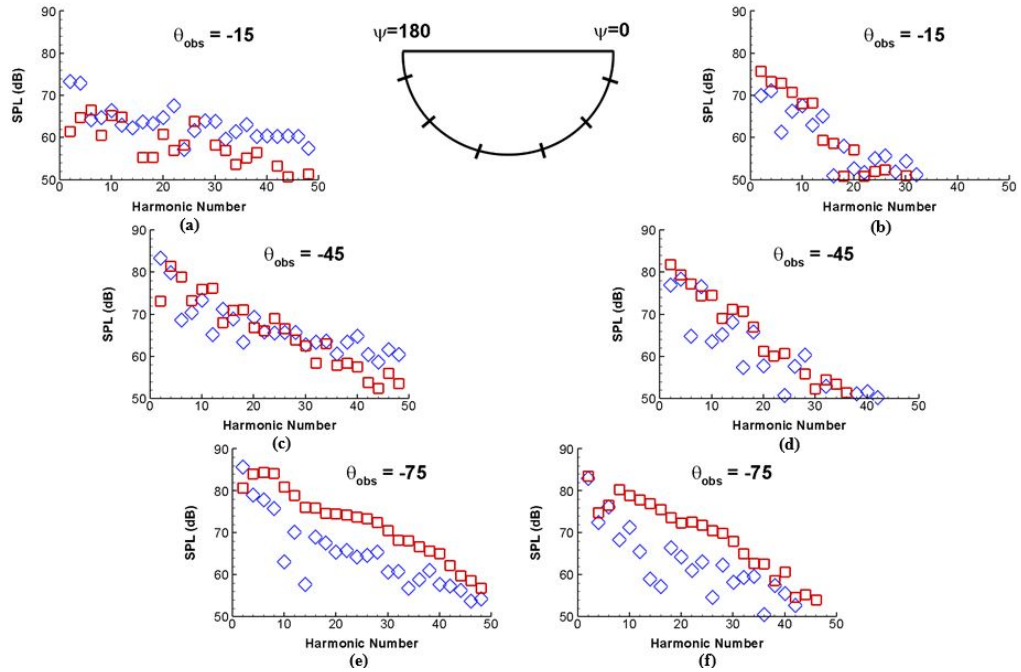


Figure 4.33. Blade crossover comparison of loading acoustic spectra at out-of-plane $\psi=0$ and 180 deg. observer locations — \square $\psi = 0$ deg. crossover — \diamond $\psi = 30$ deg. crossover [30].

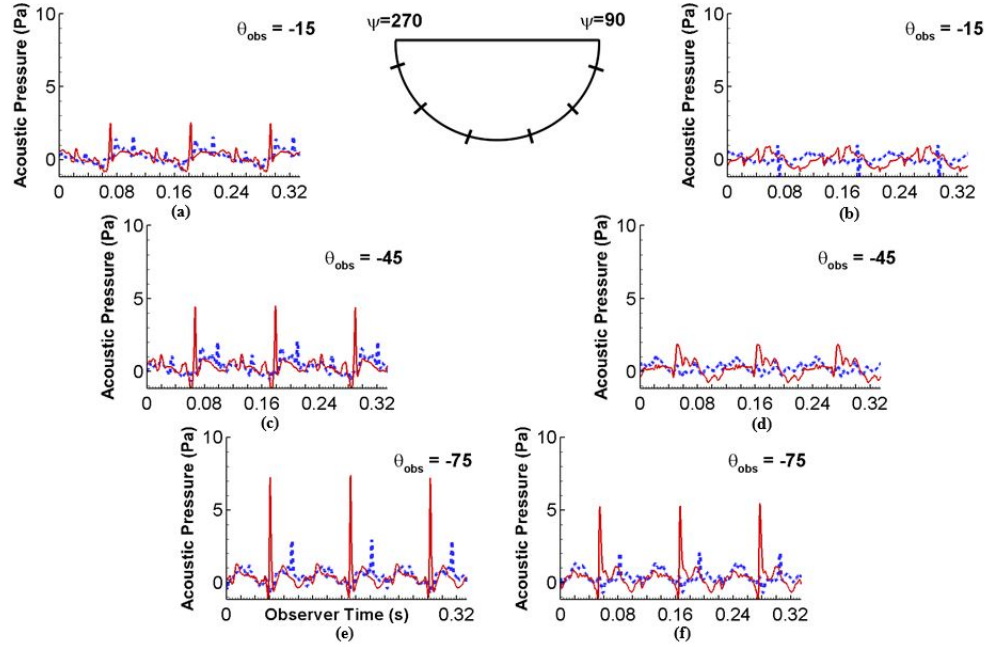


Figure 4.34. Blade crossover comparison of loading acoustic pressure at out-of-plane $\psi=90$ and 270 deg. observer locations — \square $\psi = 0$ deg. crossover — \diamond $\psi = 30$ deg. crossover [30].

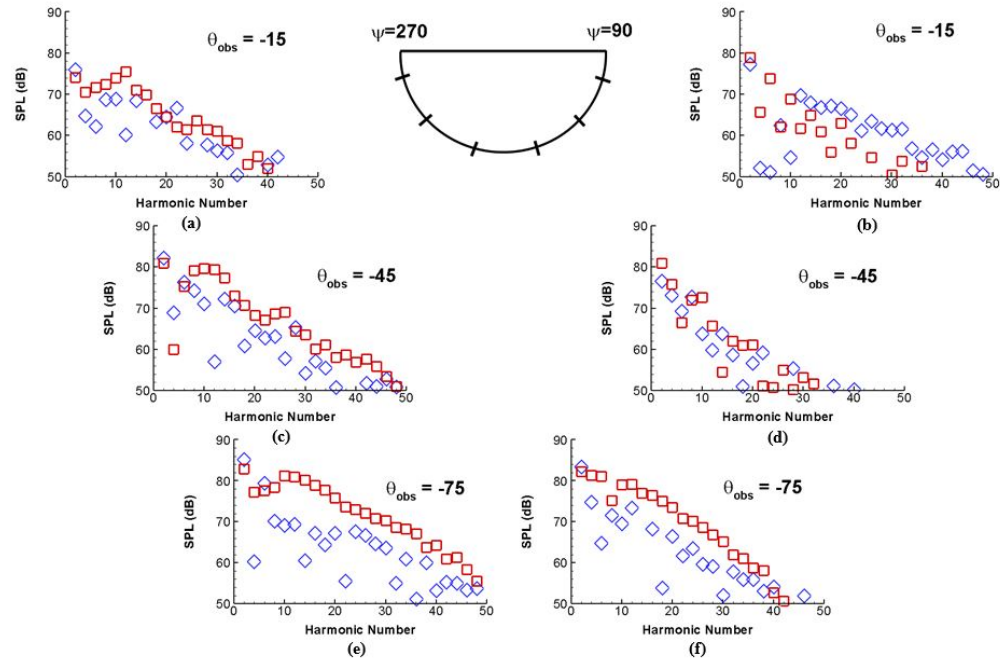


Figure 4.35. Blade crossover comparison of loading acoustic spectra at out-of-plane $\psi=90$ and 270 deg. observer locations — \square $\psi = 0$ deg. crossover — \diamond $\psi = 30$ deg. crossover [30].

By digging deeper and considering the rotor loading for each crossover configuration, shown in Figs. 4.36 and 4.37 for the upper, CCW rotors, and lower, CW rotors, respectively, some insight can be gained as to why the new crossover configuration provides an acoustic benefit. In both Figs. 4.36 and 4.37, the black dash-dot lines represent the locations of blade crossovers for each rotor configuration and $\psi = 180$ deg. is located at the left most point of each circle. As illustrated by Fig. 4.36, comparing both upper, CCW rotors, there is not a noticeable difference between the two contour plots; each appears to have an impulsive loading change around $\psi = 70$ deg. and the baseline configuration does have a second instance around $\psi = 120$ deg., though it doesn't seem to be very significant. The rotor disk loading in Fig. 4.37, of the lower, CW rotors, however, are distinctly different in a few ways. First, the onset of high levels of lift (denoted by deep-orange/red color) at inboard radial stations begins at a different azimuth for each configuration; around $\psi = 290$ deg. for the baseline case and around $\psi = 270$ deg. for the new configuration. It is also interesting to note that in both cases, these regions begin at, or shortly after, a blade crossover with the upper rotor. Lastly, there is an impulsive loading change on the advancing blade of the baseline case, directly at a blade crossover location of $\psi = 240$ deg., where the levels of lift along the blade quickly drop and then spike, which is not present in the new configuration.

These different characteristics, yielded by altering the upper to lower rotor blade phasing, resulted in significant reduction in the strength and impulsiveness of the loading noise, which suggests that the large acoustic pulses shown in Figs. 4.32 and 4.34 could be excited by the specific baseline configuration and mitigated by altering the blade crossover locations. Moreover, while it was originally thought that either blade crossover interactions or self-generated BVI events caused the impulsive loading noise below the rotor plane, the impact of changing the blade crossover positions had on this noise indicates that perhaps it is more likely the blade crossovers or even BVI from the upper rotor into the lower rotor that caused this noise. A further study would be valuable to more completely understand the cause(s) of the impulsive blade loading and resulting noise.

Although the acoustic benefit was not conclusive by only considering the in-plane loading noise, the out-of-plane loading noise results display a strong advantage to modifying the original blade crossover configuration into a new blade phasing, such as the $\psi = 30$ deg. crossover configuration. Likewise, the in-plane thickness noise was also reduced with the change in upper and lower rotor blade phasing, so together, the $\psi = 30$ deg. crossover configuration appears to provide an overall acoustic benefit.

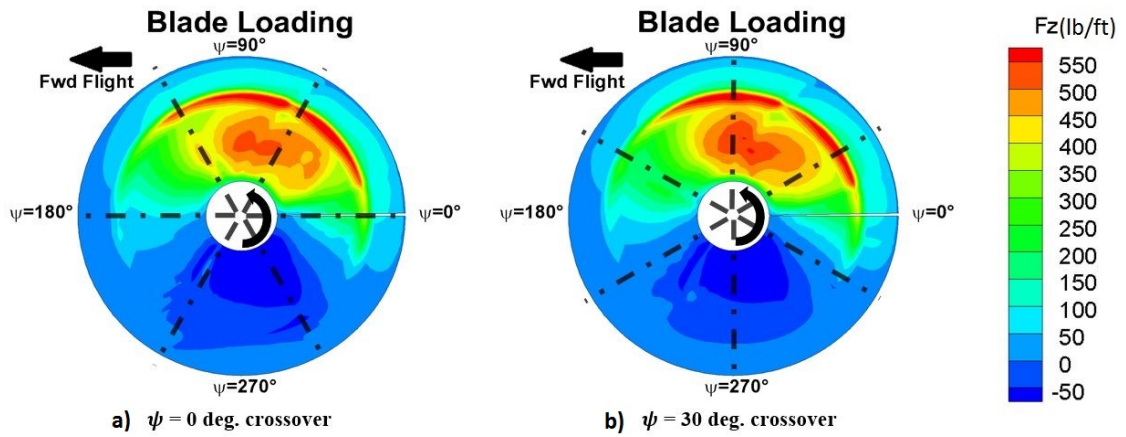


Figure 4.36. Blade crossover comparison of the upper, CCW rotor lift distributions [30].
 a) $\psi = 0^\circ$ deg. crossover (left) and b) $\psi = 30^\circ$ deg. crossover (right).
 Black dash-dot lines represent blade crossover locations.

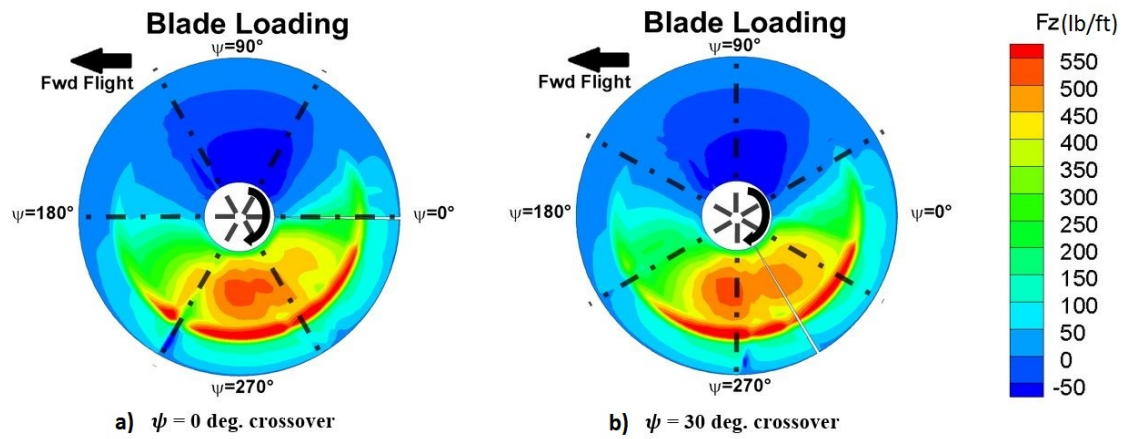


Figure 4.37. Blade crossover comparison of the lower, CW rotor lift distributions [30].
 a) $\psi = 0^\circ$ deg. crossover (left) and b) $\psi = 30^\circ$ deg. crossover (right).
 Black dash-dot lines represent blade crossover locations.

4.5 RPM Reduction Study

The blade crossover locations of the upper and lower rotor proved to be an important acoustic factor, primarily for the out-of-plane loading noise. A second compound lift-offset coaxial helicopter parameter, the rotors' RPM, was also considered acoustically. A thrust compounded helicopter, like the XH-59, possesses the ability to achieve the same forward flight speed at different main rotor RPMs with the use of auxiliary propulsion; thus the rotor RPM is a trim variable (i.e., can be altered while achieving same flight condition).

As previously seen in Farassat's Formulation 1A, the powers of the Doppler amplification in each of the acoustic pressure terms have a strong influence on the noise and, because the Mach number varies linearly with RPM for a fixed flight speed, varying the RPM is expected to have a significant impact on the overall noise.

Though the XH-59 has a maximum design RPM of 345, for the purposes of this study and for realistic forward flight trim of the helicopter, settings for a slowed rotor were compared: RPMs of 179, 207 and 276 (52%, 60% and 80% of maximum RPM respectively). In each case, the helicopter was trimmed with a forward flight speed of 230 kts, resulting in $M_{AT} = 0.64, 0.69,$ and 0.81 for 179, 207 and 276 RPM respectively, and an aircraft angle of attack of 3 deg. for all three cases. Additionally, although the upper to lower rotor blade phasing was shown to be effective in noise reduction, the blade phasing in this comparison was held constant at the baseline $\psi = 0$ deg. crossover configuration.

4.5.1 Total Noise

In the same manner as the blade crossover study, Figs. 4.38 - 4.43 show the total noise first for both in-plane and out-of-plane observer locations, respectively. It should be noted that the x-axis in all the plots in this RPM reduction study are "Fraction of Revolution," ranging from 0 to 1, normalizing the rotor rotation speed for easier comparisons between different RPM cases. Upon review of the total in-plane results in Figs. 4.38 and 4.39, it is immediately clear that reducing the rotor RPM has a powerful impact on reducing the overall in-plane noise and is most effective in plot (b) of Figs. 4.38 and 4.39, where the in-plane noise is dominant.

Likewise, the out-of-plane plots in Figs. 4.40 - 4.43 show a noise reduction with RPM reduction; but, at some out-of-plane observers, the opposite is true: the noise increased with an RPM decrease. This is an area that needs to be further examined by separately considering thickness and loading noise.

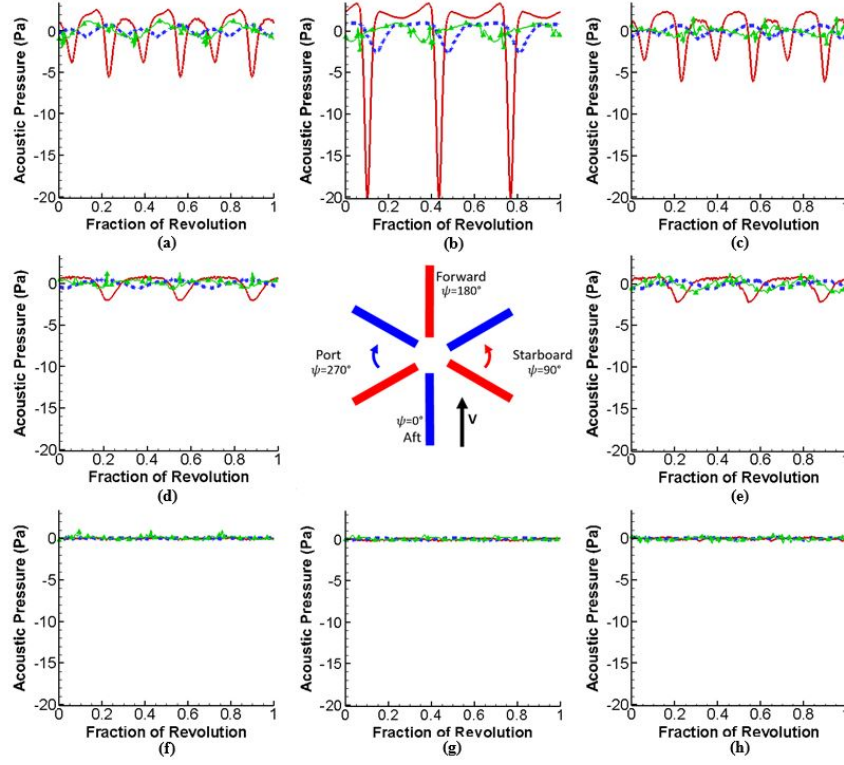


Figure 4.38. RPM comparison of total acoustic pressure at in-plane observer locations
— \square 276 — \diamond 207 — \triangle 179 (M_{AT} : 0.84, 0.72, 0.67) [30].

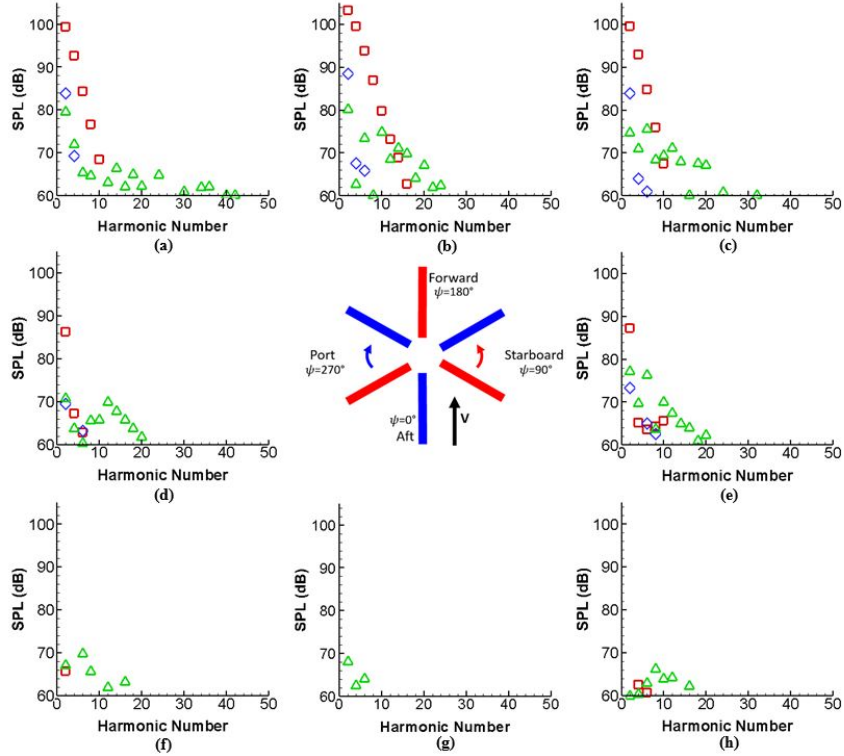


Figure 4.39. RPM comparison of total acoustic spectra at in-plane observer locations
— \square 276 — \diamond 207 — \triangle 179 (M_{AT} : 0.84, 0.72, 0.67) [30].

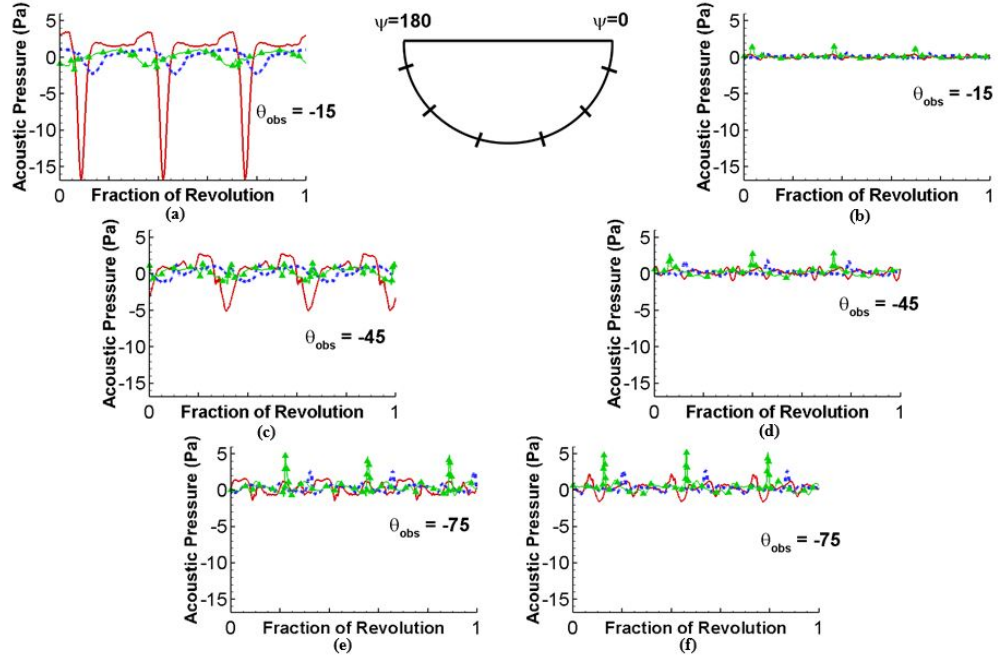


Figure 4.40. RPM comparison of total acoustic pressure at out-of-plane $\psi=0$ and 180 deg. observer locations — 276 — 207 — 179 (M_{AT} : 0.84, 0.72, 0.67)[30].

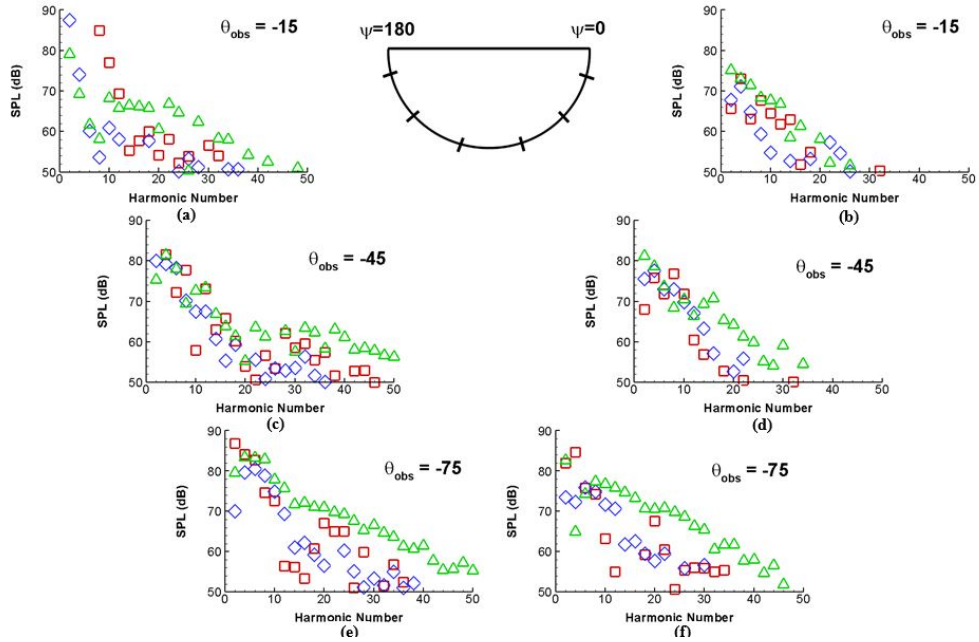


Figure 4.41. RPM comparison of total acoustic spectra at out-of-plane $\psi=0$ and 180 deg. observer locations — 276 — 207 — 179 (M_{AT} : 0.84, 0.72, 0.67)[30].

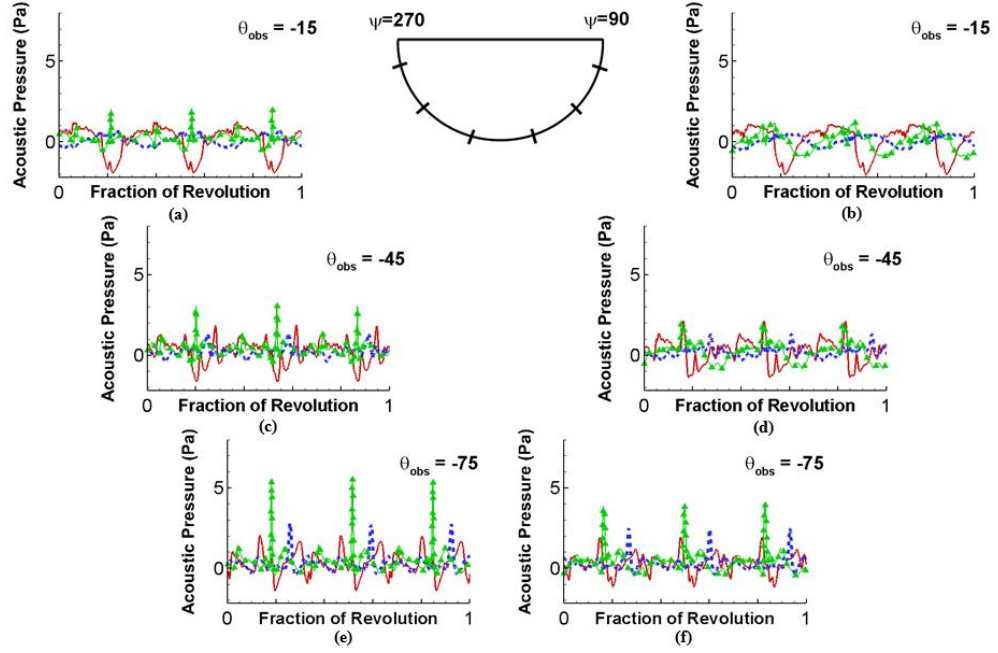


Figure 4.42. RPM comparison of total acoustic pressure at out-of-plane $\psi=90$ and 270 deg. observer locations — \square 276 — \diamond 207 — \triangle 179 (M_{AT} : 0.84, 0.72, 0.67)[30].

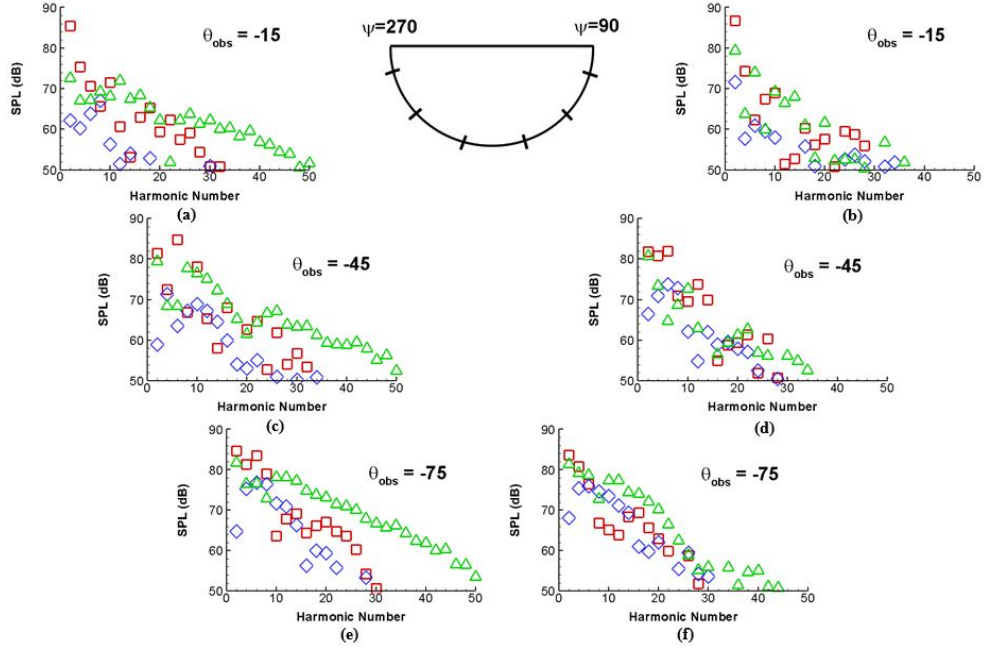


Figure 4.43. RPM comparison of total acoustic spectra at out-of-plane $\psi=90$ and 270 deg. observer locations — \square 276 — \diamond 207 — \triangle 179 (M_{AT} : 0.84, 0.72, 0.67)[30].

4.5.2 Thickness Noise

In Figs. 4.44 - 4.49 below, in-plane and out-of-plane thickness noise comparisons of the three rotor RPM cases are shown. Since thickness noise is largely dominant within the rotor plane and often of less significance out of the rotor plane, only the in-plane plots are discussed but the out-of-plane plots are shown for completeness.

As displayed by the in-plane plot in Figs. 4.44 and 4.45, the reduction in rotor RPM results in a dramatic reduction in thickness noise at all in-plane observers. This decrease is so substantial that the acoustic pulses of the 179 RPM case can hardly be seen when plotted on the same scale as the 276 RPM case, especially in plot (b) of Figs. 4.44 and 4.45. However, the thickness noise reduction is not a huge surprise when considering the Doppler amplification factor in Farassat's Formulation 1A. As mentioned before, the Doppler amplification and the Mach number of the blades have a large influence on the thickness noise and this impact is twofold when considering the presence of constructive interference at some in-plane observers. By making a large reduction in the rotor RPM, the Mach number on the blades is proportionally reduced, despite maintaining the helicopter's forward flight speed, which leads to this large reduction in the thickness noise signal.

For further reference and to understand the magnitude of the impact of this rotor RPM reduction, an additional case was run with the XH-59's design RPM of 345 and the in-plane thickness noise is compared to the 276 and 179 RPM cases and shown in Figs. 4.50 and 4.51. Though high-speed impulsive (HSI) noise is not accounted for and would likely more than double the acoustic pressure pulse for the 345 RPM case, it is still evident that flying with a lower rotor RPM, is perhaps the most effective approach to mitigate the noise. Moreover, the RPM should be the primary parameter considered to reduce the in-plane thickness noise of a compound lift-offset coaxial helicopter because noise dramatically changes and high forward flight speeds can be maintained with variation of the RPM.

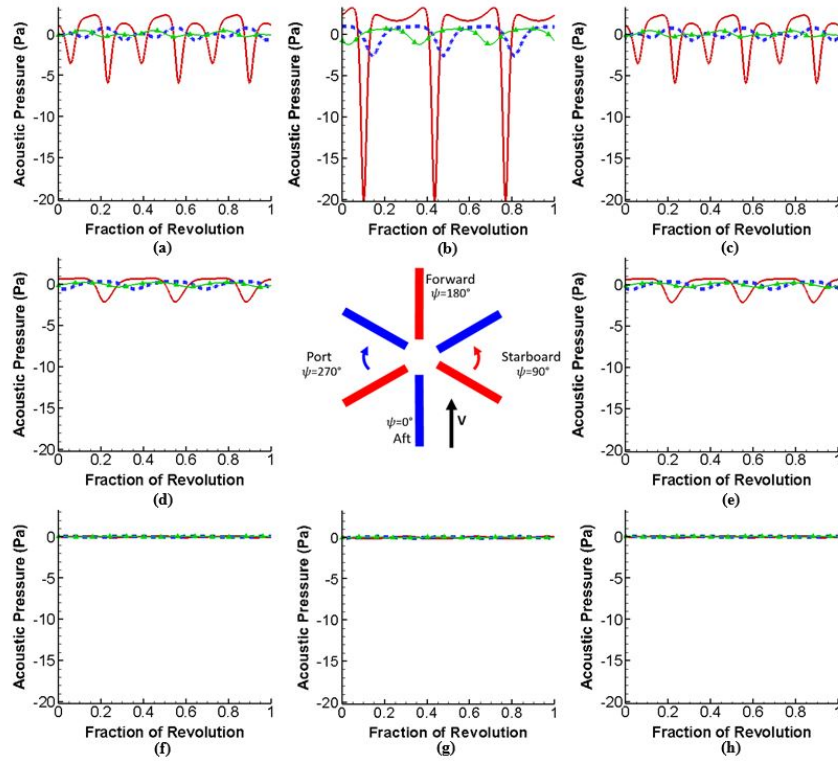


Figure 4.44. RPM comparison of thickness acoustic pressure at in-plane observer locations
— \square 276 — \diamond 207 — \triangle 179 (M_{AT} : 0.84, 0.72, 0.67)[30].

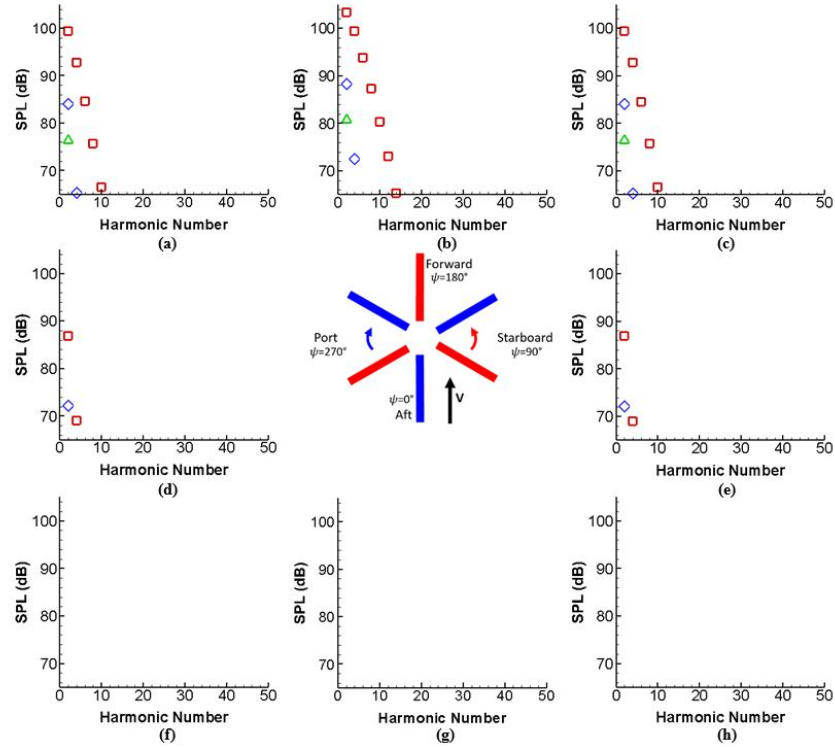


Figure 4.45. RPM comparison of thickness acoustic spectra at in-plane observer locations
— \square 276 — \diamond 207 — \triangle 179 (M_{AT} : 0.84, 0.72, 0.67)[30].

Note: Most values are lower than 70 dB at observer locations (d), (e), (f), (g), and (h).

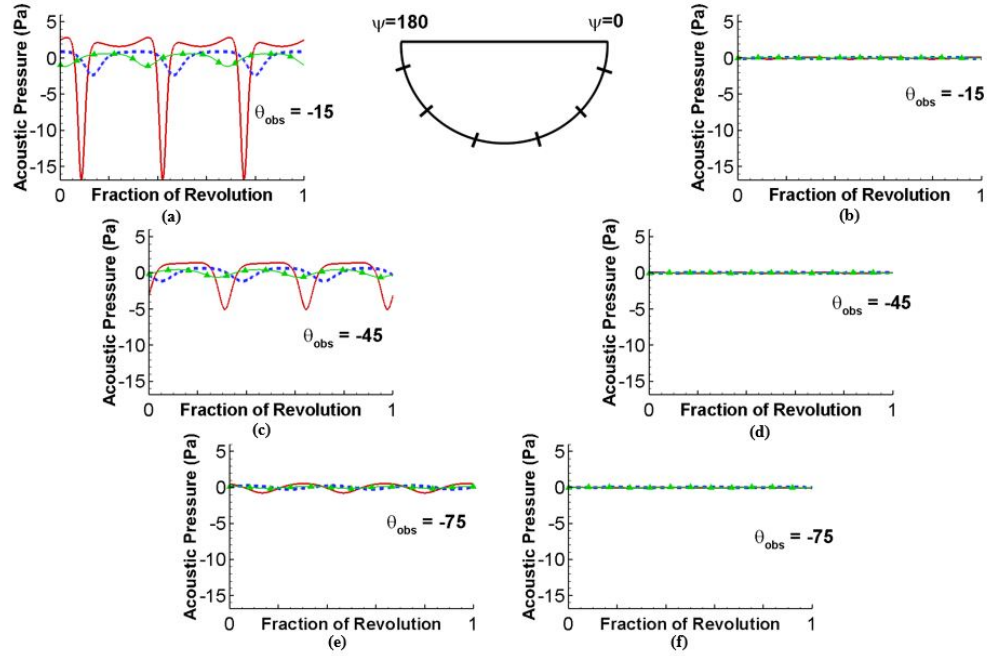


Figure 4.46. RPM comparison of thickness acoustic pressure at out-of-plane $\psi=0$ and 180 deg. observer locations — \square 276 — \diamond 207 — \triangle 179 (M_{AT} : 0.84, 0.72, 0.67).

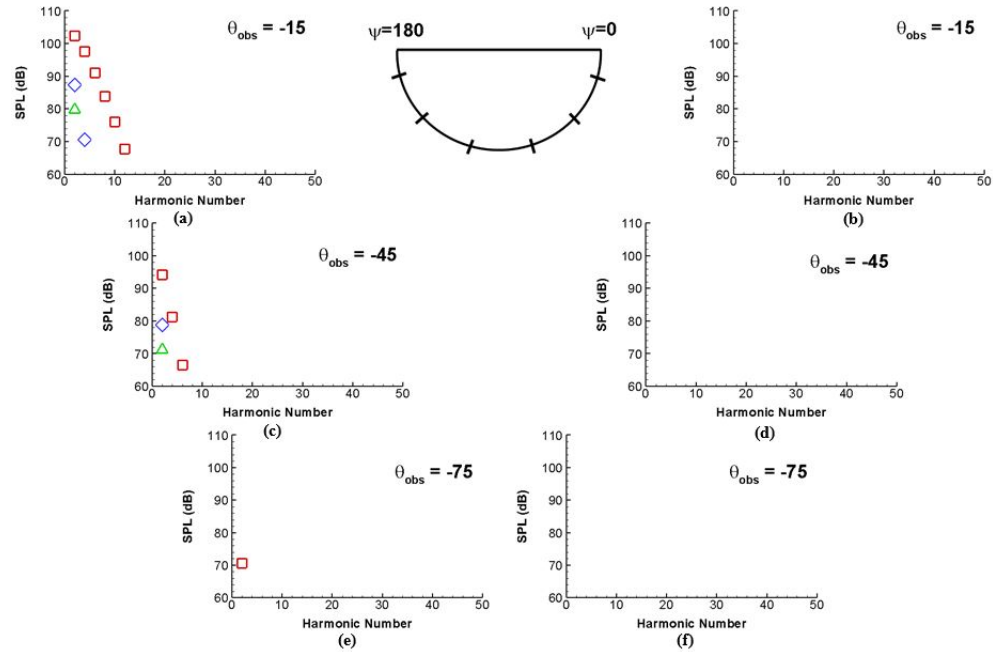


Figure 4.47. RPM comparison of thickness acoustic spectra at out-of-plane $\psi=0$ and 180 deg. observer locations — \square 276 — \diamond 207 — \triangle 179 (M_{AT} : 0.84, 0.72, 0.67).

Note: Most values are lower than 60 dB at observer locations (b), (d), (e) and (f).

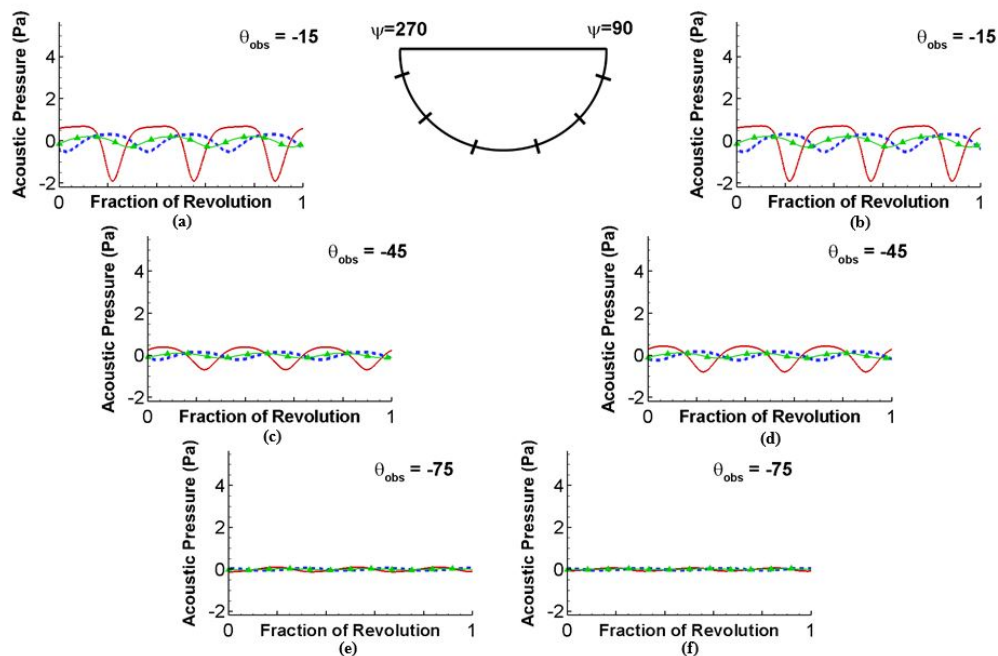


Figure 4.48. RPM comparison of thickness acoustic pressure at out-of-plane $\psi=90$ and 270 deg. observer locations — \square 276 — \diamond 207 — \triangle 179 (M_{AT} : 0.84, 0.72, 0.67).

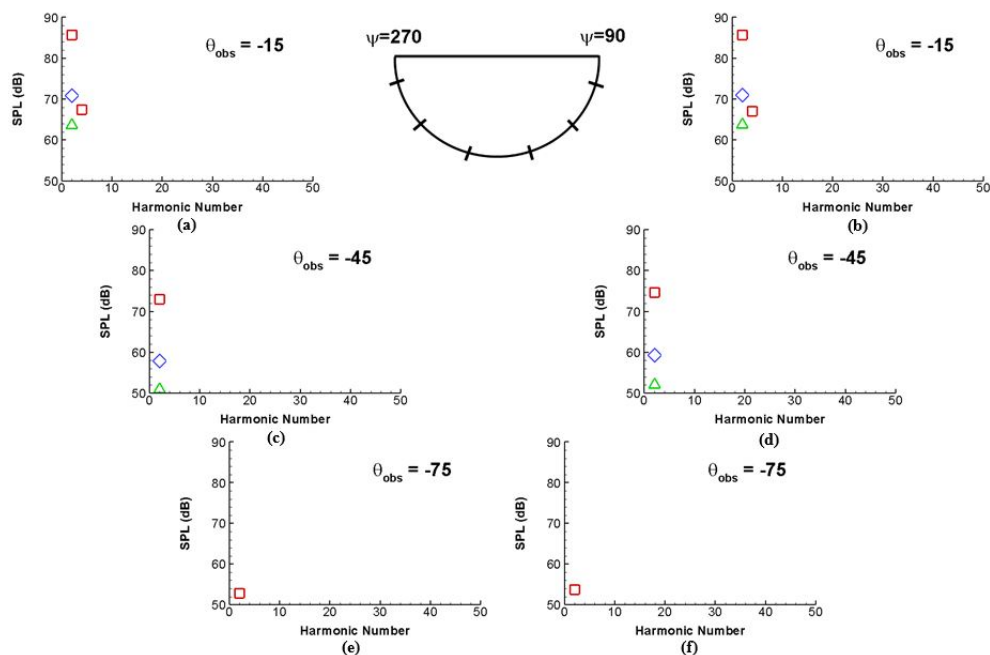


Figure 4.49. RPM comparison of thickness acoustic spectra at out-of-plane $\psi=90$ and 270 deg. observer locations — \square 276 — \diamond 207 — \triangle 179 (M_{AT} : 0.84, 0.72, 0.67).

Note: Most values are lower than 50 dB at all observer locations.

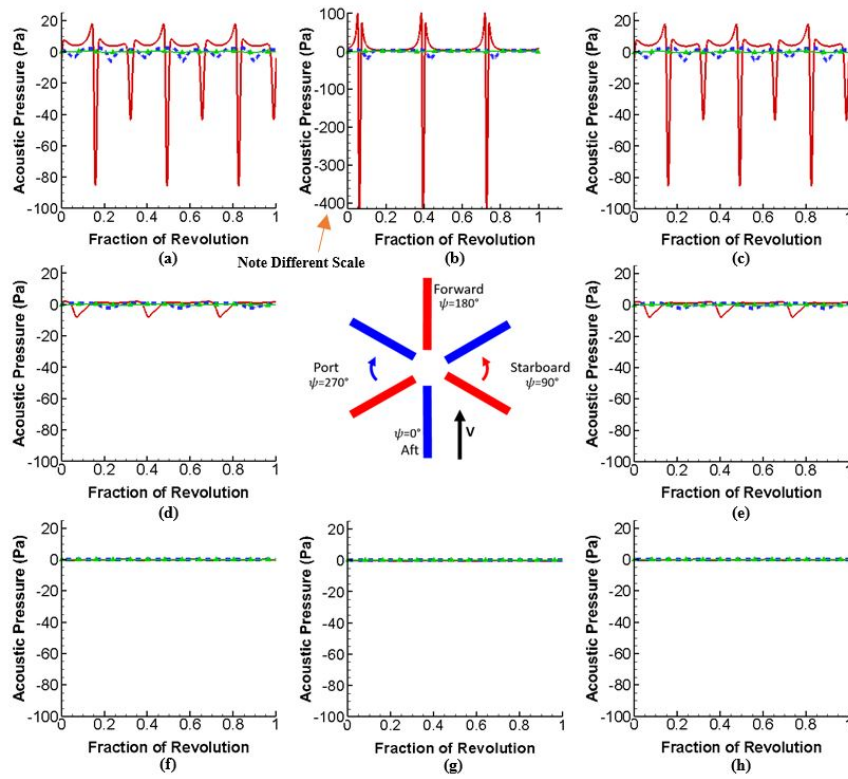


Figure 4.50. RPM comparison of thickness acoustic pressure at in-plane observer locations — \square 345 — \diamond 276 — \triangle 179 (M_{AT} : 0.84, 0.72, 0.67) [30].

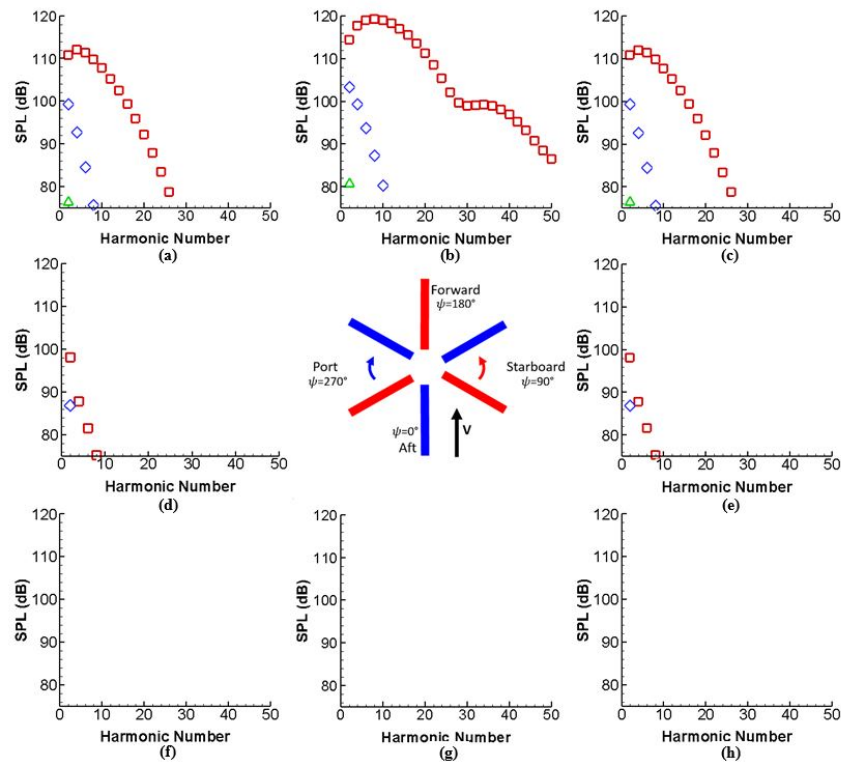


Figure 4.51. RPM comparison of thickness acoustic spectra at in-plane observer locations — \square 345 — \diamond 276 — \triangle 179 (M_{AT} : 0.84, 0.72, 0.67) [30].

Note: Most values are lower than 80 dB at observer locations (d), (e), (f), (g), and (h).

4.5.3 Loading Noise

Since it has been established that thickness noise is greatly reduced with RPM, loading noise is now considered and displayed for both in-plane and out-of-plane observers in Figs. 4.52 -4.57. For the in-plane observers in Figs. 4.52 and 4.53, it is interesting to note that the RPM appears to have the opposite effect on loading noise as it did on thickness noise. The loading noise at in-plane observer locations actually increases with a decrease in RPM. Despite this increase, when the in-plane loading noise is considered on the scale of the in-plane thickness noise, this increase is not very significant.

In Figs. 4.54 - 4.57, a similar phenomenon can be seen for loading noise at out-of-plane observers. The loading noise is similar between the different RPM cases for most out-of-plane observer locations but observers at an elevation angle of -75 deg. experience an increase in the loading noise signal with a decrease in RPM. Specifically, large, narrow acoustic pulses appear as the RPM is decreased to 179. In contrast to the in-plane loading noise increase with RPM reduction, the out-of-plane increase is significant as loading noise is dominant out of the rotor plane, especially at an elevation angle of -75 deg., where these highly impulsive signals appear.

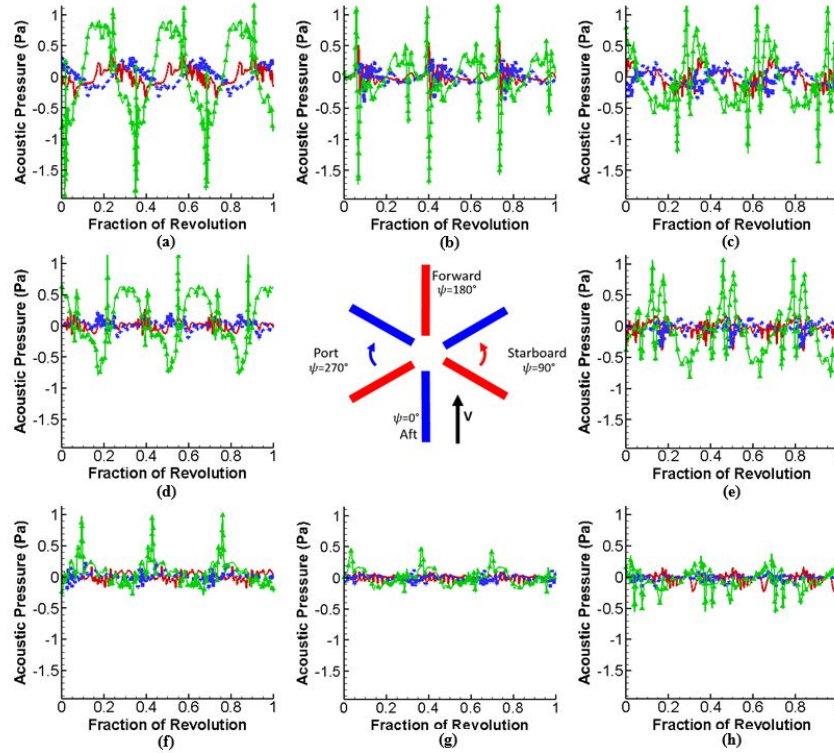


Figure 4.52. RPM comparison of loading acoustic pressure at in-plane observer locations
— \square 276 - - - \diamond 207 — \triangle 179 (M_{AT} : 0.84, 0.72, 0.67)[30].

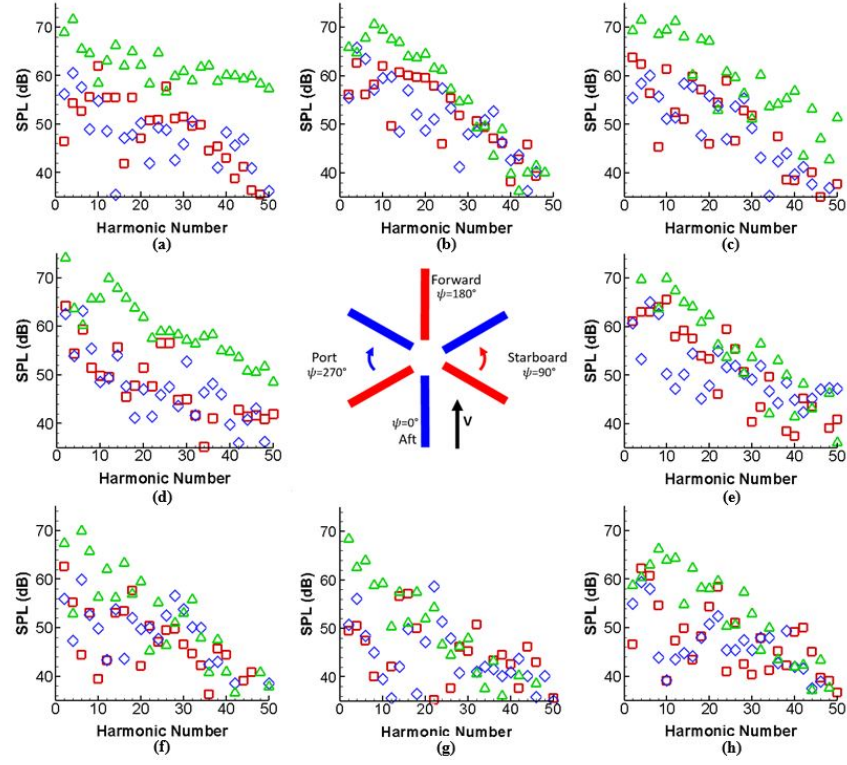


Figure 4.53. RPM comparison of loading acoustic spectra at in-plane observer locations — \square 276 — \diamond 207 — \triangle 179 (M_{AT} : 0.84, 0.72, 0.67)[30].

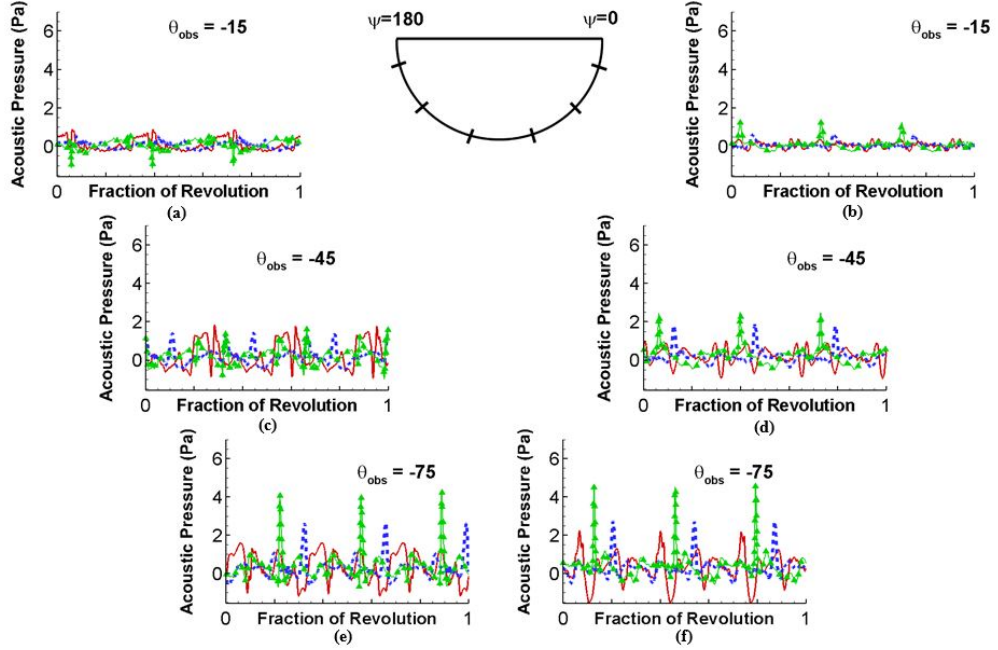


Figure 4.54. RPM comparison of loading acoustic pressure at out-of-plane $\psi=0$ and 180 deg. observer locations — \square 276 — \diamond 207 — \triangle 179 (M_{AT} : 0.84, 0.72, 0.67)[30].

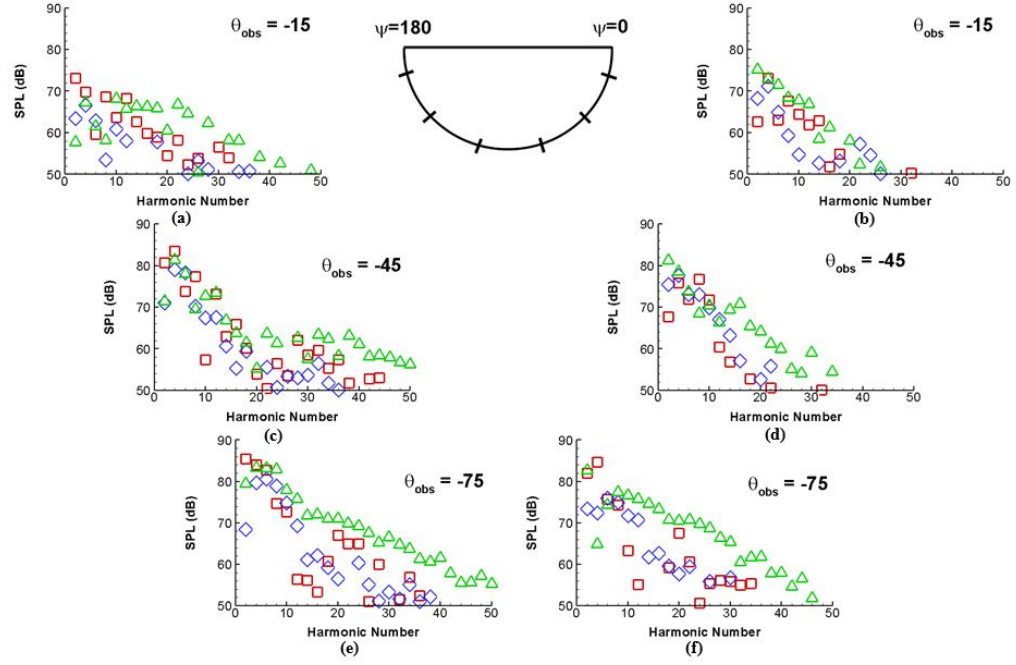


Figure 4.55. RPM comparison of loading acoustic spectra at out-of-plane $\psi=0$ and 180 deg. observer locations — 276 — 207 — 179 (M_{AT} : 0.84, 0.72, 0.67) [30].

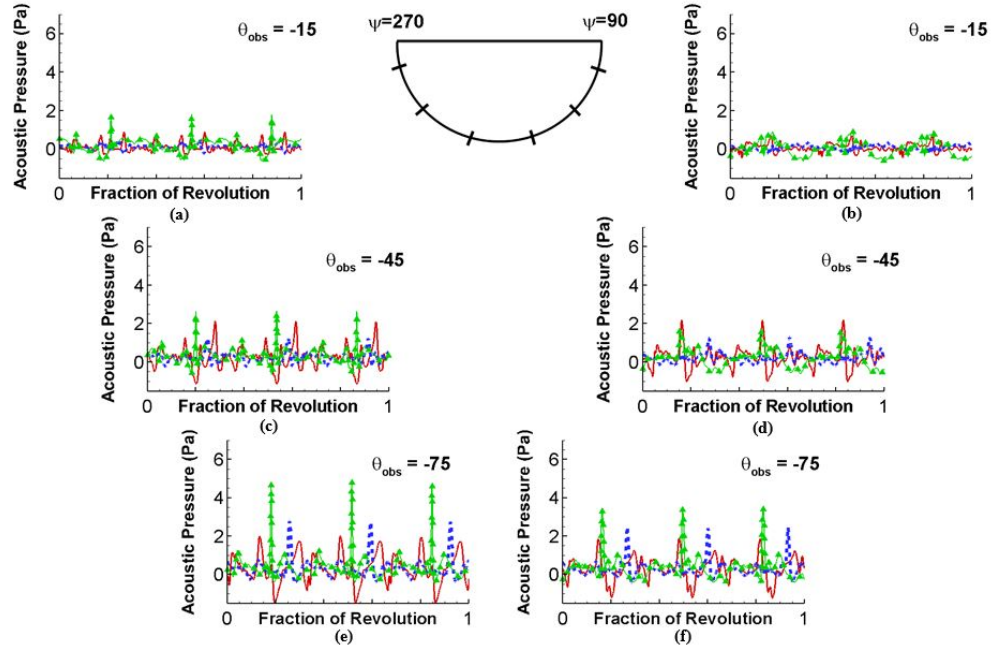


Figure 4.56. RPM comparison of loading acoustic pressure at out-of-plane $\psi=90$ and 270 deg. observer locations — 276 — 207 — 179 (M_{AT} : 0.84, 0.72, 0.67) [30].

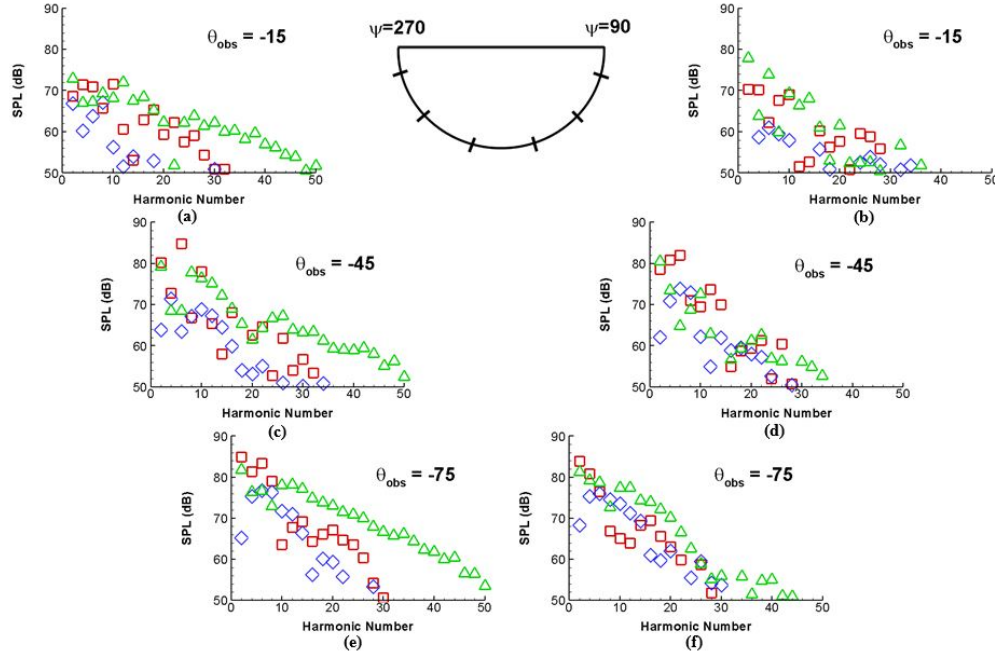


Figure 4.57. RPM comparison of loading acoustic spectra at out-of-plane $\psi=90$ and 270 deg. observer locations — \square 276 — \diamond 207 — \triangle 179 (M_{AT} : 0.84, 0.72, 0.67)[30].

To examine this more thoroughly, a look at the azimuthal blade loading may be helpful. By comparing the rotor loading plots for these cases with RPM variation, shown in Figs. 4.58, 4.59 and 4.60 for 276, 207 and 179 RPM respectively, an increase can be seen in the amount of high lift regions and the number of impulsive loading areas along the advancing sides as the RPM is reduced. Acoustically, larger blade loads and specifically high gradient loading changes result in higher levels of loading acoustic pressures. Hence, these characteristics of the blade loading may explain the out-of-plane loading noise increases with reduction in RPM.

This fact should be kept in mind when slowing the rotor RPM of a compound lift-offset coaxial helicopter to reduce the in-plane thickness noise, as decreasing one noise source for certain observer locations, by changing the RPM, might increase the other noise source at different observer locations (although a more accurate analysis will be needed to confirm this).

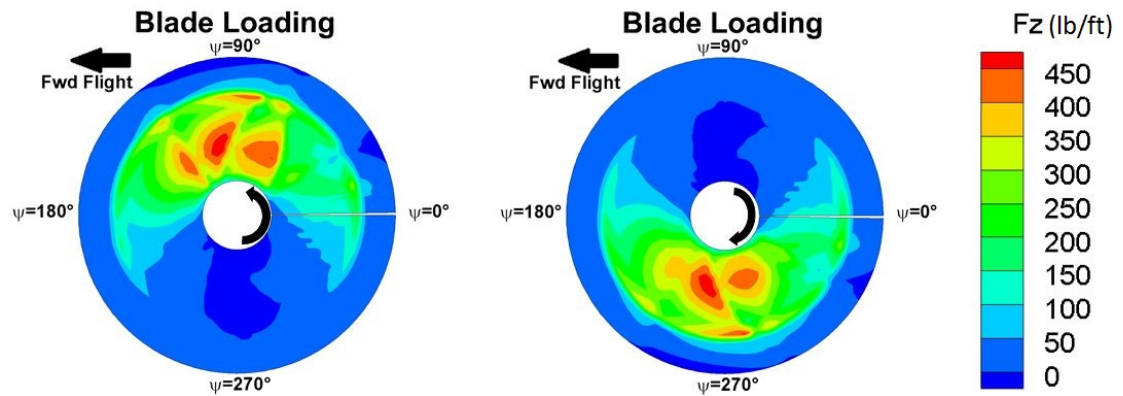


Figure 4.58. 276 RPM rotor lift distribution for both the CCW, upper (left), and the CW, lower (right), rotors [30].

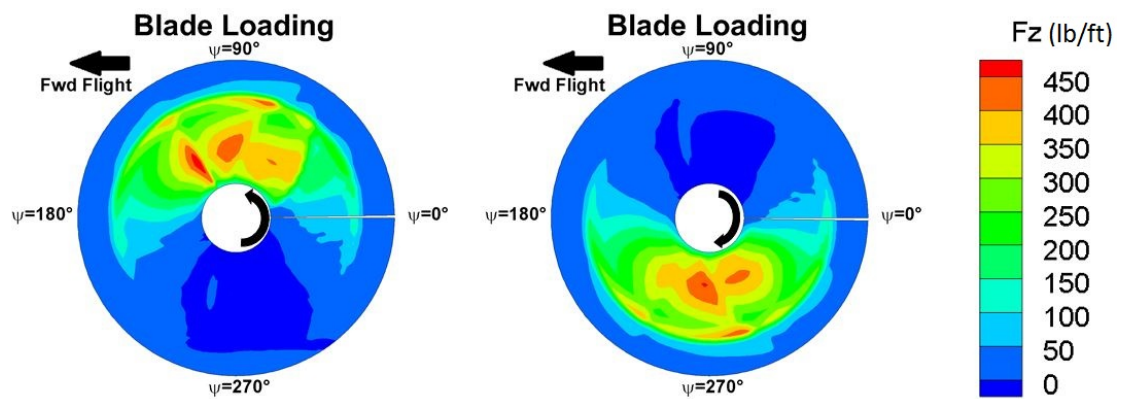


Figure 4.59. 207 RPM rotor lift distribution for both the CCW, upper (left), and the CW, lower (right), rotors [30].

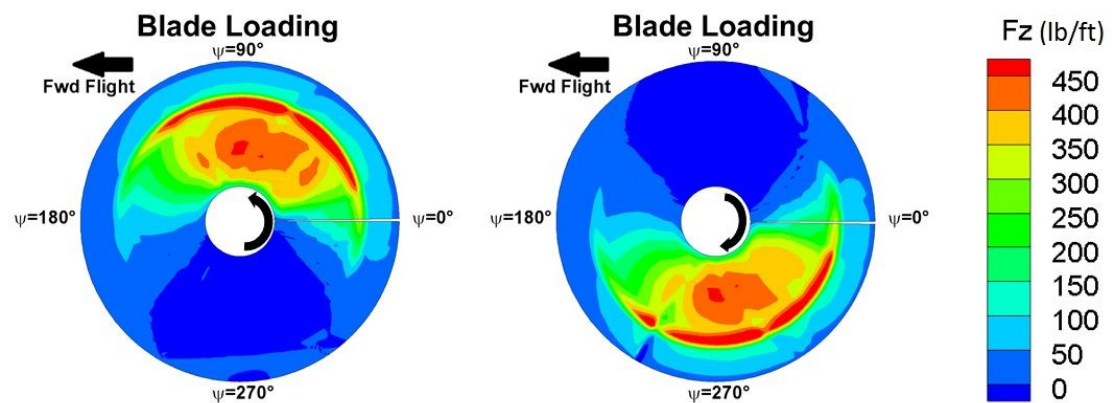


Figure 4.60. 179 RPM rotor lift distribution for both the CCW, upper (left), and the CW, lower (right), rotors [30].

4.5.4 Peak OASPL vs. RPM & M_{AT}

As a summary of this coaxial acoustic RPM reduction study, the Overall Sound Pressure Level (OASPL) is plotted on an observer sphere centered at a point on the shaft axis half way between the two rotors, with an observer sphere radius of 10 rotor radii. OASPL predictions were made on the observer sphere for 7 different RPMs, varying from the maximum of 345 RPM to 196 RPM, each for a fixed forward flight speed of 250 kts. (without including HSI noise). From these spheres, the peak OASPL was extracted for each RPM case and plotted vs. rotor RPM on the bottom x-axis and M_{AT} on the top x-axis in Fig. 4.61. As it can be seen from this graph, the RPM and corresponding M_{AT} , impact the coaxial helicopter noise greatly. For lower RPMs, the noise increases almost linearly with RPM (on a log scale) and at higher RPMs this trend becomes superlinear. Fig. 4.61 serves to further emphasize the overall acoustic advantage of slowing the rotor RPM of a compound coaxial helicopter in high-speed forward flight.

Quantitatively, in conjunction with [16], which showed that a 27% reduction in main rotor RPM, at a forward flight speed of 250 kts., reduced the total power of the XH-59 configuration by 17%, the same RPM reduction decreases the peak OASPL by almost 30 dB! This corresponds to a 97% reduction in acoustic pressure, even without the inclusion of HSI noise! Thus, it is clear that reducing the RPM of a compound lift-offset coaxial helicopter in high-speed forward flight can lead to both a significant performance improvement and noise reduction.

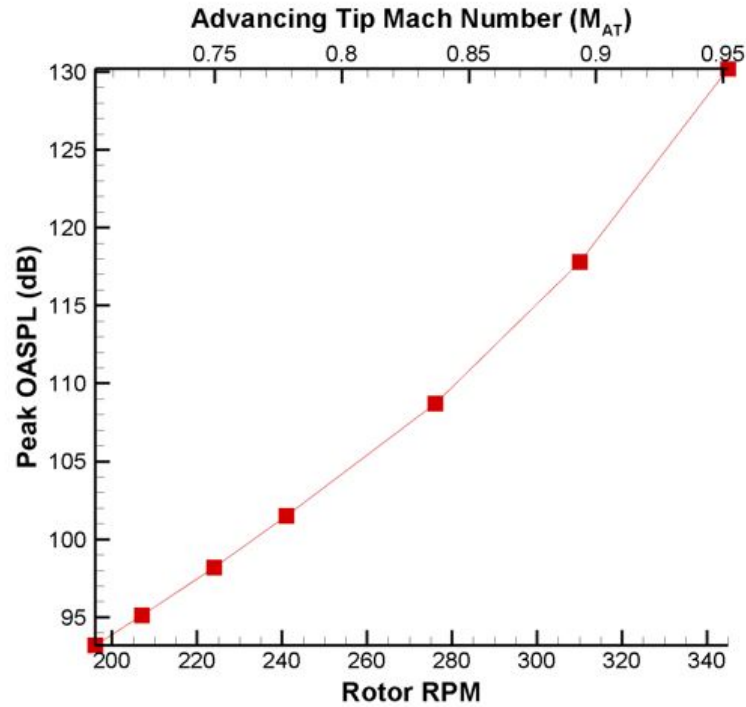


Figure 4.61. Peak OASPL vs. rotor RPM/ M_{AT} for a full sphere of observer locations 10 rotor radii from the coaxial rotor hub, halfway between the two rotors [30].

4.6 Alternative Blade Design

Both the blade crossover locations and the rotor RPM affect the acoustics of the coaxial helicopter in high-speed forward flight. Another parameter to consider is the geometry of the blades, with a specific focus on blade planform and swept blades; meaning that one or more spanwise sections along the blades are shifted forward or rearward in relation to the pitch change axis, such that the blade planform is no longer a straight line.

There are two motivations to study blades with significant forward and rearward sweep on a compound lift-offset coaxial configuration. First, planform changes, such as double sweep near the blade tips (forward then rearward sweep – i.e., like the Blue Edge rotor blades, [31, 32, 33]) have been shown to reduce BVI noise in single main rotor configurations by changing the geometry of the interaction of the blade and the tip vortex. Such a geometry change might also alleviate any blade crossing events in lift-offset coaxial rotors. The second motivation is that changes in geometry will also lead to changes in the constructive/destructive acoustic interference of the blades at various observer locations. Moreover, on a high-speed rotorcraft configuration, like the XH-59, the swept tips could be essential to enabling high forward speeds by delaying and weakening potential shocks on the advancing blades.

4.6.1 Precursor Exploration

Before settling on specific blade designs for comparison, a brief preliminary study was conducted to determine the thickness noise contribution from the inboard and outboard sections of the XH-59 blade. Though it can be recognized from the acoustic theory that an outboard section of a blade, with inherently higher M_{AT} , generates larger acoustic pressures than an inboard section, this investigation served to demonstrate the magnitude of that difference and to find where the focus should be for any blade design changes intended for noise reduction.

In order to carry out this study, the original XH-59 blade surface geometry was split at mid-span (halfway between the root and the tip), resulting in two separate blade geometries: the inboard 50% and the outboard 50%. These two surface geometries, along with the original XH-59 surface geometry, were then input to PSU-WOPWOP with a flight condition of 250 kts. forward flight speed, 332 RPM, resulting in a $0.93 M_{AT}$, with an observer at a distance of 5 rotor radii directly in front and in-plane of the rotor's hub at $\psi = 180$ deg.

Fig. 4.62 shows the result of this computation, comparing the acoustic pressure time histories for one blade passage of all three geometries: the inner 50% blade, the outer 50% blade and the full XH-59 blade. From this plot, it is strikingly clear that the outer 50% of the blade (towards the tip) contributed nearly all of the noise signal to this observer in this flight condition. Thus, the attention for these blade planform changes with sweep will be focused on the outer 50% of the blade span.

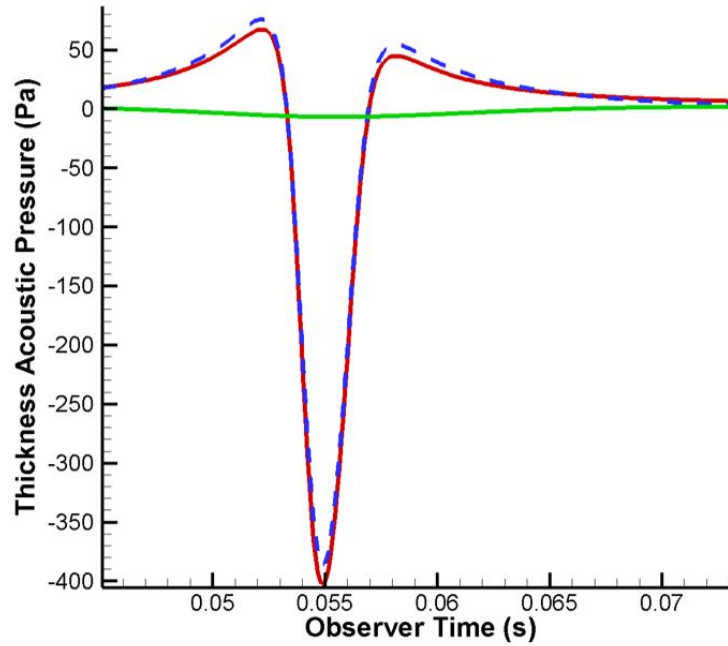


Figure 4.62. Blade section comparison of thickness acoustic pressure at the forward $\psi=180$ deg. observer location — Full XH-59 - - - Outer 50% — Inner 50%.

4.6.2 Configurations

Armed with this knowledge of each blade section noise contribution, multiple blade designs and configurations were considered but a select four of the most interesting and most effective designs considered thus far are discussed in this section and shown in Figs. 4.63 - 4.66.

4.6.2.1 Dual-Swept Tip Blades

In Fig. 4.63, the first dual-swept tip blade design on a coaxial configuration is displayed. This blade design has forward sweep inboard and reward sweep outboard with the forward sweep beginning at 60% of the blade span. Effectively, the overlap region of the blades is altered by employing these coaxial dual-swept tip blades, as the blades no longer completely overlap when a crossover occurs. A second design, shown in Fig. 4.64, features “anti-symmetric” dual-swept tip blades on the lower, CW rotor. This anti-symmetric configuration has rearward sweep inboard and forward sweep outboard (in the opposite manner of the upper, CCW rotor blades), such that when the blades from the two rotors cross, they overlap completely, as can be seen in Fig. 4.64. Acoustically, the opposite sweep on the lower rotor blades causes a non-symmetric noise signal to propagate from the two rotors, in an effort to change the constructive/destructive interference.

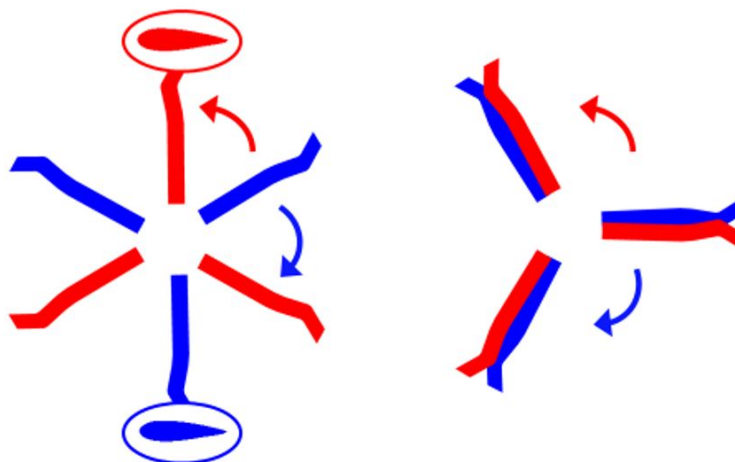


Figure 4.63. Dual-swept tip blade configuration [30].

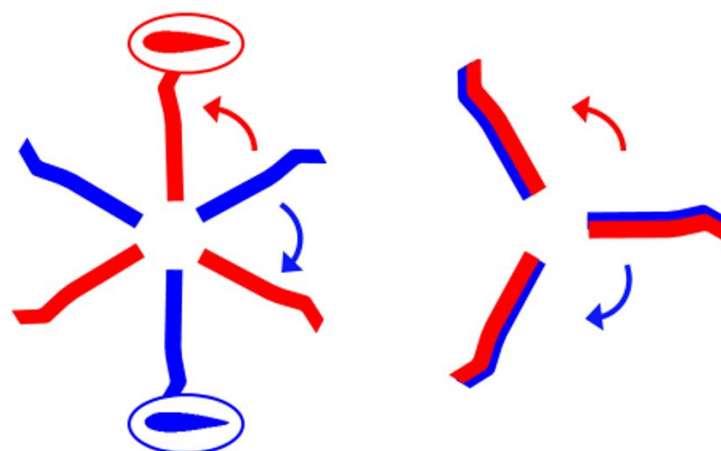


Figure 4.64. “Anti-Symmetric” dual-swept tip blade configuration [30].

4.6.2.2 Curved-Swept Blades

Another planform considered, shown in Fig. 4.65, features only rearward sweep that changes in a “curved” manner from 60% of the blade span to the tip. From this design, an “anti-symmetric” configuration of these rearward curved-swept blades was generated, in the same manner as the previous anti-symmetric design, and is shown in Fig. 4.66. Although this blade design causes a moment about the blade pitch axis because the loads on the blade are not symmetric relative to the pitch axis, this planform design was conceived in order to demonstrate the unique changes in the thickness noise expected by this design. Namely, a delay in the arrival of the acoustic pressure pulses as compared to the signal from the XH-59 blade because the outer 40% of the curved-swept blade is rearward swept and therefore farther from a target observer location at $\psi = 180$ deg. is expected. Secondly, a complete separation of the acoustic pressure pulses from each rotor with the “anti-symmetric” rotor configuration because the tip region of each blade is

at very different locations on the advancing blade is also anticipated. Thus, the thickness noise signal from each rotor's advancing blade to a target observer location at $\psi = 180$ deg. will arrive at different times. The idea for both of these curved-swept blade configurations spawned from the dual-swept tip designs but are intended to be more radical, such that the acoustic effects of the overlap region change (from the curved-swept blades) and the non-symmetric noise signal change (from the anti-symmetric curved-swept blades) are more dramatic.

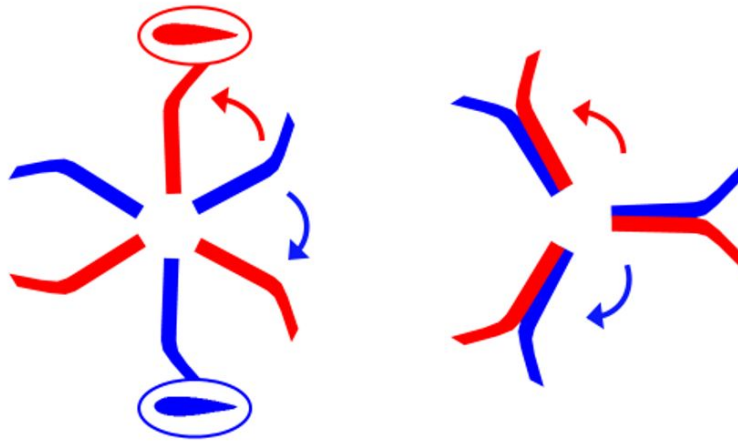


Figure 4.65. Curved-swept tip blade configuration.

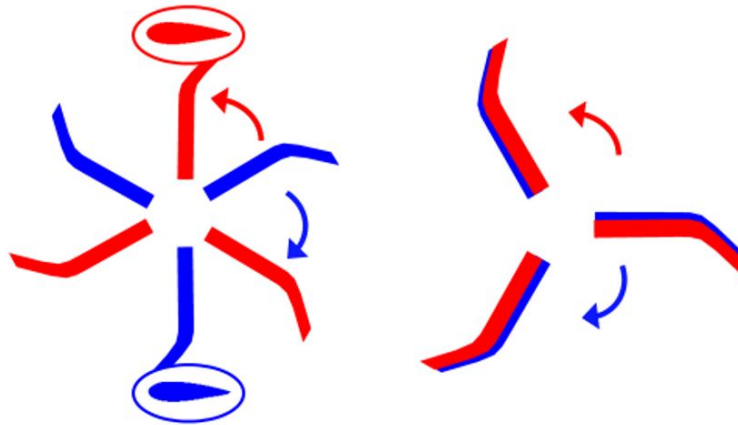


Figure 4.66. "Anti-Symmetric" curved-swept tip blade configuration.

4.6.3 Thickness Noise

With the goal in mind of exploring these blade designs and reducing the relatively large thickness acoustic signal at in-plane observers from the original XH-59 blades, especially at the forward $\psi = 180^\circ$ observer location, only the in-plane thickness noise was considered. Each case of this study was computed for the same flight condition as in the preliminary blade section study with a forward flight speed of 250 kts, 332 RPM, resulting in a $0.93 M_{AT}$, and observer locations at a distance of 5 rotor radii from the rotor's hub.

The thickness noise results for each of the four configurations described in previous sections, as well as the original XH-59 blade design, are plotted on the same graph and shown for all in-plane observers, for half of a rotor revolution, in Figs. 4.67 and 4.68 (Note: the y-axis in plot (b) has a different scale)). Though exact details are hard to pick out from this plot, differences can be seen between thickness noise signals from each configuration and it can be seen that some noise reduction have been achieved.

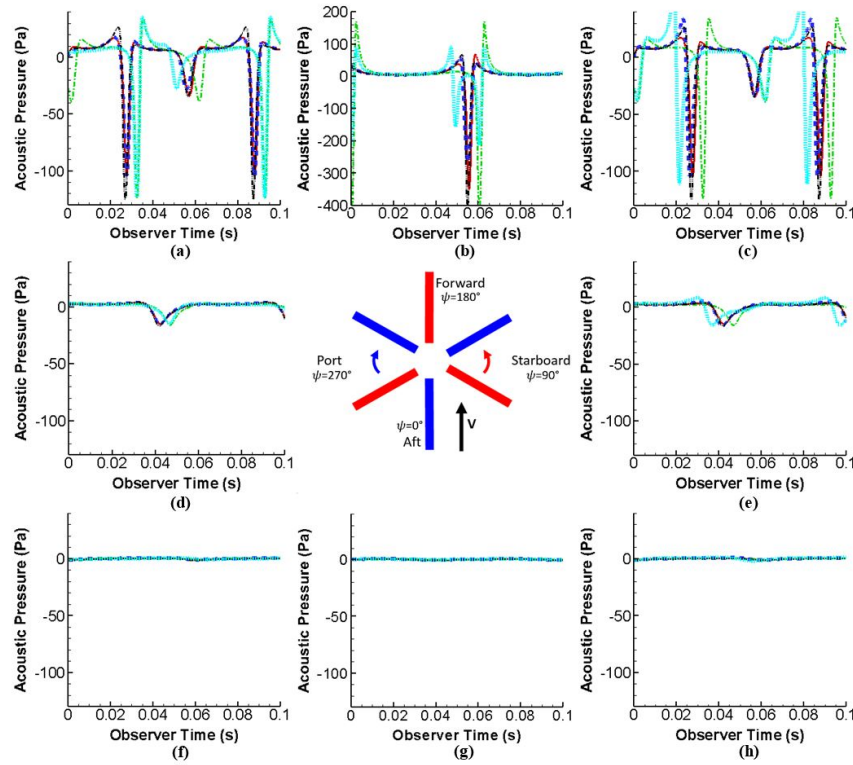


Figure 4.67. Blade design comparison of thickness acoustic pressure at in-plane observer locations
 —◇ Dual-Swept Tip - - -△ Anti-Symmetric Dual-Swept Tip - · - · -○ Curved-Swept Tip
 · · · · ·▶ Anti-Symmetric Curved-Swept Tip - - -□ XH-59.

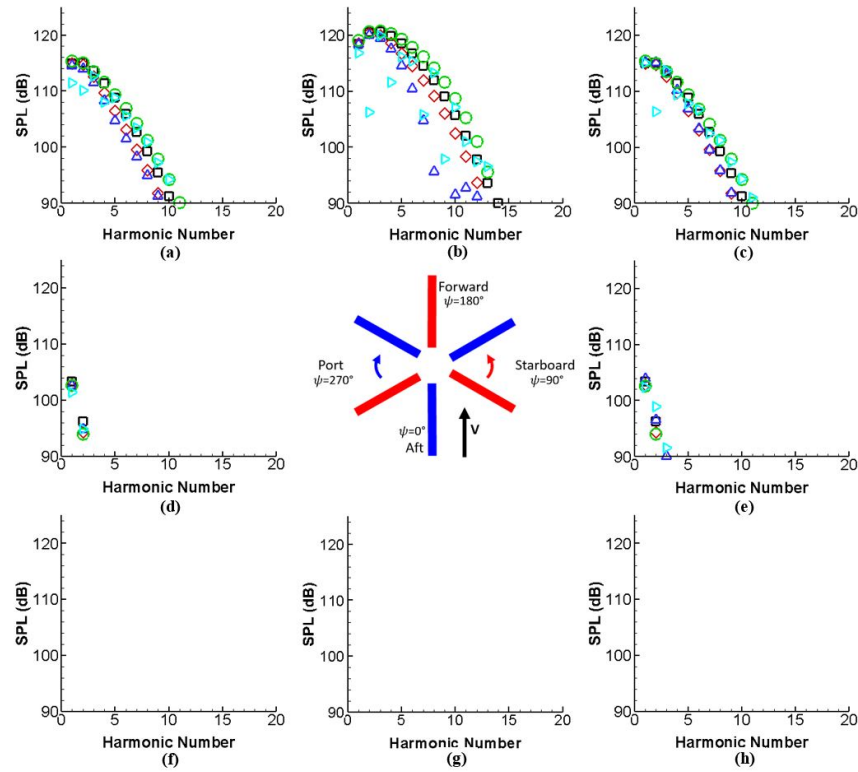


Figure 4.68. Blade design comparison of thickness acoustic spectra at in-plane observer locations
 —◇ Dual-Swept Tip - -△ Anti-Symmetric Dual-Swept Tip - · · · ○ Curved-Swept Tip
 · · · · · △ Anti-Symmetric Curved-Swept Tip - - - □ XH-59.

For a closer look at this comparison, Fig. 4.69 graphs only the thickness acoustic pressure at the $\psi = 180$ deg. observer location, for one blade passage.

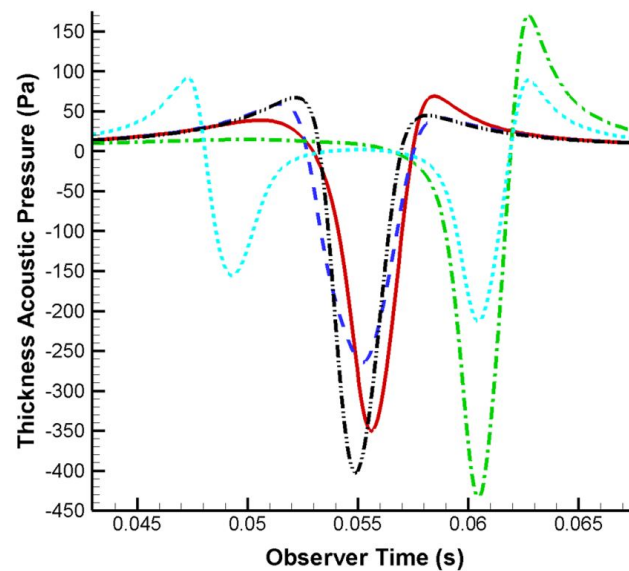


Figure 4.69. Blade design comparison of thickness acoustic pressure at in-plane observer locations
 — Dual-Swept Tip - -△ Anti-Symmetric Dual-Swept Tip - · · · Curved-Swept Tip
 · · · · · △ Anti-Symmetric Curved-Swept Tip - - - XH-59.

As illustrated by Fig. 4.69, each successive design consideration reduced the thickness noise signal at this target observer, with the smallest signal coming from the “anti-symmetric” curved-swept blades. From the previous blade crossover study, it is understood that changing the blade phasing alters the constructive interference of the in-plane thickness noise and the “anti-symmetric” blade configuration has a similar effect. This “anti-symmetric” blade configuration features advancing blades with outboard sections at different distances relative to the forward observer at a given source time. Acoustically, this design both widens the acoustic signal as well as weakens it because the individual signals from the upper and lower rotor blades no longer arrive to the $\psi = 180$ deg. observer at the same instance. Thus, the constructive interference of these two independent signals is not as strong and a widened summation pulse results. If desired, this “anti-symmetric” blade design could be compounded with a different blade crossover position and draw benefits from both configurations, resulting in the weakest acoustic signal at the $\psi = 180$ deg. observer location of the considered dual-swept tip designs. For the “anti-symmetric” curved-swept blade configuration, however, the constructive interference is a non-issue at the $\psi = 180$ deg. observer location because the acoustic pulses from the two blades are not overlapping, so a different blade crossover was not considered in this study.

It should be noted that HSI noise is again not accounted for in these calculations and would have a significant impact; but, sweep near the tip should delay the formation and weaken shocks (and hence reduce the impact of HSI noise to some extent). Nevertheless, these cases are only representative designs that should be further explored with HSI (as well as loading) noise included to substantiate any acoustic benefits.

Conclusion and Future Work

5.1 Conclusions

Acoustic predictions of a model XH-59 compound lift-offset coaxial rotor system for a wide variety of high-speed cases and observer locations have been performed. The acoustic field due to this coaxial rotor design in high-speed forward flight is characterized by potentially large thickness acoustic pulses directly forward of the rotor, constructive and destructive interference of acoustic signals from the upper and lower rotors (especially noticeable in thickness noise) and impulsive loading acoustic pressure jumps (specifically below the tip-path plane). Each of these characteristics are initially concerning because each are associated with potentially high levels of noise. Moreover, the compound lift-offset coaxial helicopter may routinely operate in a high-speed flight condition that potentially excites and amplifies these acoustic characteristics. However, specific design features and/or trim settings inherent to this rotorcraft configuration can result in mitigation of these effects.

The first variable considered was the upper and lower rotor blade crossover locations which enabled directional control of the in-plane thickness noise pulses and provided a way to decrease the out-of-plane loading pressure jumps. Most notably, decreasing the rotor's RPM while maintaining flight speed provides the greatest benefit by reducing the overall acoustic signal, reducing the large in-plane thickness acoustic pulses ahead of the rotor and providing a performance improvement as well, reducing the total power required. Although it was also found that reducing the RPM increased the out-of-plane noise well below the tip-path plane to a significant degree, a more in-depth study is needed in order to validate this claim. Nevertheless, the variable rotor RPM feature is highly valuable on a compound lift-offset coaxial helicopter and should be exploited when possible. Lastly, alternative blade planform designs changed the in-plane thickness noise signal, particularly at the $\psi = 180$ deg. observer location, and the "anti-symmetric" blade configuration provided a significant noise reduction.

The research work outlined in this thesis was a "first look" at the noise generated by a

compound lift-offset coaxial rotor system. There are several areas of acoustic “concern” when considering a compound lift-offset coaxial rotor system, but there are also design changes and operation parameters that can be used to mitigate the potential noise problems.

5.2 Future Work

The findings of this thesis suggest that further and more comprehensive studies of compound lift-offset coaxial rotor system noise would be beneficial. Specifically, a first step in continuing this area of research would be to run full, high-fidelity CFD or free wake inflow modeling for these high-speed cases, extracting the surface pressures or blade loadings on each blade and using those as loading input for PSU-WOPWOP to more accurately predict loading noise. Additionally, analyzing the blade loadings around the azimuth to identify specific interactions and when each occurs would also be useful. Beyond the main coaxial rotor system noise, accounting for other noise sources, such as an aft-mounted propeller and its interaction noise, would make a future study more comprehensive.

With this expanded knowledge, new noise reduction designs and techniques should be explored and those presented in this study should be reevaluated with the new solutions. As compound lift-offset coaxial helicopters become more widely used in both civilian and military applications, noise will become a very important issue that needs to be understood and accurately predicted. This study aimed to serve as an introduction to high-speed compound lift-offset coaxial helicopter noise with the hope of continued research spawning from it.

References

- [1] Leishman, J. G., *Principles of Helicopter Aerodynamics*. New York: Cambridge University Press, 2006.
- [2] Seddon, J., and Newman, S., *Basic Helicopter Aerodynamics*. Blackwell Science Ltd., 2002, pp. xxii.
- [3] Robb, R. L., “Hybrid Helicopters: Compounding the Quest for Speed,” *Vertiflite*, American Helicopter Society, Summer 2006.
- [4] Maisel, M. D., Giulianetti, D. J., Dugan, D. C., “The History of the XV-15 Tilt Rotor Research Aircraft,” The NASA History Series, Monographs in Aerospace #17, NASA SP-2000-4517, 2000.
- [5] Cheney, Jr., M. C., “The ABC Helicopter,” AIAA/AHS VTOL Research Design, and Operations Meeting, AIAA Paper 69-127, Georgia Institute of Technology, Atlanta, GA, February 17-12, 1969.
- [6] Mikheyev, S. V., Bourtsev, B. N., Selemenev, S. V., “Ka-50 Attack Helicopter Acrobatic Flight,” American Helicopter Society 55th Annual Forum, Montreal, Canada, May 1999.
- [7] Ruddell, A. J., “XH-59A ABC Technology Demonstrator Altitude Expansion and Operational Tests,” Technical Report USAVRADCOM-TR-81-D-35, U. S. Army Research and Technology Laboratories (AVRADCOM), December 1981.
- [8] Wall, R., “Hybrid Help,” *Aviation Week and Space Technology*, vol. 173, no. 36, pp. 49, 2011.
- [9] Osborn, K., “Army Propels Next Generation Helicopter Program Forward,” *Defense Tech*, October 8, 2014.
- [10] Majumdar, D., “U.S. Army Selects Bell and Sikorsky/Boeing to Build Prototypes for Next Generation Helicopter Program,” *USNI News*, October 3, 2014.
- [11] Mosher, M., and Peterson, R.L., “Acoustic Measurements of a Full Scale Coaxial Helicopter,” AIAA 8th Aeroacoustics Conference, AIAA Paper 83-0722, Atlanta, GA, April 11-13, 1983.
- [12] Boyd, D., Burley, C., and Conner, D., “Acoustic Predictions of Manned and Unmanned Rotorcraft Using the Comprehensive Analytical Rotorcraft Model for Acoustics (CARMA) Code System,” American Helicopter Society International Specialists’ Meeting on Unmanned Rotorcraft, Chandler, AZ, January 2005.

- [13] Kim, H. W., Kenyon, A. R., Duraisamy, K., and Brown, R. E., "Interactional Aerodynamics and Acoustics of a Propeller-Augmented Compound Coaxial Helicopter," American Helicopter Society Specialists' Conference on Aeromechanics, San Francisco, CA, January 2008.
- [14] Kim, H. W., Duraisamy, K., and Brown, R. E., "Aeroacoustics of a Coaxial Rotor in Level Flight," American Helicopter Society 64th Annual Forum, Montreal, Canada, April 2008.
- [15] Barbely, N. L., Komerath, N. M., Novak, L. A., "A Study of Coaxial Rotor Performance and Flow Field Characteristics," American Helicopter Society Specialists' Conference on Aeromechanics, San Francisco, CA, January 2016.
- [16] Jacobellis, G., Gandhi, F., and Floros, M., "A Physics-Based Approach to Trim Optimization of Coaxial Helicopters in High-Speed Flight," Paper AHS2015-000044, 71st Annual Forum of the American Helicopter Society, Virginia Beach, VA, May 2015.
- [17] Passe, B., Sridharan, A., and Baeder, J., "Computational Investigation of Coaxial Rotor Interactional Aerodynamics in Steady Forward Flight," Paper AIAA 2015-2883, 33rd AIAA Applied Aerodynamics Conference, Dallas, TX, June 2015.
- [18] Walsh, D., Weiner, S., Arifian, K., Lawrence, T., Wilson, M., Millott, T., and Blackwell, R., "High Airspeed Testing of the Sikorsky X2 Technology Demonstrator," American Helicopter Society 67th Annual Forum, Virginia Beach, VA, May 2011.
- [19] Schmaus, J. and Chopra, I., "Aeromechanics for a High Advance Ratio Coaxial Helicopter," American Helicopter Society 71st Annual Forum, Virginia Beach, VA, 2015.
- [20] Brentner, K. S., and Farassat, F., "Helicopter Noise Prediction: The Current Status and Future Direction," *Journal of Sound and Vibration*, vol. 170, no. 1, pp. 79-96, 1994
- [21] Magliozzi, B., Metzger, F.B., Bausch, W., King, R.J., "A Comprehensive Review of Helicopter Noise Literature," FAA ADA014640, June 1975.
- [22] Brentner, K. S., and Farassat, F., "Modeling Aerodynamically Generated Sound of Helicopter Rotors," *Progress in Aerospace Sciences*, Vol. 39, (2-3), Feb-April 2003, pp. 83-120.
- [23] Ffowcs Williams, J. E. and Hawkins, D. L., "Sound Generated by Turbulence and Surfaces in Arbitrary Motion," *Philosophical Transactions of the Royal Society*, Vol. 264, No. 1151, 1969, pp. 321-342.
- [24] Saberi, H., Khoshlahjeh, M., Ormiston, R., and Rutkowski, M., "Overview of RCAS and Application to Advanced Rotorcraft Problems," AHS Fourth Decennial Specialists Conference on Aeromechanics, San Francisco, CA, January 2004.
- [25] Peters, D. A., and He, C. J., "Comparison of Measured Induced Velocities with Results from a Closed-form Finite State Wake Model in Forward Flight," American Helicopter Society 45th Annual Forum, Boston, MA, May 1989.
- [26] Brès, G. A., Brentner, K. S., Perez, G., and Jones, H. E., "Maneuvering rotorcraft noise prediction," *Journal of Sound and Vibration*, 275(3-5):719-738, August 2004.
- [27] Brès, G. A., "Modeling the noise of arbitrary maneuvering rotorcraft: Analysis and implementation of the PSU-WOPWOP noise prediction code," M.S. thesis, Department of Aerospace Engineering, The Pennsylvania State University, June 2002.
- [28] Perez, G., "Investigation of the Influence of Maneuver on Rotorcraft Noise," M.S. thesis, Department of Aerospace Engineering, The Pennsylvania State University, June, 2002.

- [29] Linden, A., “S-69 (XH-59A) Advancing Blade Concept Demonstrator,” [Online], <http://www.sikorskyarchives.com/S-69%20%28XH-59A%29.php>, April, 2013.
- [30] Walsh, G., Brentner, K.S., Jacobellis, G., Gandhi, F., “An Acoustic Investigation of a Coaxial Helicopter in High-Speed Flight,” Paper AHS2016-0322, 72nd Annual Forum of the American Helicopter Society, West Palm Beach, FL, May 2016.
- [31] Rauch, P., Gervais, M., Cranga, P., Baud, A., Hirsch, J-F., Walter, A., and Beaumier, P., “Blue Edge: The Design, Development and Testing of a New Blade Concept,” Paper AHS2011-000043, 67th Annual Forum of the American Helicopter Society, Virginia Beach, VA, May 2011.
- [32] Paur, J., “Eurocopter Moves One Step Closer To ‘Whisper Mode’.” 2010 Feb 25, 2010 [accessed 3/4/2016]; Available from: <http://www.wired.com/2010/02/eurocopter-moves-one-step-closer-to-whisper-mode/>
- [33] Nelms, D. (2015). “New Eco-Friendly Bluecopter Unveiled,” *Vertiflite* 61(5): pp. 26-28.

Appendix A

BladeMaker: PSU-WOPWOP Geometry

The surface geometry input for PSU-WOPWOP in this research was created in BladeMaker. BladeMaker is a Fortran based code that takes spanwise definitions of a blade from a user-defined input file to create full blade surface geometry. Standard 4 and 5 digit NACA airfoils can be generated in BladeMaker and taper, sweep, offset, flex and twist of the blade can also be specified. Through the use of this code, distributed blade geometry files, which will then be used in PSU-WOPWOP for thickness noise prediction, are output. These distributed blade geometry files are in ASCII format and are converted to binary format by a code called 'GEOMETRY.INPUT' and then can be input to PSU-WOPWOP.

A.1 Blade Generation Procedure

The input file to the BladeMaker code is the 'blade.config' file. Below is an example 'blade.config' input file which was used to generated the XH-59 blades for this thesis.

```
number leading edge, number trailing edge, number span while creating blade
8 6 500
number of points for airfoil cross section
4
the locations
0.00000000 0.40000000 0.78000000 1.00000000
the values
0026 23018 23012 23012
number of points for taper ratio
2
the locations
0.0 1.000000
the values
1.00000000 1.000000
number of points for twist
17
the locations
0.0 0.0625 0.125 0.1875 0.25 0.3125 0.375 0.4375 0.5
```

```

0.5625 0.625 0.6875 0.75 0.8125 0.875 0.9375 1.0
the values
0.0 0.0804 0.0716 0.0687 0.0598 0.0497 0.0386 0.0269 0.0146
0.0023 -0.0099 -0.0217 -0.0327 -0.0426 -0.0513 -0.0591 -0.0666
number of points for sweep
2
the locations
0.00000000 1.00000000
the values
0.00000000 0.00000000
number of points for flex
2
the locations
0.00000000 1.00000000
the values
0.00000000 0.00000000
forward offset of blade
2
the locations
0.00000000 1.00000000
the values
0.130225 0.130225
number of points for dx
26
the locations
0.000 .02167 0.2712 0.3458 0.4183 0.4883 0.551 0.6186 0.6783 0.7524 0.8077
0.8276 0.8468 0.8652 0.8829 0.8995 0.9152 0.9297 0.9430 0.9551 0.9658 0.9751
0.9830 0.9894 0.9943 1.000
the values
0.1835 0.1835 0.4145 0.4042 0.3914 0.3758 0.3581 0.3383 0.3164 0.4966 0.1106
0.1073 0.1035 0.0991 0.0942 0.0887 0.0828 0.0765 0.0697 0.0626 0.0551 0.0473
0.0393 0.0311 0.0227 0.0197
start chord
0.5209
start position
1.0973
end position
5.4864

```

Editing this file is fairly straight forward but a few key delicacies need to be known to get everything correct. It is set up to be readable (with labels above almost each number) and additional context to the ‘blade.config’ file is provided here:

1. The first number in the code, ‘number leading edge’ corresponds to the number of grid points from the leading edge of the blade, along the upper surface of the chord, to the quarter chord. And the next number is the number of grid points from the quarter-chord to the trailing edge, again along the upper surface. This exact grid is then copied to the lower surface of the chord. The ‘number span’ is not used at this time.
2. The next 5 numbers define the airfoil along the blade. The number of points for the airfoil cross section must be at least 2 (with default locations of 0.000 (root) and 1.000 (tip) if there is a constant chord along the span). All 4-digit NACA airfoils can be represented by Blade-

Maker and ‘the values’ correspond to the 4-digit number of the airfoil. If the airfoil changes along the span, locations and values can be added but the number of points must be equal to the number ‘locations’ and ‘values’.

3. Next is taper ratio, twist, sweep, flex and forward offset of the blade all in a similar format to the airfoil definition. It should be noted that the twist values are in radians and a negative value causes a nose-down twist.
4. The next 6 lines after these define the grid spacing along the span. The numbers under ‘the values’ are the most important here. To make the grid spacing constant, keep those two numbers the same value, or if ‘number of points for dx’ is still 2 and you have two different numbers under ‘the values’, BladeMaker will create a linear grid spacing along the span.
5. Lastly, is ‘start chord’, which is the length of the chord at the root in meters, ‘start position’ which takes into account the root cut out in meters (0.0000 if no root cut out) and ‘end position’ which defines the blade radius in meters.

Once the ‘blade.config’ file is set up, it should be placed within the same directory as ‘BladeMaker.exe.’ The BladeMaker code can then be executed by opening the ‘BladeMaker.exe’ file. Running the BladeMaker code with the proper blade specifications in the ‘blade.config’ file yields 3 output files: ‘blade.x’, ‘blade.fn’ and ‘blade.nam’.

In order to create the PSU-WOPWOP patch geometry input file, these 3 BladeMaker output files need to be input to ‘GEOMETRY_INPUT.’ ‘GEOMETRY_INPUT’ converts these BladeMaker files to a binary format needed for PSU-WOPWOP. Both the blade.x’ and ‘blade.fn’ files need to be within the same directory as the ‘GEOMETRY_INPUT.exe’ in order to be converted. Running the ‘GEOMETRY_INPUT’ code is not difficult but users are prompted for specific inputs: IMAX, JMAX and patch name. IMAX and JMAX are the first two numbers, respectively, in both the ‘blade.x’ and ‘blade.fn’ files and the patch name can be user-defined and does not affect output (commonly ‘blade’). Below is a screen shot example execution of the code for clarity, where ‘blade’ is the patch name, IMAX is 18 and JMAX is 28. Output from ‘GEOMETRY_INPUT’ is ‘geom_binary.dat’ which can be used as a PSU-WOPWOP patch geometry file.

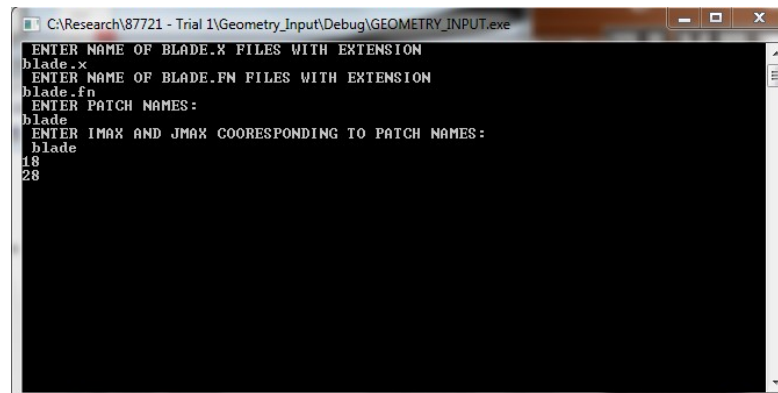


Figure A.1. ‘GEOMETRY_INPUT’ Example.

Appendix B

Integration of RCAS and PSU-WOPWOP

B.1 RCAS Output to ‘.txt’ files via MATLAB

The blade loadings (X, Y, and Z direction forces and moments) output from RCAS for both the upper and lower rotors are contained in one large file titled ‘bladeloads001.rep.’ The following is a MATLAB script used to extract the necessary loading from this file for input to PSU-WOPWOP.

```
filename    = 'bladeloads001.rep'; \%Name of file to be read in
sets        = 1:6;                \% 3 force + 3 moment
nrow        = 359;                \% rows of data -1
ncol        = 48;                 \% columns of data per set
colpp       = 5;                  \% columns of data per page
skiprow     = 11;                 \% rows in header
r1          = 8;                  \% initialize first row to read

[azi,data] = readrcasfile(filename,sets,colpp,ncol,r1,nrow,skiprow);
X_Force = data{1,1};
Y_Force = data{1,2};
Z_Force = data{1,3};
X_Moment = data{1,4};
Y_Moment = data{1,5};
Z_Moment = data{1,6};
upper_rotor_X_Force = X_Force(:,1:24);
upper_rotor_Y_Force = Y_Force(:,1:24);
upper_rotor_Z_Force = Z_Force(:,1:24);
upper_rotor_X_Moment = X_Moment(:,1:24);
upper_rotor_Y_Moment = Y_Moment(:,1:24);
upper_rotor_Z_Moment = Z_Moment(:,1:24);
lower_rotor_X_Force = X_Force(:,25:48);
lower_rotor_Y_Force = Y_Force(:,25:48);
lower_rotor_Z_Force = Z_Force(:,25:48);
lower_rotor_X_Moment = X_Moment(:,25:48);
```

```

lower_rotor_Y_Moment = Y_Moment(:,25:48);
lower_rotor_Z_Moment = Z_Moment(:,25:48);

load('geom24.mat')

col =2.87;      \%deg found in rcasmaster001.log

```

This loop is used to reorient the coordinates for x aft and z up

```

for i = 1:24
    for j = 1:360
        upper_rotor_X_Force(j,i) = upper_rotor_X_Force(j,i)*cosd(col)*dx(i);
        upper_rotor_Z_Force(j,i) = upper_rotor_Z_Force(j,i)*cosd(col)*dx(i);
        lower_rotor_X_Force(j,i) = lower_rotor_X_Force(j,i)*-1*cosd(col)*dx(i);
        lower_rotor_Z_Force(j,i) = lower_rotor_Z_Force(j,i)*cosd(col)*dx(i);
    end
end

fileID = fopen('CCW\_loading.txt','w+');
for k = 1:360
    for j = 1:24
        fprintf(fileID,'%2.6f\r\n',upper_rotor_X_Force(k,j));
    end
end

for k = 1:360
    for j = 1:24
        fprintf(fileID,'%2.6f\r\n',upper_rotor_Y_Force(k,j));
    end
end

for k = 1:360
    for j = 1:24
        fprintf(fileID,'%2.6f\r\n',upper_rotor_Z_Force(k,j));
    end
end
fclose(fileID);

fileID = fopen('CW\_loading.txt','w+');
for k = 1:360
    for j = 1:24
        fprintf(fileID,'%2.6f\r\n',lower_rotor_X_Force(k,j));
    end
end

for k = 1:360
    for j = 1:24
        fprintf(fileID,'%2.6f\r\n',lower_rotor_Y_Force(k,j));
    end
end

```



```

for k = 1:360
    for j = 1:24
        fprintf(fileID,'%2.6f\r\n',lower\_rotor\_Z\_Force(k,j));
    end
end

fclose(fileID);

```

B.2 Output '.txt' files to Binary files

The two text files output from this MATLAB script are then input into this FORTRAN subroutine to convert the blade loading into the binary format that PSU-WOPWOP requires.

```

PROGRAM MAIN
    USE constantGeometryFileParameter
    USE periodicPressureFileParameter
    IMPLICIT NONE
    CHARACTER(99):: Pressure_ASCII, Pressure_BINARY, Pressure2_ASCII,
    Pressure2_BINARY, Geom_ASCII, Geom_BINARY, Geom2_ASCII, Geom2_BINARY,
    character(32) :: Cpbottom, Cpupper
    integer,parameter :: jm=24, npsi=360, im=28, c=340
    integer:: i,j,i1,j1,k
    real,dimension(jm,npsi) :: cl, Mach
    real(kind=4) :: x2(im,jm), R(jm)
    real(kind=4) :: Fx(360,24), Fy(360,24), Fz(360,24)
    real(kind=4) :: psi(npsi)

    ! Names of output files

    ! ASCII output files
    Pressure_ASCII = 'pressure_ASCII.txt'
    Pressure2_ASCII = 'pressure_reverse_ASCII.txt'

    ! Binary output files
    Pressure_BINARY = 'pressure_binary.dat'
    Pressure2_BINARY = 'pressure_binary_reverse.dat'

    OPEN(1, FILE='PSI_RPI.txt', STATUS='OLD', ACTION='READ')
    do i=1,npsi
        READ(1,*) psi(i)
    enddo

    OPEN(1, FILE='R_RPI.txt', STATUS='OLD', ACTION='READ')
    do i=1,jm
        READ(1,*) R(i)
    enddo

    OPEN(3, FILE='CCW_loading.txt', STATUS='OLD', ACTION='READ')

```

[illegible]

```

subroutine writeINTPressureFile(lxCpl,lyCpl,lzCpl,psi,im,jm,km,
                               fileName, fileName1)

use periodicPressureFileParameter
implicit none
integer,intent(in):: im, jm, km
real(kind=4),intent(in):: lxCpl(km,jm), lyCpl(km,jm), lzCpl(km,jm), psi(km)
character(len=99),intent(in) :: fileName, fileName1
integer :: unitNumber=12, unitNumber1=13
integer :: i, j, k
real :: angularVel = 35.027
real :: pi = 3.1415

open(unit=unitNumber, file=trim(fileName), status="unknown")
open(unit=unitNumber1, file=trim(fileName1), &
form="binary", status="unknown")

!!! write file in ASCII
write(unitNumber,*) magic_number
write(unitNumber,*) version_number_1, version_number_2
write(unitNumber,*) comment
write(unitNumber,*) fs1
write(unitNumber,*) fs2
write(unitNumber,*) fs3
write(unitNumber,*) fs4
write(unitNumber,*) fs5
write(unitNumber,*) fs6
write(unitNumber,*) fs7
write(unitNumber,*) fs8
write(unitNumber,*) fs9
write(unitNumber,*) fs10
write(unitNumber,*) num_zone
write(unitNumber,*) zone_list

write(unitNumber,*) name_zone
write(unitNumber,*) 2.0*pi/angularVel
write(unitNumber,*) km
write(unitNumber,*) 1,jm

!!! write file in binary
write(unitNumber1) magic_number
write(unitNumber1) version_number_1, version_number_2
write(unitNumber1) comment
write(unitNumber1) fs1
write(unitNumber1) fs2
write(unitNumber1) fs3
write(unitNumber1) fs4
write(unitNumber1) fs5
write(unitNumber1) fs6

```



```

! 2 : data is periodic
! 3 : data is aperiodic

fs5=1,& ! 1 : if the data is node-centered
! 2 : if it is face-centered

fs6=2,& ! 1 : if data is surface pressure
! 2 : if data is surface loading vector
! 3 : if data is flow parameters

fs7=3,& ! if reference frame is..
! 1 : stationary, ground-fixed frame
! 2 : rotating ground-fixed frame
! 3 : patch-fixed frame

fs8=1,& ! 1: if data is single precision
! 2: if it is double precision

fs9=0,& ! reserved for future use

fs10=0 ! reserved for future use

! number of zones with loading data
integer,parameter::num_zone=1

! a list of the zones with loading data
! (correspond to geometry file)
integer::zone_list(num_zone)=(/1/)

! specify names of zones with loading data
character(32)::name_zone(num_zone)=(/ 'periodic pressure' /)

end module periodicPressureFileParameter

```

Appendix C

PSU-WOPWOP Changes of Base and Namelist

PSU-WOPWOP uses a variable method for defining surface and observer motion known as changes of base (COB). These COB can specify a single translation, rotation, axis change or a combination of all three. When COB are used together, complex object motion, such as forward flight of a coaxial rotor system, can be properly analyzed. The rotation and forward motion of the coaxial rotor system studied in this research is simulated through the use of COB and the observers are “attached” to the aircraft such that the observers follow the aircraft motion. Example COB within a PSU-WOPWOP input namelist file are presented below and are denoted by ‘&CB.’ This namelist file is set up such that PSU-WOPWOP computes thickness and loading noise with the given input data.

C.1 Example Namelist

```
&EnvironmentIn
  nbSourceContainers = 1
  nbObserverContainers = 1
  ASCIIOutputFlag = .true.
  OASPLdBFlag = .false.
  OASPLdBAFlag = .false.
  spectrumFlag = .true.
  SPLdBFlag = .true.
  SPLdBAFlag = .true.
  acousticPressureFlag = .true.
  pressureGradient1AFlag = .false.
  sigmaflag = .false.
  loadingsigmaflag = .true.
  areaSigmaFlag = .true.
  loadingNoiseSigmaFlag = .true.
  pressureFileName = "pressure_blade_RPI_TOTAL_FWD_PSI180"
  OASPLFileName = "OASPL_blade_RPI"
  SPLFileName = "SPL_blade_RPI_TOTAL_FWD_PSI180"
```

```

    debugLevel = 12
    thicknessNoiseFlag = .false.
    loadingNoiseFlag = .false.
    totalNoiseFlag = .true.
/

&EnvironmentConstants
rho = 1.225
c = 343.0
/

&ObserverIn
nt = 2048
xLoc = -54.8          !10 Rotor radii ahead
yLoc = 0.0
zLoc = 0.0
tMin = 0.0
tMax = 0.2174967      !1 Rev
attachedTo = "Aircraft"
/

&ContainerIn
Title = "Aircraft"
nbContainer = 4
nbBase = 1
dTau = 5e-4
/

&CB                      !FWD Vel
translationType='KnownFunction'
VH = -128.61, 0.0, 0.0    !V_inf = 421.95 ft/s = 250 kts. = 128.61 m/s
/
&ContainerIn
Title = "CCW Rotor_Thickness"
nbContainer = 3
nbBase = 2
/
&CB
Title = "Rotor Rotation"
rotation = .true.
AngleType = "KnownFunction"
AxisType = "Timeindependent"
Omega = 28.8878
AxisValue = 0.0,0.0,1.0
PSIO = -1.5707963267948966192313216916398
/
&CB                      !Offset between the two rotors
translationType='KnownFunction'
YO = 0.0, 0.0, 0.381      !total offset is 30 inches = 0.762m
/

```

```

&ContainerIn
title="CCW_blade_1"
patchGeometryFile="geom_binary.dat"
nbBase = 0
/

&ContainerIn
title="CCW_blade 2"
patchGeometryFile="geom_binary.dat"
nbBase = 1
/
    &CB                                !In-rotor-plane rotation for a 3-bladed rotor
    Title="Constant Rotation"
    AxisType="TimeIndependent"
    AngleType="TimeIndependent"
    axisValue=0.0,0.0,1.0
    angleValue = 2.094395102
/

&ContainerIn
title="CCW_blade 3"
patchGeometryFile="geom_binary.dat"
nbBase = 1
/
    &CB                                !In-rotor-plane rotation for a 3-bladed rotor
    Title="Constant Rotation"
    AxisType="TimeIndependent"
    AngleType="TimeIndependent"
    axisValue=0.0,0.0,1.0
    angleValue = 4.188790205
/

&ContainerIn
Title = "CCW Rotor_Loading"
nbContainer = 3
nbBase = 2
/
    &CB
    Title = "Rotor Rotation"
    rotation = .true.
    AngleType = "KnownFunction"
    AxisType = "Timeindependent"
    Omega = 28.8878
    AxisValue = 0.0,0.0,1.0
    PSIO = -1.5707963267948966192313216916398
/
    &CB                                !Offset between the two rotors
    translationType='KnownFunction'
    Y0 = 0.0, 0.0, 0.381                !total offset is 30 inches = 0.762m
/

```



```

&ContainerIn
title="CCW_blade_1_loading"
patchGeometryFile="geom_binary_single_comp.dat"
patchLoadingFile="pressure_binary.dat"
nbBase = 0
/

&ContainerIn
title="CCW_blade_2_loading"
patchGeometryFile="geom_binary_single_comp.dat"
patchLoadingFile="pressure_binary.dat"
nbBase = 1
periodicKeyoffset = 120
/

    &CB                                !In-rotor-plane rotation for a 3-bladed rotor
    Title="Constant Rotation"
    AxisType="TimeIndependent"
    AngleType="TimeIndependent"
    axisValue=0.0,0.0,1.0
    angleValue = 2.094395102
/

&ContainerIn
title="CCW_blade_3_loading"
patchGeometryFile="geom_binary_single_comp.dat"
patchLoadingFile="pressure_binary.dat"
nbBase = 1
periodicKeyoffset = 240
/

    &CB                                !In-rotor-plane rotation for a 3-bladed rotor
    Title="Constant Rotation"
    AxisType="TimeIndependent"
    AngleType="TimeIndependent"
    axisValue=0.0,0.0,1.0
    angleValue = 4.188790205
/

&ContainerIn
Title = "CW Rotor_Thickness"
nbContainer = 3
nbBase = 2
/

    &CB
    Title = "Rotor Rotation"
    rotation = .true.
    AngleType = "KnownFunction"
    AxisType = "Timeindependent"
    Omega = -28.8878
    AxisValue = 0.0,0.0,1.0

```

```

PSIO = -1.5707963267948966192313216916398
/
&CB                                !Offset between the two rotors
translationType='KnownFunction'
YO = 0.0, 0.0, 0.381                !total offset is 30 inches = 0.762m
/

&ContainerIn
title="CW_blade 1"
patchGeometryFile="geom_binary_reverse.dat"
nbBase = 0
/

&ContainerIn
title="CW_blade 2"
patchGeometryFile="geom_binary_reverse.dat"
nbBase = 1
/
    &CB                                !In-rotor-plane rotation for a 3-bladed rotor
    Title="Constant Rotation"
    AxisType="TimeIndependent"
    AngleType="TimeIndependent"
    axisValue=0.0,0.0,1.0
    angleValue = -2.094395102
/

&ContainerIn
title="CW_blade 3"
patchGeometryFile="geom_binary_reverse.dat"
nbBase = 1
/
    &CB                                !In-rotor-plane rotation for a 3-bladed rotor
    Title="Constant Rotation"
    AxisType="TimeIndependent"
    AngleType="TimeIndependent"
    axisValue=0.0,0.0,1.0
    angleValue = -4.188790205
/

&ContainerIn
Title = "CW Rotor_Loading"
nbContainer = 3
nbBase = 2
/
    &CB
    Title = "Rotor Rotation"
    rotation = .true.
    AngleType = "KnownFunction"
    AxisType = "Timeindependent"
    Omega = -28.8878

```

```

AxisValue = 0.0,0.0,1.0
PSIO = -1.5707963267948966192313216916398
/
&CB                                !Offset between the two rotors
translationType='KnownFunction'
YO = 0.0, 0.0, 0.381              !total offset is 30 inches = 0.762m
/

&ContainerIn
title="CW_blade_1_loading"
patchGeometryFile="geom_binary_reverse_single_comp.dat"
patchLoadingFile="pressure_binary_reverse.dat"
nbBase = 0
/

&ContainerIn
title="CW_blade_2_loading"
patchGeometryFile="geom_binary_reverse_single_comp.dat"
patchLoadingFile="pressure_binary_reverse.dat"
nbBase = 1
periodicKeyoffset = 120
/
    &CB                                !In-rotor-plane rotation for a 3-bladed rotor
    Title="Constant Rotation"
    AxisType="TimeIndependent"
    AngleType="TimeIndependent"
    axisValue=0.0,0.0,1.0
    angleValue = -2.094395102
/

&ContainerIn
title="CW_blade_3_loading"
patchGeometryFile="geom_binary_reverse_single_comp.dat"
patchLoadingFile="pressure_binary_reverse.dat"
nbBase = 1
periodicKeyoffset = 240
/
    &CB                                !In-rotor-plane rotation for a 3-bladed rotor
    Title="Constant Rotation"
    AxisType="TimeIndependent"
    AngleType="TimeIndependent"
    axisValue=0.0,0.0,1.0
    angleValue = -4.188790205
/

```